Final Report

FDOT BDV31-977-121

Use of Infrared Thermography for the Inspection of Welds in the Shop and Field-Phase II

Prepared for:

Florida Department of Transportation State Materials Office
5007 NE 39th Avenue
Gainesville, FL 32609

FDOT Project Manager: Tim McCullough

Prepared by:

Department of Materials Science and Engineering
University of Florida
549 Gale Lemerand Dr.
Gainesville, Fl 32611

Principal Investigator: Professor Michele Manuel, Ph.D.

July 2023

Disclaimer Page

The opinions, findings, and conclusions expressed in this publication are those of the authors and not necessarily those of the State of Florida Department of Transportation.

Technical Report Documentation Page

1. Report No.	2. Government Accession No.	3. Recipient's Catalog No.

4. Title and Subtitle	5. Report Date
Use of Infrared Thermography for the Inspection of Welds in the Shop and Field – Phase II	July 2023
	6. Performing Organization Code
7. Author(s) Dr. Michele Manuel	8. Performing Organization Report No.
9. Performing Organization Name and Address University of Florida 100 Rhines Hall 549 Gale Lemerand Drive Gainesville, Florida 32611	10. Work Unit No. (TRAIS)
	11. Contract or Grant No. FDOT BDV31-977-121 August 27, 2019 – August 31, 2022
12. Sponsoring Agency Name and Address Florida Department of Transportation 605 Suwannee Street, MS 30 Tallahassee, Florida 32399	13. Type of Report and Period Covered Final Report August 2019 – July 2023
	14. Sponsoring Agency Code

15. Supplementary Notes

16. Abstract

The research focused on demonstrating and implementing infrared thermography non-destructive technique (IR-TNDT) methods in-service for inspecting aluminum (Al) and steel welds in complex structures. The study was applied to in-shop and mock in-field conditions. After a thorough literature review, this report presents the qualification of defect manufacturing procedures in the selected base materials, followed by sample preparation methods before infrared (IR) imaging. The work investigates the utility of the FLIR C5 and T620 cameras to produce a reliable and repeatable inspection of weld defects. The effect of applying protective coatings to the steel weld joint surface and a surface finish method applied to Al weld joints were addressed. The results illustrate that IR-TNDT is a promising non-destructive technique to identify surface-breaking defects in weld joints. However, proper defect identification is very sensitive to surface features. Quantitative destructive analysis was performed on weld joints to correlate defect geometry and location in the IR images. The FLIR T620 camera provided higher contrast and resolution imaging of surface-breaking defects than the FLIR C5 camera. It is recommended that IR-TNDT for steel and Al weld defect characterization be used concurrently with other non-destructive testing (NDT) techniques.

17. Key Words	18. Distribution Statement
Thermography, NDT, Infrared, Welds, IR-TNDT, Steel, Aluminum	

19. Security Classif. (of this report)	20. Security Classif. (of this page)	21. No. of Pages	22. Price
		94	

Form DOT F 1700.7 (8-72) Reproduction of completed page authorized

Acknowledgements

This work was supported by the Florida Department of Transportation (FDOT) under award number BDV31-977-121. Thank you to Brittany Maskley, Dr. Flavia Gallo, and the University of Florida Powell Family Structures and Materials Laboratory for their technical contributions and laboratory support on this project.

Executive Summary

The manufacturing of reliable bridge welds is of great importance to ensure public safety. Therefore, there is an ongoing effort to develop inspection methods for identifying weld defects that are more efficient and reliable while less costly and time-consuming.

Florida Department of Transportation (FDOT) has been considering the implementation of IR-TNDT as an alternative NDT method to overcome the challenges presented by conventional NDT methods, such as ultrasonic tests and radiography. This study evaluated the utility of using IR-TNDT as an accurate, efficient, and reliable non-contact method to inspect steel and Al weld joints in plate-to-plate and pipe-to-plate geometries.

The research was applied to in-shop and mock in-field conditions. The described active IR-TNDT methodology encompasses IR camera setup, calibration, sample heating, and imaging conditions. Controlled (artificially created) defects were induced into the base materials utilizing various defect manufacturing procedures. The study also included the evaluation of IR-TNDT on steel and Al weld joints with applied protective coatings and surface finish. The work identified the accuracy and effectiveness of the FLIR C5 and T620 IR cameras to produce a reliable and repeatable inspection of weld defects.

A complete dataset of thermal images by active IR-TNDT of plate-to-plate and pipe-to-plate Al and steel weld joints was produced. Surface-breaking defects were found to generate detectable indications using the IR-TNDT technology. Observable indications in the IR images also were generated from surface irregularities on the sample originating from typical welding artifacts such as splatter and slag, leading to disturbances in the IR images and false-positive indications in defect-free regions of the weld. Thus, it was determined that the proper defect identification of weld defects could be affected by sample surface topology. To correlate the IR images with depth-dependent defect geometries, destructive quantitative analysis was performed by cross-sectioning the samples near or at the defect centers. Overall, the results indicated that the FLIR T620 camera provided higher contrast and resolution imaging of surface-breaking defects than the FLIR C5 camera. Neither IR camera sufficiently identified subsurface defects. The application of protective coatings reduced false-positive indications by homogenizing (e.g., evening) the surface topography and decreasing the background IR noise, but viscous coatings obscured surface-breaking defects entirely. Surface modification via grinding and polishing provided minimal improvement in defect detection. Although the analysis of IR-TNDT is a promising technique to characterize and identify surface-breaking defects, it is recommended that IR-TNDT be used concurrently with other non-destructive testing (NDT) methods.

Table of Contents

DISCLAIMER PAGE ..... **II**

TECHNICAL REPORT DOCUMENTATION PAGE ..... **III**

ACKNOWLEDGEMENTS ..... **IV**

EXECUTIVE SUMMARY ..... **V**

LIST OF FIGURES ..... **VII**

LIST OF TABLES ..... **XIV**

CHAPTER 1 INTRODUCTION **1**

CHAPTER 2 BACKGROUND **3**

WELD DISCONTINUITIES AND DEFECTS 3
INFRARED THERMOGRAPHY NON-DESTRUCTIVE TECHNIQUE (IR-TNDT) 5
IR-TNDT METHODS 7
CHALLENGES TO THE IMPLEMENTATION OF IR-TNDT 8

CHAPTER 3 EXPERIMENTAL METHODS **11**

MATERIALS AND JOINT SPECIFICATIONS 11
WELD JOINT MANUFACTURING 15
WELD JOINT DEFECT MANUFACTURING 18
IR CAMERA PREPARATION 23
SAMPLE HEATING 25
IR IMAGING AND IR IMAGE ANALYSIS 27
DESTRUCTIVE TESTS FOR OPTICAL MICROSCOPY 28

CHAPTER 4 RESULTS **29**

IN-SHOP INFRARED TRIALS 29
IN-LABORATORY INFRARED TRIALS 43
IN-LABORATORY COMPLIMENTARY INFRARED TRIALS 52
DEFECT QUANTIFICATION THROUGH DESTRUCTIVE ANALYSIS 56

CHAPTER 5 CONCLUSIONS AND RECOMMENDATIONS **63**

CONCLUSIONS 63
RECOMMENDATIONS 63

REFERENCES **66**

APPENDIX A – WELDING PROCEDURE SPECIFICATIONS **71**

APPENDIX B – CAMERAS SPECIFICATIONS **75**

APPENDIX C – IR IMAGES OF COATED SAMPLES IN COMPARISON TO UNCOATED CONDITIONS AT DIFFERENT TEMPERATURE RANGES **77**

List of Figures

Figure 2-1 – Depiction of an undercut and overlap weld discontinuity present on a T-joint fillet weld [11]. 3

Figure 2-2 – Different types of porosity observed in welds. The types of porosity given are as follows: (a) uniformly scattered, (b) cluster, (c) linear, (d) elongated [11]. 4

Figure 2-3 – Example of LOF in a single V-groove weld joint [11]..... 4

Figure 2-4 – The different types of weld cracks shown in a groove weld: (1) crater, (2) transverse (located in the weld metal), (3) transverse (located in the base metal), (4) longitudinal, (5) toe, (6) underbead, (7) fusion-line, (8) root, and (9) hat [11]. 5

Figure 2-5 – Temperature decay plot of an Al joint welded using FSW, comparing defect and defect-free regions of the weld [19]. 6

Figure 2-6 – Temperature plots of SS weld joints with defects. (a) A surface-finished SS weld joint reveals only temperature peaks in regions with defects. (b) A SS weld joint that was not surface finished showed temperature peaks in regions with and without defects [21]. 6

Figure 2-7 – Cool-down behavior of a carbon steel weld in a region with and without a crack defect [9]. 7

Figure 2-8 – Schematic representation of the proposed active infrared thermography setup for weld inspection [9]. 8

Figure 2-9 – (a) Backside active thermography setup; (b) raw IR image; (c) FFT processed IR image showing corroded regions; (d) front-side setup and resulting FFT processed image showing several misleading points due to irregularities in protective layer [35].. 10

Figure 2-10 – IR-UTD processed image from weld cooling showing indication in the toe crack [8]..... 10

Figure 3-1 – The plate-to-plate and pipe-to-plate weld joint configurations used in this work..... 11

Figure 3-2 – The base plate to pole connection in FDOT Design Index #715-010 that was used in this work to design the steel pipe-to-plate weld joint [36]. 12

Figure 3-3 – The joint in FDOT Design Index #700-040 that was used in this work to design the steel plate-to-plate weld joint [36]. 13

Figure 3-4 – The joint in FDOT Design Index #715-002 that was used in this work for the Al cast plate-to-extruded pipe weld joint [36]. 14

Figure 3-5 – The joint in FDOT Design Index #715-002 that was used in this work for the extruded Al plate-to-plate weld joint [36]. 14

Figure 3-6 – Cross-section of the steel plate-to-plate weld joint. Image (a) shows the single-pass weld side, and (b) shows the multi-pass weld side of the joint. 16

Figure 3-7 – Cross-section of the steel pipe-to-plate weld joint. Images (a-b) show each cross-section of this joint when machined down the middle. 16

Figure 3-8 – Cross-section of the Al plate-to-plate weld joint. Image (a) shows the multi-pass weld side, and (b) shows the single-pass weld side of the joint. The areal % and total area of porosity for each weld were calculated to be (a) 4.7% and 0.10 mm^2 and (b) 4.4% and 0.05 mm^2, respectively. 17

Figure 3-9 – Cross-section of the Al pipe-to-plate weld joint. Images (a) and (b) show each cross-section of this joint when machined down the middle. The areal % and total area of porosity for each weld were calculated to be: (a) 5.8% and 0.07 mm^2 and (b) 3.1% and 0.05 mm^2, respectively. 17

Figure 3-10 – Cross-section of the Al plate-to-plate weld joint. This sample has a LOF at the joint, which will be treated as a pore defect for this work. The areal % and total area of porosity for this weld are 6% and 0.05 mm^2, respectively. 18

Figure 3-11 – Steel plate-to-plate joint with a Cu shot placed in a notch at the root of the joint before welding. 19

Figure 3-12 – Steel (a-d) plate-to-plate and (e-g) pipe-to-plate weld joint cross-sections where the Cu and notch were placed. All samples resulted in one or more cracks that were subsurface or surface-breaking. In addition to cracks, the defect welds possessed overlap, porosity, and undercut effects..... 20

Figure 3-13 – The Al plate-to-plate joint after one side was welded, and then a band saw was used to machine a cut horizontally through the weld. 21

Figure 3-14 – (a) Schematic representation of the machine-cut into the root of the joint before welding to create a subsurface pseudocrack. (b) Cross-sections of the Al plate-to-plate weld joint with a machined cut going through 7.6 cm of the weld. 21

Figure 3-15 – Schematic representation of the drill holes applied to the weld joints using a 1.6-mm (1/16”) diameter drill bit to create a surface-breaking hole. (a) Side view of the plate-to-plate weld joint and (b) front view of the pipe-to-plate weld joint. 22

Figure 3-16 – Front view of the two different geometries of weld joints with labels indicating where the defect was located and where the FLIR T620 lens center was positioned. (a) Steel and Al plate-to-plate joint, (b) steel and Al pipe-to-plate joint. 24

Figure 3-17 – Side view of the setup for the FLIR T620 camera based on the plate-to-plate weld joint. 25

Figure 3-18 – Side view of the setup for the FLIR C5 camera based on the plate-to-plate weld joint. 25

Figure 3-19 – Schematics indicating the location of the heat gun nozzle on both weld joints geometries when heating. (a) Steel and Al plate-to-plate weld joint, (b) steel and Al pipe-to-plate weld joint. 27

Figure 3-20 – Photography of the trial assembly, showing sample, camera, and heat gun positioning. 27

Figure 4-1 – (a-b) The defect-free IR images of the steel plate-to-plate joint using the FLIR T620 camera. (c-d) The FLIR T620 IR images of the steel plate-to-plate joints with manufactured subsurface cracks from a Cu contaminant (defect location labeled). The emissivity (ε) that the user sets in the camera is shown on the top left and on the right of the image is the corresponding temperature scale color scheme, which is automatically performed by the camera. 30

Figure 4-2 – (a-b) The defect-free IR images of the steel plate-to-plate joint using the FLIR C5 camera. (c-d) The FLIR C5 IR images of the steel plate-to-plate joints with manufactured subsurface cracks from a Cu contaminant (defect location labeled). The temperatures on the left of the images correspond to the temperature scale color scheme which is automatically performed by the camera. 31

Figure 4-3 – (a-b) The defect-free IR images of the steel pipe-to-plate joint using the FLIR T620 camera. (c-d) The FLIR T620 IR images of the steel pipe-to-plate joints with manufactured subsurface cracks from a Cu contaminant (defect location labeled). The emissivity (ε) that the user sets in the camera is shown on the top left and on the right of the image is the corresponding temperature scale color scheme, which is automatically performed by the camera. 32

Figure 4-4 – Optical image of the steel pipe-to-plate weld joint with slag over the defect center corresponding to the IR image in Figure 35(c). 32

Figure 4-5 – (a-b) The defect-free IR images of the steel pipe-to-plate joint using the FLIR C5 camera. (c-d) The FLIR C5 IR images of the steel pipe-to-plate joints with manufactured subsurface cracks from a Cu contaminant (defect location labeled). The temperatures on the left of the images correspond to the temperature scale color scheme, which is automatically performed by the camera. 33

Figure 4-6 – Optical image of the baseline sample steel plate-to-plate weld joint with labels showing examples of slag, cold spots (regions where slag spontaneously removed from the weld during cool-down), and weld spatter. 34

Figure 4-7 – The steel plate-to-plate weld joint with a 4x4-pixel box over a slag spot and a non-slag spot to measure the average temperatures of those regions. The slag spot box average temperature was 115°C, and the non-slag spot box average temperature was 112°C. 34

Figure 4-8 – The steel plate-to-plate weld joint with a 4x4-pixel box over a slag cold spot and a non-slag cold spot to measure the average temperatures of those regions. The cold

spot box average temperature was 51°C, and the non-slag cold spot box average temperature was 107°C. 35

Figure 4-9 – The steel plate-to-plate weld joint with a 4x4-pixel box over a weld splatter spot and a non-weld splatter spot to measure the average temperatures of those regions. The weld splatter spot box average temperature was 77°C, and the non-weld splatter spot box average temperature was 109°C. 35

Figure 4-10 – Optical image of the defect sample steel plate-to-plate weld joint with a label showing the cold spot location. 37

Figure 4-11 – Cross-section of the steel plate-to-plate defect weld joint where the cold spot was present in the IR images, labeled as Cu contaminant. A portion of Cu from the defect center melted backwards into this region, and this phenomenon resulted in the cold spots in the defect weld joint IR images. 37

Figure 4-12 – (a-b) The baseline IR images of the Al plate-to-plate weld joints with less underfill and (c-d) with more underfill. The emissivity (ε) that the user sets in the camera is shown on the top left and the corresponding temperature scale color scheme, which is automatically performed by the camera. 38

Figure 4-13 – The IR images of the defect sample Al plate-to-plate weld joint with a manufactured subsurface machined cut (defect location labeled). (a) FLIR T620 IR image of the defect sample weld joint. (b) FLIR C5 IR image of the defect sample weld joint. The emissivity (ε) that the user sets in the camera is shown on the top left and on the right of the image ‘a’ and left in ‘b’ is the corresponding temperature scale color scheme, which is automatically performed by the camera. 39

Figure 4-14 – (a-b) The IR images of the defect-free Al pipe-to-plate weld joint. (c-d) The IR images of the defect in Al pipe-to-plate weld joint with a manufactured subsurface machined cut (defect location labeled). The emissivity (ε) that the user sets in the camera is shown on the top left, and each image shows the corresponding temperature scale color scheme, which is automatically performed by the camera. 40

Figure 4-15 – Optical images of the two baseline Al plate-to-plate weld joints. (a) The baseline weld joint has some occurrences of underfill. (b) The baseline weld joint has a more frequent occurrence of underfill. 41

Figure 4-16 – FLIR T620 IR images of two additional baseline (defect-free) Al pipe-to-plate weld joints tested to further analyze the hot spot present in this joint type. (a) IR image of the baseline weld joint with the hot spot present. (b) IR image of the baseline weld joint imaged without a hot spot. The emissivity (ε) that the user sets in the camera is shown on the top left and on the right of the image is the corresponding temperature scale color scheme, which is automatically performed by the camera. 42

Figure 4-17 – Visual (top) and IR-TNDT (bottom) images at 100°C of the Al pipe-to-plate samples with the surface-breaking drill hole: (a) in the uncoated condition, (b) with the

applied surface finish. The black arrows point to the location of the surface-breaking drill hole. (c) Analysis of the temperature profile along the weld line plotted from the IR images of the uncoated and with surface finish samples. 44

Figure 4-18 – Visual (top) and IR-TNDT (bottom) images at 100°C of the Al plate-to-plate samples with the surface-breaking drill hole: (a) the uncoated condition, (b) with the applied surface finish. The black arrows point to the location of the surface-breaking drill hole. (c) A linear temperature profile along the weld line plotted from the IR images of the uncoated and with surface finish samples. 45

Figure 4-19 – Visual (top) and IR-TNDT (bottom) images at 100°C of the Al plate-to-plate samples with subsurface pseudocrack: (a) in the uncoated condition, (b) with the applied surface finish. No subsurface defect could be identified..... 46

Figure 4-20 – Visual (top) and IR-TNDT (bottom) images at 100°C of the steel pipe-to-plate samples with the surface-breaking drill hole: (a) in the uncoated condition, (b) coated with 1 layer of Zinc-It® spray, (c) with 3 layers of Zinc-It® spray. Black arrows point to the location of the surface-breaking drill hole. (d) A linear temperature profile along the weld line plotted from the IR images of the uncoated and coated samples. 47

Figure 4-21 – Visual (top) and IR-TNDT (bottom) images at 100°C of the steel plate-to-plate samples with the surface-breaking drill hole: (a) in the uncoated condition, (b) coated with 1 layer of Zinc-It® spray, (c) with 3 layers of Zinc-It® spray. Black arrows point to the location of the surface-breaking drill hole. (d) A linear temperature profile along the weld line plotted from the IR images of the uncoated and coated samples. 48

Figure 4-22 – Visual (top) and IR-TNDT (bottom) images at 100°C of the steel pipe-to-plate samples with the surface-breaking drill hole: (a) in the uncoated condition, (b) coated with the epoxy-based coating. The black arrows point to the location of the surface-breaking drill hole. In ‘b’, no defect can be detected. (c) A linear temperature profile along the weld line plotted from the IR images of the uncoated and coated samples. 50

Figure 4-23 – Visual (top) and IR-TNDT (bottom) images at 100°C of the steel plate-to-plate samples with the surface-breaking drill hole: (a) in the uncoated condition, (b) coated with the epoxy-based coating. The black arrows point to the location of the surface-breaking drill hole. The defect was not observable after coating with the epoxy-based coating. (c) A linear temperature profile along the weld line plotted from the IR images of the uncoated and coated samples. 51

Figure 4-24 – Al pipe-to-plate weld joint sample, with surface-breaking drill hole and 120-grit surface finish: (a) IR image taken with FLIR C5 camera, (b) IR image taken with FLIR T620 camera. A white arrow points to the defect and a label informs the diameter of the hole. Some examples of artifacts are also labeled. A temperature scale in °C is provided on the right side of each IR image. 53

Figure 4-25 – Al plate-to-plate weld joint sample, with surface-breaking drill hole and 120-grit surface finish, in (a) IR image taken with FLIR C5 camera and in (b) with FLIR T620

camera. A white arrow points to the defect and a label informs the diameter of the hole. Some examples of artifacts are also labeled. A temperature scale in °C is provided on the right side of each IR image..... 54

Figure 4-26 – Al plate-to-plate weld joint sample, with subsurface pseudocrack and 120-grit surface finish, in (a) IR image taken with FLIR C5 camera and in (b) with FLIR T620 camera. The location of the machined cut pseudocrack is indicated. A temperature scale in °C is provided on the right side of each IR image..... 54

Figure 4-27 – Steel plate-to-plate weld joint sample, with surface-breaking drill hole without coating, in (a) IR image taken with FLIR C5 camera and in (b) with FLIR T620 camera. A white arrow points to the defect and a label informs the diameter of the hole. Some examples of artifacts are also labeled. A temperature scale in °C is provided on the right side of each IR image..... 55

Figure 4-28 – Steel plate-to-plate weld joint sample, with surface-breaking drill hole coated with AMERCOAT® 399, in (a) IR image taken with FLIR C5 camera and in (b) with FLIR T620 camera. A white arrow points to the defect and a label informs the diameter of the hole. A temperature scale in °C is provided on the right side of each IR image. 55

Figure 4-29 – Steel pipe-to-plate weld joint sample, with surface-breaking drill hole without coating, in (a) IR image taken with FLIR C5 camera and in (b) with FLIR T620 camera. A white arrow points to the defect and a label informs the diameter of the hole. A temperature scale in °C is provided on the right side of each IR image. 56

Figure 4-30 – Cross-section of the Al pipe-to-plate weld joint sample, showing the produced surface-breaking drill hole. Other subsurface weld defects could be observed from the cross-section and are pointed out in the optical image. Dimensions are labeled. 57

Figure 4-31 – Cross-section of the Al plate-to-plate weld joint sample, showing the produced surface-breaking drill hole. Other subsurface weld defects could be observed from the cross-section and are pointed out in the optical image. Dimensions are labeled. 57

Figure 4-32 – Cross-section of the steel plate-to-plate weld joint sample, showing the produced surface-breaking drill hole. Other subsurface weld defects could be observed from the cross-section and are pointed out in the optical image. Dimensions are labeled. 58

Figure 4-33 – Cross-section of the steel pipe-to-plate weld joint sample, showing the produced surface-breaking drill hole. Other subsurface weld defects could be observed from the cross-section and are pointed out in the optical image. Dimensions are labeled. 58

Figure 4-34 – Cross-section of the Al plate-to-plate weld joint sample, showing the machine cut subsurface pseudocrack. Other subsurface weld defects could be observed from the cross-section and are pointed out in the optical image. Dimensions are labeled. 59

Figure 4-35 – Example of a zoomed in IR image (of the Al pipe-to-plate sample) taken with (a) C5 and (b) T620 cameras, evidencing increased sharpness of defect edges in the T620 image in ‘b’. 61

Figure 4-36 – Zoomed in IR image of the steel plate-to-plate sample coated with AMERCOAT®, taken with (a) C5 and (b) T620 cameras, evidencing very imprecise defect edges in both images. 61

List of Tables

Table 3-1– Materials, geometries, and surface conditions investigated. 15

Table 3-2 – Measured weld emissivity for the weld joints studied in this work. 24

Table 3-3 – A listing of the sample population to be tested and the maximum test temperature used in the study. 26

Table 4-1 – Summary of measurements from the optical micrographs (OM) and IR images using the FLIR T620 and FLIR C5 cameras. Defect data are represented as averages with standard deviation 60

Chapter 1 Introduction

The manufacturing of reliable bridge welds is of great importance to ensure public safety. Transportation structures, such as light poles and signs, must be manufactured to minimize failures that could lead to accidents or potential roadway hazards. Welding is a crucial manufacturing area within FDOT. Welds must be sound to produce strong and durable parts for various roadway structures. Because welds can present defects compromising their integrity, additional measures are needed to ensure they are sound and meet minimum safety standards. Thus, inspecting weld defects is vital for safety.

Inspection methods for identifying subsurface defects in welds that are more efficient and implementable while remaining reliable is lacking. Despite the chosen joining technique, any deficient procedure may induce flaws, which must be detected early to avoid reducing the safe life of the welded parts. Madhvacharyula et al. [1] reviewed common defects in welds, for instance, porosity, cracks, and undercut. The authors also discussed in situ methods for detection, including ultrasonic testing (UT), radiography, and magnetic particle testing [1].

In UT, acoustic waves are used to penetrate materials to detect subsurface defects through discontinuities in the reverberated sound waves [2]. This technique is more complex, time-consuming, and costly than other NDT methods [3]. Radiography uses X-rays to penetrate welds and can detect discontinuities as these areas transmit rather than absorb more X-rays than the surrounding bulk material, which results in dark regions of the processed image [4]. This technique has material thickness limitations for defect detection and can fail to detect cracks parallel to emitted X-rays. Additionally, radiography has increased user hazards due to the presence of radiation and is time- and cost-inefficient [2], [3]. Magnetic particle testing is a safe, time- and cost-effective NDT method used in weld defect detection, which uses magnetic particles in an applied magnetic field to locate defects [2]. However, this technique is restricted to ferromagnetic materials, such as steels, and can only detect surface or near-surface defects [2]. There is a need to develop an NDT method that is safe while time- and cost-efficient without a loss in subsurface defect detection capabilities and can be applied to nonferrous materials, such as Al.

Infrared thermography NDT (IR-TNDT) is used in applications ranging from the maintenance of electrical components to the corrosion of steel pipes to detect flaws [5]. IR-TNDT can record the temperature distributions on and around a target by analyzing thermal radiation [6]. Promising efforts have been made to use IR-TNDT to detect weld defects [7]–[9]. These works have found that IR-TNDT can detect subsurface defects. Still, detection becomes challenging at greater depths because it requires more significant temperature gradients and higher IR camera resolution [7], [9]. There is yet to be a study that collectively investigates the effect of weld joint types, base metals, specific defect depths, and using the welding process as the heating method in IR

inspections. Such an investigation would benefit FDOT as it could be immediately applied to its manufacturing processes in both a time- and cost-efficient manner.

This investigation seeks to understand the efficacy of the IR-TNDT method in detecting welding defects through the creation and experimental testing of practical weld samples. The FDOT and American Welding Society (AWS) standards were used to develop defect-free and defective weld joints. Two commercially available IR-TNDT devices, the FLIR C5 and T620 cameras, were used to acquire IR images after welding. These thermal images were qualitatively inspected and processed to identify anomalies to illustrate their potential to detect different surface-breaking and subsurface defects. The welded samples underwent a mock in-field inspection to determine if the IR-TNDT method could locate the defects after in-shop welding. The subsurface defect geometry was determined using destructive analysis by sectioning the samples near the defect centers. These results were then correlated to the IR-quantified defect geometries to garner insight into the level of accuracy using the IR cameras. This investigation aims to determine if IR-TNDT can detect weld defects in steel and Al weld joints and, if so, to develop procedures accordingly.

Chapter 2 Background

Weld discontinuities and defects

Welded parts may possess discontinuities, however, not all discontinuities will compromise the integrity of the weld joint. A discontinuity is only considered a defect when it has a high risk of failure and, as a result, must be repaired or rejected from service [4]. Discontinuities can be present on the surface or subsurface of the weld and base metal. They can also be present within the heat-affected zone (HAZ) of the base metal, defined as the region of the base metal with microstructural changes from the high temperatures experienced during welding [10]. The AWS, which oversees the standardization of welds in the United States, provides resources for determining when these discontinuities are deemed defects and the proper course of action to take upon finding a defect.

Undercut and overlap are a set of welding process-related discontinuities that can be identified based on the geometry of the weld joint profile [11], [12]. The undercut is the melting of the base metal near the weld toe or root that occurs during welding and results in a flaw in this region, as demonstrated in the T-joint fillet weld shown in Figure 0-1[11].

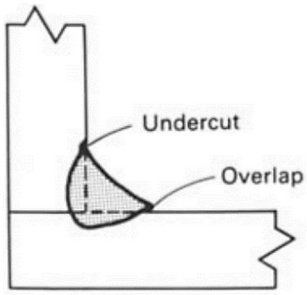

Figure 0-1 – Depiction of an undercut and overlap weld discontinuity present on a T-joint fillet weld [11].

Porosity is a discontinuity type categorized under welding process-related metallurgical discontinuities [11], [12]. Its presence appears as 3-dimensional voids throughout the weld metal and fusion zone that result from the entrapment of gases [11]. Figure 0-2 displays the four main microstructural topographies of porosity.

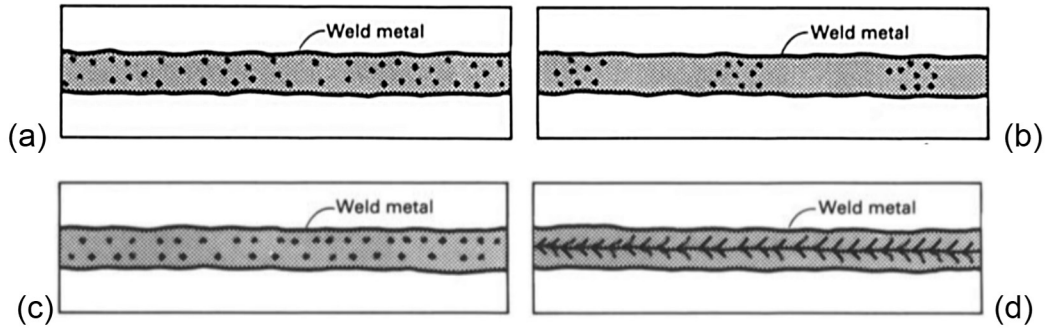

Figure 0-2 – Different types of porosity observed in welds. The types of porosity given are as follows: (a) uniformly scattered, (b) cluster, (c) linear, (d) elongated [11].

The lack of fusion (LOF) is a welding process-related discontinuity defined as any area of the weld metal that is improperly fused to the base metal [11], [12]. Unlike the other discontinuities mentioned, LOF has no allowable limits, and thus, any presence of it is deemed a defect. An example of LOF in a single V-groove weld joint is shown in Figure 0-3.

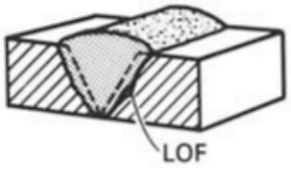

Figure 0-3 – Example of LOF in a single V-groove weld joint [11].

The final weld discontinuity to be discussed is cracks categorized as metallurgical discontinuities [11], [12]. Cracks are a form of fracture that can occur in the weld or base metal and, similar to LOF, are never allowable in the final weld.

Figure 0-4 shows different types of weld cracks. Cracks can be identified as transgranular or intergranular, revealing the mechanism which resulted in the crack [13].

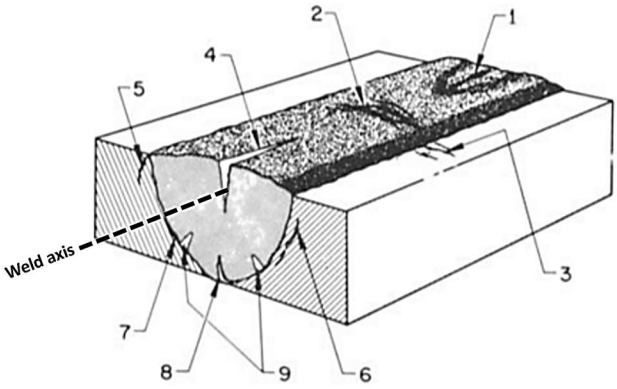

Figure 0-4 – The different types of weld cracks shown in a groove weld: (1) crater, (2) transverse (located in the weld metal), (3) transverse (located in the base metal), (4) longitudinal, (5) toe, (6) underbead, (7) fusion-line, (8) root, and (9) hat [11].

Infrared thermography non-destructive technique (IR-TNDT)

Infrared thermography non-destructive technique arises as a promising method used in applications ranging from the maintenance of electrical components to the corrosion of steel pipes to detect faults or flaws [5]. The concept that a defect will radiate thermal energy different from the surrounding bulk material has motivated the use of IR-TNDT for defect detection. Some of the earlier instances of IR-TNDT were used for defect detection in materials ranging from composites to electronic materials [14]–[18]. One of the earliest uses of IR-TNDT for composite defect detection was demonstrated on rocket motor cases in the early 1960s, where voids could be identified using temperature contour maps taken from the motor cases upon heating and scanning with IR cameras [14]–[17]. In electronic material defect detection, IR-TNDT has been used since 1963 to detect defects in circuits where the flaws are displayed as hot spots in the produced thermographs [18].

More recent studies have continued to test IR-TNDT for weld defect detection. One study detected and characterized defects in friction stir welded (FSW) Al joints. The cool-down of the defect-free and defect regions was monitored as a function of time to generate temperature distribution plots that could be analyzed for discontinuities [19]. The cool-down plot of the defect and defect-free regions of the weld is shown in

Figure 0-5 [19]. Only one Al joint was tested in this study, creating a need to verify the techniques' repeatability on other joint types. Another study that tested IR-TNDT on FSW Al joints analyzed weld process-related discontinuities, which can obscure the thermal signal from nearby defects [20].

A more detailed review of weld process-related discontinuities was conducted on 71 mm thick stainless steel (SS) welded joints with surface-breaking defects, which were heated and then imaged using IR cameras [21]. This study used image reconstruction of the timelapse IR images to remove background noise. However, this still resulted in false positives in weld regions without defects due to weld process-related

discontinuities [21]. Figure 0-6 shows the relative temperature versus position graphs of the SS weld joint with surface finishing and without surface finishing [21].

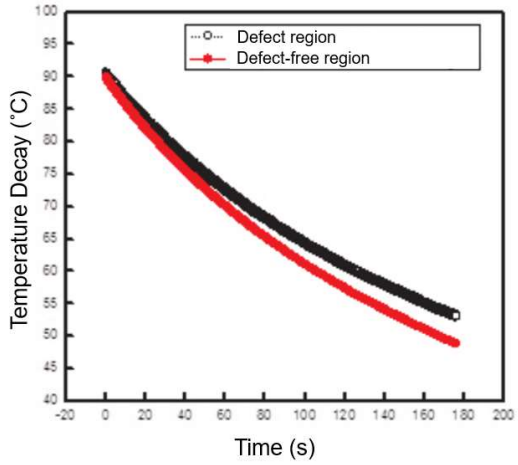

Figure 0-5 – Temperature decay plot of an Al joint welded using FSW, comparing defect and defect-free regions of the weld [19].

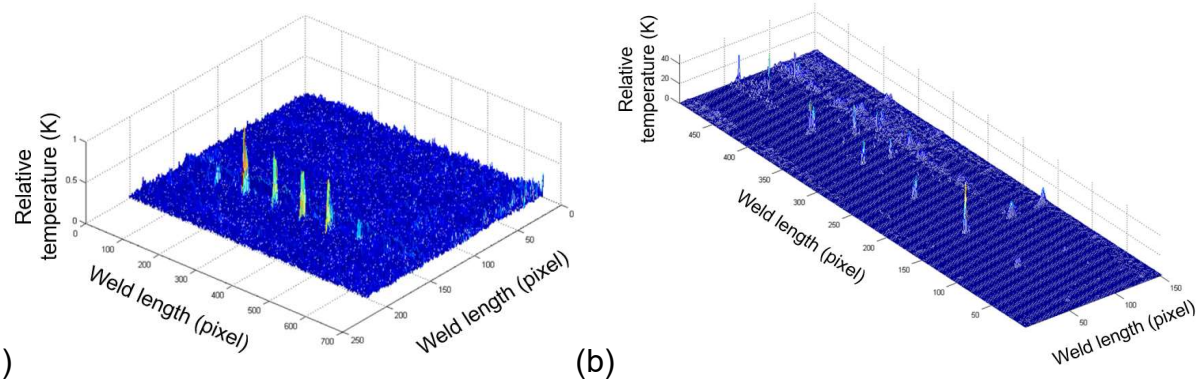

(a) (b)

Figure 0-6 – Temperature plots of SS weld joints with defects. (a) A surface-finished SS weld joint reveals only temperature peaks in regions with defects. (b) A SS weld joint that was not surface finished showed temperature peaks in regions with and without defects [21].

Two studies have attempted to document the heat transfer behavior of a weld with a defect by analyzing the cool-down curves of carbon steel weld joints with defects and comparing them to weld regions without defects [7], [9]. An example is shown in Figure 0-7, where the time-dependent thermal profile differs in the defect-free and defective areas. The portion of the weld containing the defect cools faster than the defect-free region [9], opposingly to the data obtained for Al weld joints, as shown in Figure 0-5 [19].

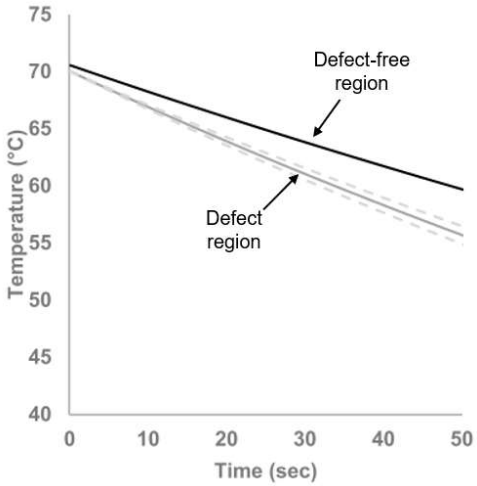

Figure 0-7 – Cool-down behavior of a carbon steel weld in a region with and without a crack defect [9].

IR-TNDT methods

IR-TNDT can be a qualitative or quantitative analysis, and two approaches are possible: passive and active thermography. Passive thermography monitors the structure under normal environmental conditions, whereas active thermography generates a temperature profile by applying an external heat source. The latter is divided into two categories: pulsed thermography (PT), characterized by a continuous heat transfer followed by monitoring during the cooling phase, or lock-in thermography (LT), where heat is provided by a sinusoidal temperature modulator and image collection occurs during the entire cycle time [22], [23].

IR-TNDT can record the temperature distributions on and around a target by analyzing thermal radiation [6]. Promising efforts have been made to use IR-TNDT to detect weld defects [7]–[9]. Still, defect detection becomes challenging when the flaw is located at greater depths since it requires more significant temperature gradients and higher IR camera resolution [7], [9].

Dorafshan et al. [9] used the experimental setup shown in Figure 0-8 to address weld defects manufactured in the laboratory (porosity and cracks) previously diagnosed by UT NDT inspection. The heat gun, placed within 50 mm of the bottom of the specimens, increased the temperature of the area of interest. The maximum temperature reached by the active thermography was 70°C. After reaching that temperature, the heat gun was turned off, and the camera started recording a thermal sequence at a frequency of 10 Hz for 50 s and analyzed through ThermaVision Examine IR software.

.

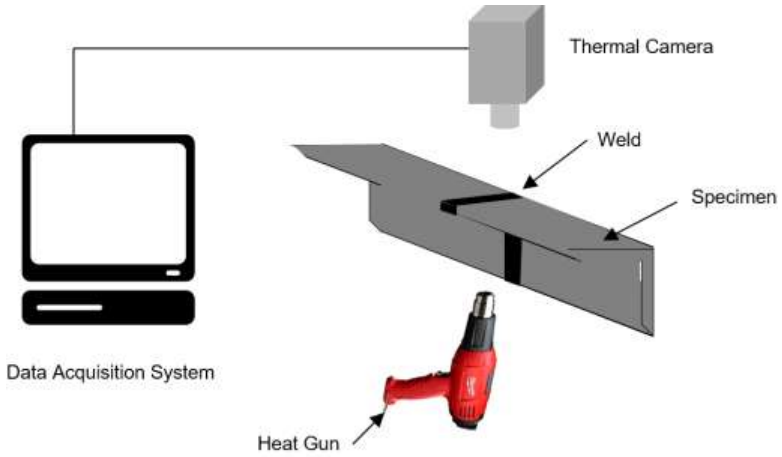

Figure 0-8 – Schematic representation of the proposed active infrared thermography setup for weld inspection [9].

Challenges to the implementation of IR-TNDT

To increase the applicability, acceptance, and reliability of IR-TNDT in-field, several authors have worked on the comparison of the IR-TNDT results with other well-established destructive and non-destructive techniques [1], [23]–[25]. However, using individual raw IR images to detect defects is a challenge. Authors [26] claim that only qualitative analysis is possible using IR-TNDT since defect quantification of size and depth cannot be determined without prior knowledge of the internal structure and application of image post-processing techniques.

Even though there are advances in IR image post-processing techniques, there remains a lack of understanding and convergence on its use for defect quantification. In addition, there is a difference between the observation of in-laboratory produced defects and actual defects found in-field. It has also been argued that empirical information often lacks conclusive physical meaning to interpret IR images [26].

The literature [9], [27]–[29] shows that noise and surface topography considerably affect IR-TNDT images. The presence of surface irregularities, which are not necessarily associated with welding defects, can increase false-positive indications through thermal imaging [9]. Dorafshan et al. [9] also claim low-emissivity materials like steel are more susceptible to topographical irregularities. Thus, for the particular case of weld inspection by active IR-TNDT, it has been recommended that the inspector grind the weld surface or cover it with high-emissivity paint to provide a mono-contrast background for thermography [9]. According to Luong [28], matte spray paint raises the surface emissivity to a uniformly high level. It reduces surface reflections, improving the detectability of the onset of defects under fatigue loading.

Other challenges to IR imaging are related to the diffuse scattering of electromagnetic radiation whenever the wavelength dimension is comparable to the surface roughness. This phenomenon impacts the identification and suppression of thermal reflections in the wavelength range of IR cameras. The low emissivity of hot gases in metallic cavities

can also confound the analysis leading to false-positive defect detection [30]. Another drawback of the IR-TNDT is the demand for an experienced operator for an accurate visual perception of the raw IR images, also called thermograms.

Ultimately, the precise interpretation of IR images relies on the application of post-processing methods. For example, Yang et al. [31] proposed applying deep learning techniques for detecting cracks in infrared thermal imaging using Convolutional Neural Networks (CNN). Furthermore, integrated approaches combining the use of several NDT methods, such as X-Ray, X-Ray fluorescence (XRF) spectroscopy, dye penetrant liquid, with finite element modeling (FEM) are claimed to improve the accuracy in defect detection [27], [32]. Ibarra-Castanedo et al. [33] reviewed various methods for post-processing IR images generated from pulsed phase thermography (PPT), such as binarization, noise smoothing through a kernel, and quantitative inversion methods. A method for thermographic signal reconstruction (TSR) data processing has been proposed for passive thermography for in situ mechanical testing by convoluting a set of IR images into a single representative one, which will be further visually analyzed by the operator [34].

According to Milovanović and Pečur [26], the most frequently applied approach to thermal image analysis is the thresholding technique to support the identification of the hotspot. As proposed, the first steps of IR-TNDT data processing are boosting the signal-to-noise ratio by averaging thermograms followed by edge filtering to accentuate the contrast within defective regions.

A Fast Fourier Transform (FFT) method was used to process IR images taken from steel pressure vessels to investigate pit corrosion [35]. Backside active thermography resulted in good detection of damaged areas after post-processing. However, the front-side reflection mode for IR image acquisition resulted in significant noise due to irregularities in the protective layer, showing that this mode is more susceptible to topographical issues. Figure 0-9a shows the setup for backside active thermography used by the authors [35]. The resulting FFT-processed image is illustrated in Figure 0-9(c), which compares the backside active thermography to the raw IR image in Figure 0-9(b). Figure 0-9(d) shows the reflection mode of IR image acquisition and the FFT-processed image, where the authors [35] identified features unrelated to the defective areas.

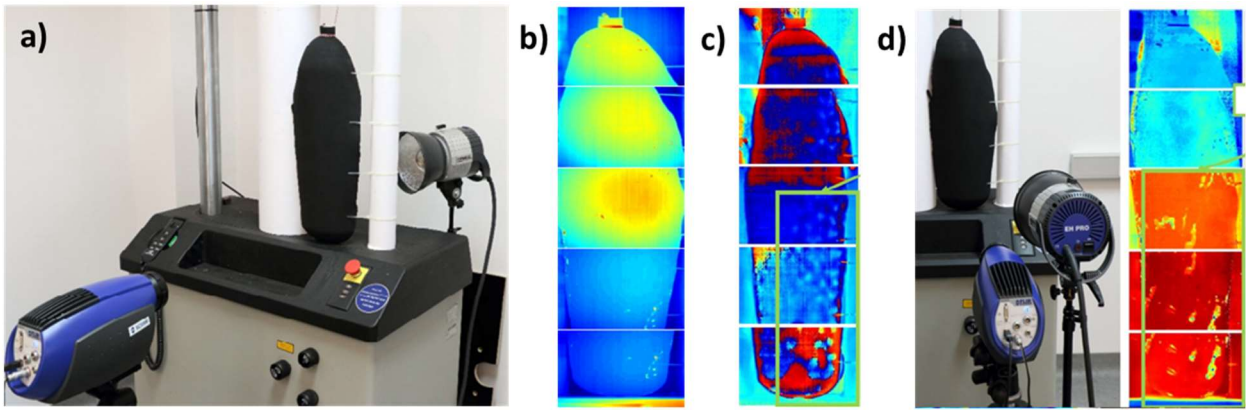

Figure 0-9 – (a) Backside active thermography setup; (b) raw IR image; (c) FFT processed IR image showing corroded regions; (d) front-side setup and resulting FFT processed image showing several misleading points due to irregularities in protective layer [35].

The author's FDOT BDV31 977-64 Phase I report [8] investigated an infrared ultra-time domain (IR-UTD) processing approach that utilizes time-lapse thermal images captured during the heating and cooling process to detect subsurface defects. As seen in Figure 0-10, it was demonstrated that in a conventional IR image produced without the time-lapse processing implemented in the IR-UTD, the crack identification did not appear clearly due to the noise created by other surface anomalies.

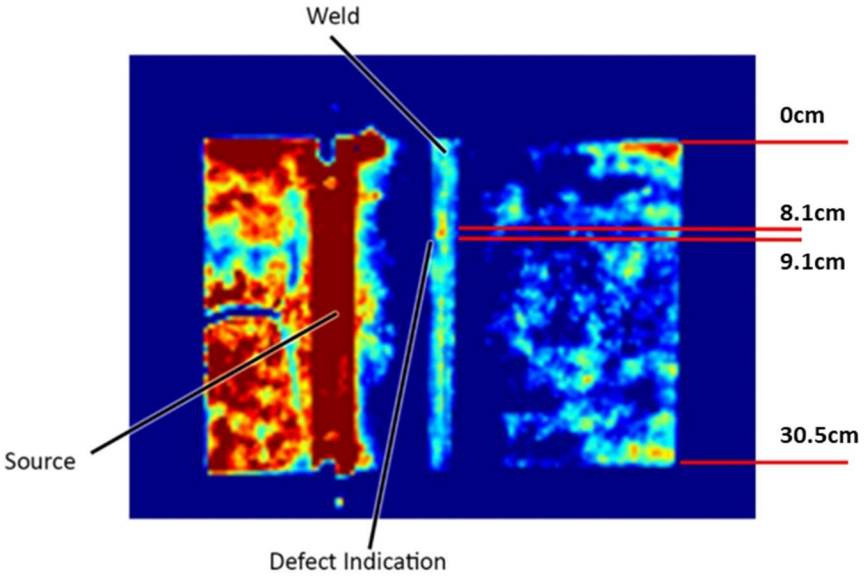

Figure 0-10 – IR-UTD processed image from weld cooling showing indication in the toe crack [8].

Chapter 3 Experimental Methods

The following sections detail the design of the defect-free welds, welding procedures, and defect manufacturing methods. Additionally, surface finishes and destructive analysis for defect quantification are also described.

Materials and joint specifications

Established FDOT component geometries were used to enable the possibility of implementing IR-TNDT into the welding manufacturing processes. This study used scaled-down designs that could be downsized without drastically changing the appropriate welding procedure. Downsizing allowed for increased repeatability. The FDOT parts that fit these design needs were light poles and roadway signs, which are typically manufactured using steel or Al alloys. Although there are many welding joint types in these designs, the two types used in this project were plate-to-plate and pipe-to-plate joints, as illustrated in Figure 0-1. The FDOT design indexes used to design the weld joints in this work are described in the following subsections.

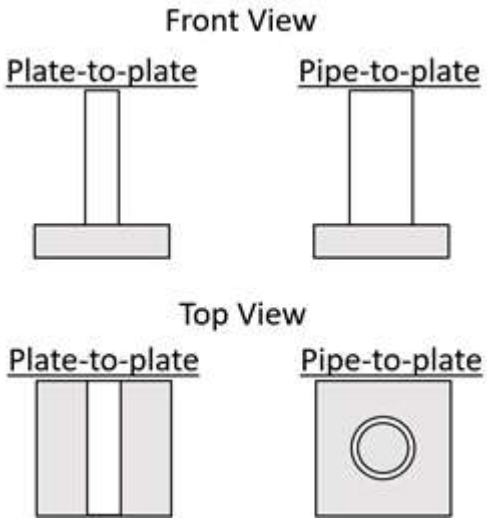

Figure 0-1 – The plate-to-plate and pipe-to-plate weld joint configurations used in this work.

Steel design indexes

The two FDOT design indexes used to design the steel welding joints are Index #715-010 (High Mast Lighting) and Index #700-040 (Cantilever Sign Structure) [36]. Both designs were taken from the FY 2020-21 Standard Plans [36]. From these two design indexes, the types of steel included are ASTM A709 (Gr. 36) and ASTM A36 for the plates and API 5L x42 PSL2, ASTM A500 (Gr. B min.), and ASTM A572 (Gr. 50, 55, 60, and 65) for the pipes. Figure 0-2 illustrates the joint in Index #715-010 used to design the pipe-to-plate weld. The thickness of the pole is 0.6 cm and the thickness of the base plate is approximately 7.6 cm, however this will be downsized to 0.6 cm thick since a 7.6 cm thick base plate would require increased welding needs including more welding material and a pre-heat of the base metal prior to welding. Figure 0-3 shows the joint in Index #700-040 used to design the plate-to-plate weld. In the design, the small plate

connections are welded to the pole. The pole in this design has a large diameter that allows for the joint to be simplified to a plate-to-plate configuration. The thickness of the pole is 2.2 cm thick which would require increased welding needs so to keep consistency with the other weld joint, a 0.6 cm thickness will be adopted here as well. The plate connections on the pole are 1.3 cm thick which can be changed to 0.6 cm thickness without affecting the welding procedures to be qualified [36].

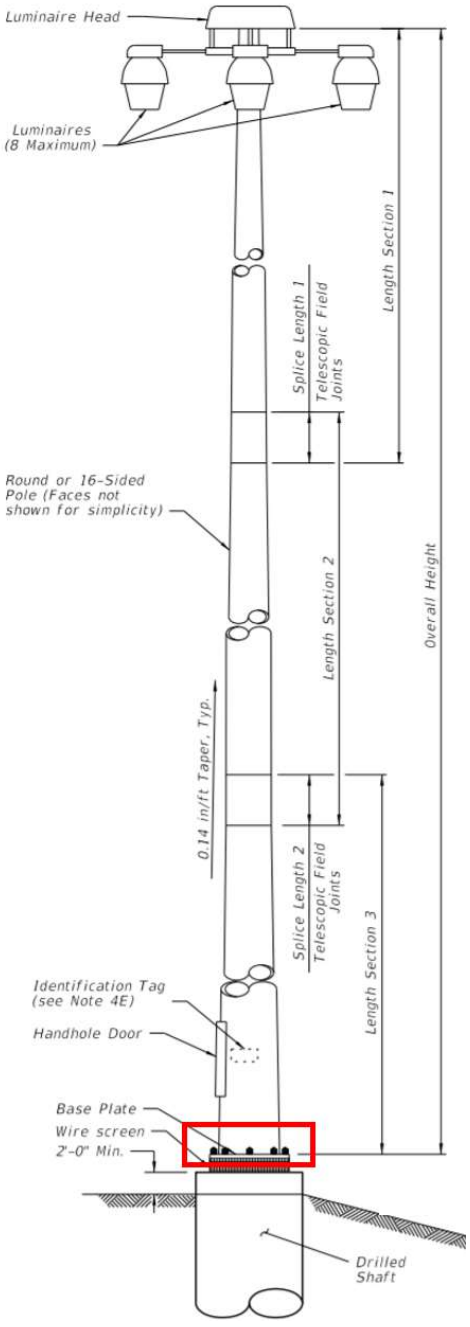

Figure 0-2 – The base plate to pole connection in FDOT Design Index #715-010 that was used in this work to design the steel pipe-to-plate weld joint [36].

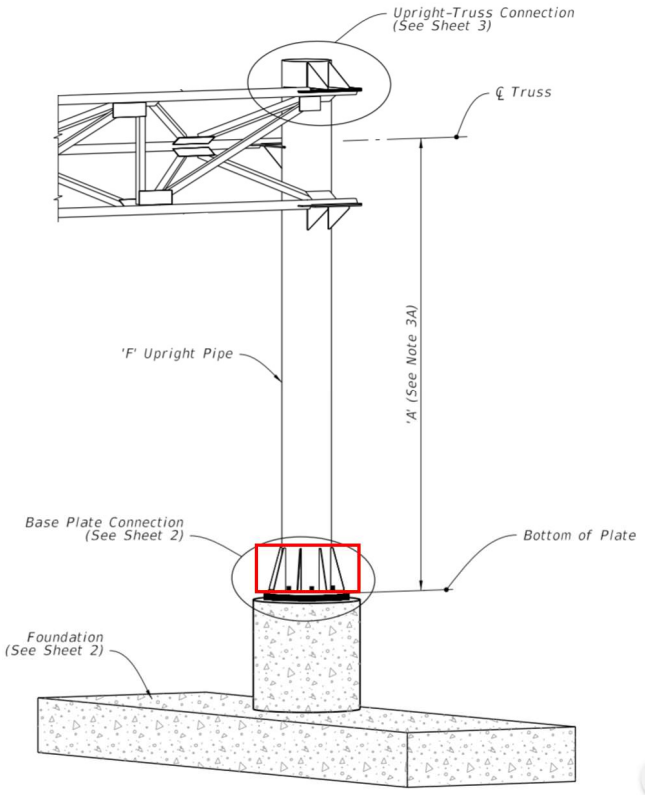

Figure 0-3 – The joint in FDOT Design Index #700-040 that was used in this work to design the steel plate-to-plate weld joint [36].

Aluminum design indexes

The FDOT Design Index used to design the Al weld joints is Index #715-002 (Standard Aluminum Lighting), taken from FY2020-21 [37]. The types of Al used in this design include Alloy 356-T6 (ASTM B26 or B108) cast Al plate and Alloy 6061-T6 and 6063-T6 extruded Al plate and pipe (ASTM B221). The joint shown in Figure 0-4 was used to design the cast plate to extruded pipe weld. There are several pole thicknesses given in the design but the thickness to be used in this work is 0.6 cm. The cast plate has an unspecified thickness as it is used as a shoe fitting for the pole but a thickness of 0.6 cm will be selected for this work to allow for weldability with the 0.6 cm thick pole. Figure 0-5 shows the joint used for the extruded Al plate-to-plate design. This joint is a bracket welded to the pole but was simplified to a plate-to-plate joint since they both use fillet welds. The thicknesses for each plate were selected based on the thickness of the pole which is 0.6 cm.

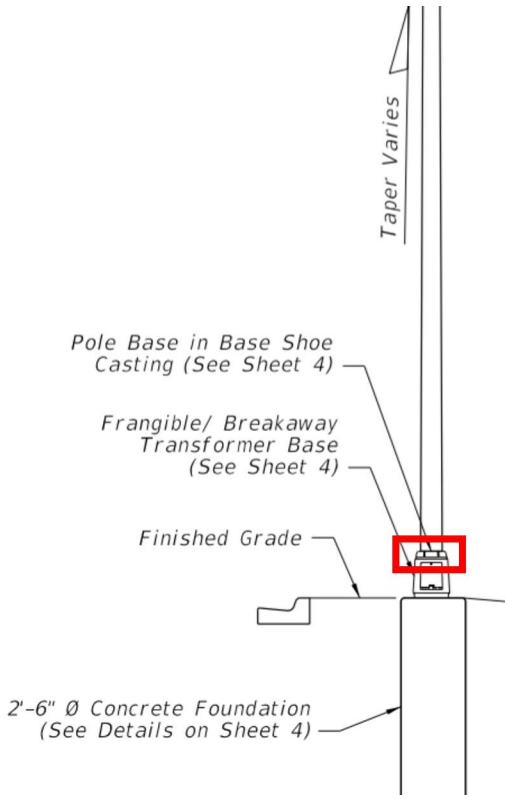

Figure 0-4 – The joint in FDOT Design Index #715-002 that was used in this work for the Al cast plate-to-extruded pipe weld joint [36].

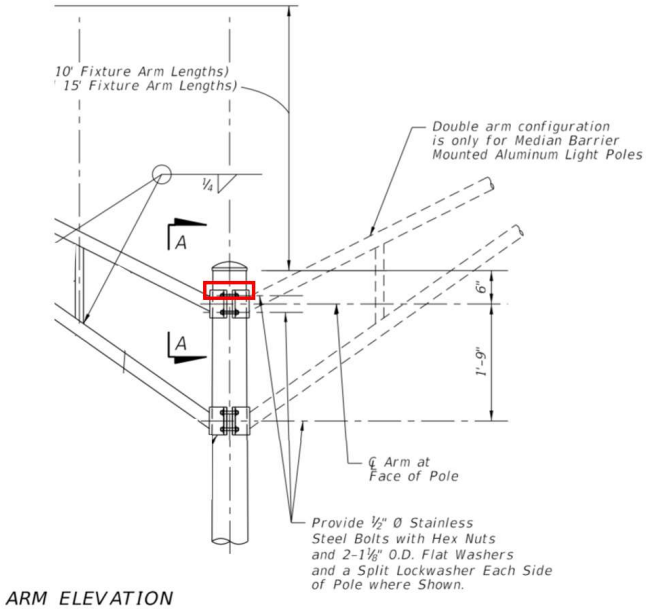

Figure 0-5 – The joint in FDOT Design Index #715-002 that was used in this work for the extruded Al plate-to-plate weld joint [36].

Summary of materials and joints selected

In summary, there will be four specimens used in this work, two steel and two Al. The two joint types for each material will be fillet welds on a pipe-to-plate and a plate-to-plate joint. The steel plate-to-plate joint used A36. The steel pipe for the pipe-to-plate joint was A500, and the corresponding steel plate will be made with A36. One Al plate-to-plate joint used extruded 6061-T6. The Al pipe used for the pipe-to-plate joint consisted of extruded 6061-T6, while the Al plate was cast Al 356-T6. A summary of the base materials, weld geometries, and surface conditions is displayed in Table 0-1. The thickness of all the materials used in this study was 6.3 mm.

Table 0-1– Materials, geometries, and surface conditions investigated.

Geometry	Materials	Surface Condition
Plate-to-plate	A36 steel (plates)	Uncoated Zinc-It® AMERCOAT® 399
Pipe-to-plate	A500 steel (pipe)/A36 steel (plate)	Uncoated Zinc-It® AMERCOAT® 399
Plate-to-plate	Al extruded 60601-T6 (plates)	Uncoated Textured satin surface finish
Pipe-to-plate	Al extruded 60601-T6 (pipe)/ Al 356-T6 (plate)	Uncoated Textured satin surface finish

Weld joint manufacturing

The most applicable welding process for steel and Al joints used in FDOT parts is the gas metal arc welding (GMAW) process. The steel welding procedures were selected based on the AWS codebook D1.1. and Al welding procedures were selected based on the AWS codebook D1.2. [37], [38].

Steel Joints

The steel joints were welded using a Millermatic 252 GMAW machine. The gas mixture was 75% argon (Ar) and 25% carbon dioxide (CO_2). A ER70S-6 welding wire spool of 0.9 mm diameter was used. The A36 plate-to-plate and A500 pipe-to-A36 plate joints used the same welding machine settings. The machine was set to 23.2 V with a wire speed of 365 inches per minute (IPM). One side of the plate-to-plate joint had a single-pass weld, and the other had a multi-pass weld. The pipe-to-plate joint had only a single pass weld. The welding procedure specifications (WPSs) for these welds contain additional details on the welding procedures performed and can be found in Appendix A of this report.

The welds were macroetched using a 2% nital solution [39] and then visually inspected to confirm that these settings and procedures yielded a baseline/sound weld joint. The optical images of the etched steel weld joints are shown in Figure 0-6 and Figure 0-7. There is complete fusion of the weld metal to the base metals with no signs of any discontinuities.

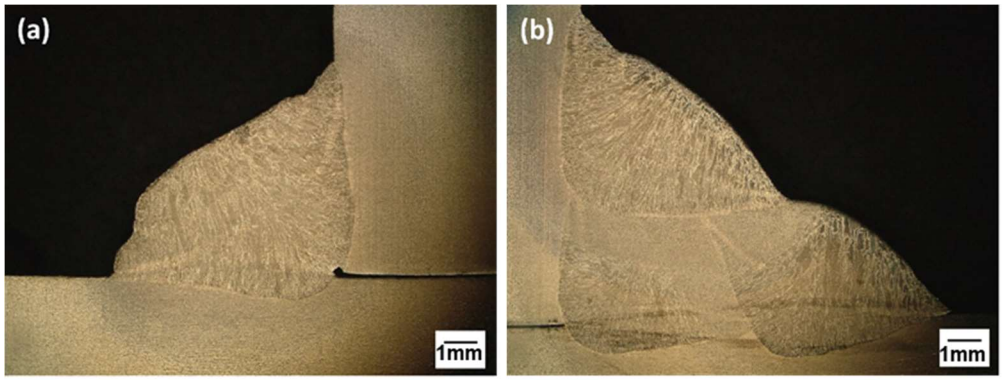

Figure 0-6 – Cross-section of the steel plate-to-plate weld joint. Image (a) shows the single-pass weld side, and (b) shows the multi-pass weld side of the joint.

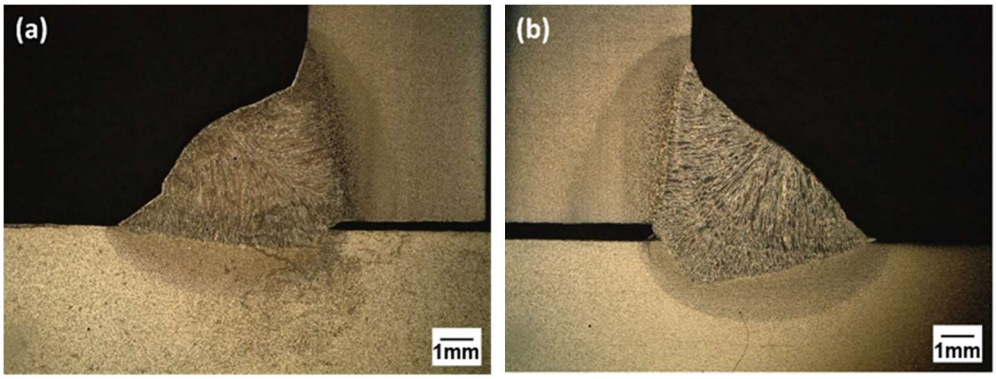

Figure 0-7 – Cross-section of the steel pipe-to-plate weld joint. Images (a-b) show each cross-section of this joint when machined down the middle.

Aluminum Joints

The Al joints were welded using a Millermatic 252 GMAW machine equipped with a Miller Spoolmatic 30A and pure Ar gas. A ER4043 welding wire spool of 0.9 mm diameter was used. The machine was set to 26.7 V and a gun setting of 6. The gun setting controls the wire speed. One side of the plate-to-plate joint had a single-pass weld, and the other had a multi-pass weld. The pipe-to-plate joint had only a single-pass weld. The WPSs for these welds contain more details on the welding procedures performed and can be found in Appendix A of this report.

The welds were polished up to 0.05-μm grit using the Buehler MasterPolish alumina and colloidal silica suspension, which resulted in mild etching of the Al weld surface. The optical images of the polished Al weld joints are shown in Figure 0-8, Figure 0-9 and Figure 0-10. All samples had subsurface porosity within the allowable amount of discontinuity area for the relative weld size following Table 5.4 in AWS D1.2 [38]. Some samples have a LOF at the root (example shown in Figure 0-10), which is an impassable discontinuity [37], [38] but for this study, the LOF was treated as a pore defect.

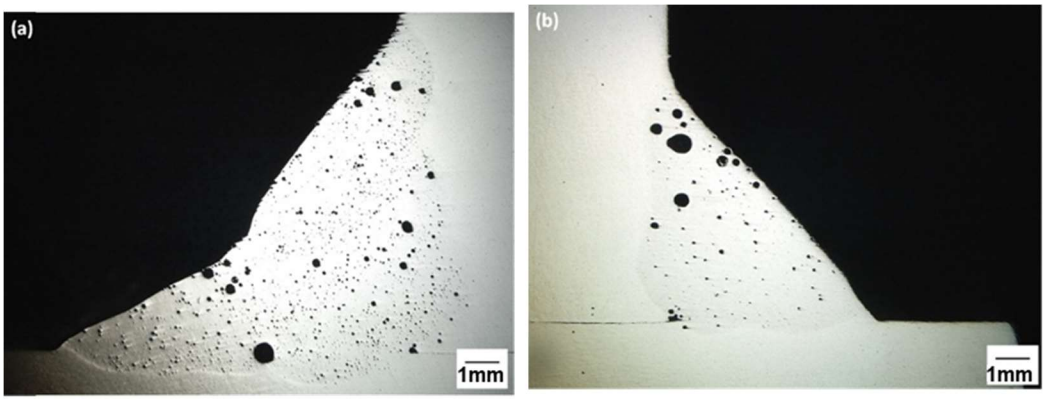

Figure 0-8 – Cross-section of the Al plate-to-plate weld joint. Image (a) shows the multi-pass weld side, and (b) shows the single-pass weld side of the joint. The areal % and total area of porosity for each weld were calculated to be (a) 4.7% and 0.10 mm^2 and (b) 4.4% and 0.05 mm^2, respectively.

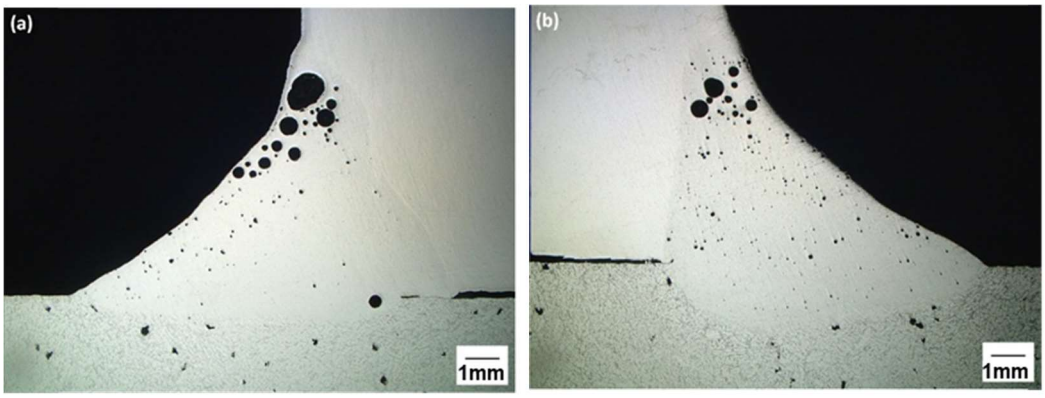

Figure 0-9 – Cross-section of the Al pipe-to-plate weld joint. Images (a) and (b) show each cross-section of this joint when machined down the middle. The areal % and total area of porosity for each weld were calculated to be: (a) 5.8% and 0.07 mm^2 and (b) 3.1% and 0.05 mm^2, respectively.

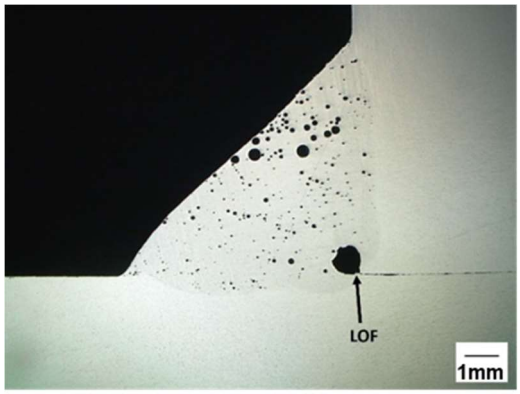

Figure 0-10 – Cross-section of the Al plate-to-plate weld joint. This sample has a LOF at the joint, which will be treated as a pore defect for this work. The areal % and total area of porosity for this weld are 6% and 0.05 mm^2, respectively.

Weld joint defect manufacturing

The objective of the defect manufacturing step is to manually induce a subsurface defect in welds that can be used to test the defect detection capabilities of IR-TNDT. The baseline welds, described in Section 3.2, were used in this portion of the project.

Steel Joints

The method used to manufacture defects in the steel welds are as follows:

- Cu contamination in a notch ground at the root of the weld joint.

This method was the most successful in creating crack defects in the subsurface of the steel welds, as it yielded a subsurface crack while maintaining a passable weld surface. All weld samples from these trials were cross-sectioned, polished to a 1-μm grit finish using the Struers alumina suspension and then macroetched using a 2% nital solution [39]. Representative defects illustrated in the following section have either a 1-μm grit finish or an etched finish, depending on which finish optimally reveals the defect.

This method of defect manufacturing of subsurface cracks in the steel welds included the use of Cu located in a notch at the root of the weld joint. Approximately 100 mg of 99.9% pure Cu shot from Alfa Aesar was placed in the notch before welding. This method was developed by combining Steel Methods 1 and 2 to minimize the subsurface defect's appearance at the weld's surface. A demonstration of the notch and Cu shot placement before welding is shown in Figure 0-11 for the steel plate-to-plate joint.

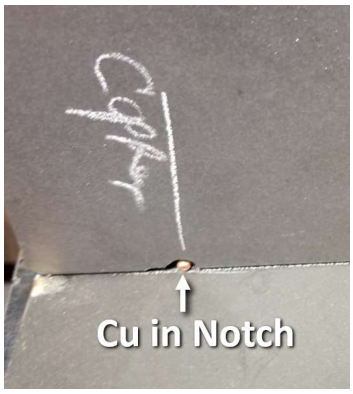

Figure 0-11 – Steel plate-to-plate joint with a Cu shot placed in a notch at the root of the joint before welding.

This method resulted in fewer weld surface discontinuities, unlike Steel Method 1. The present surface disruptions include Cu deposits (by visual observation) at or trailing behind the original Cu location and underfill. These disruptions would likely be considered passable or repairable discontinuities [40]. Minimal weld surface discontinuities ensure that the IR-TNDT is only being tested for its ability to detect the subsurface defect.

The cross-sections of the steel welds where the Cu in notch method was implemented, as shown in Figure 0-12

Figure 0-12, reveal the appearance of surface-breaking and subsurface cracks. These cracks were present in every sample tested and varied in dimension and position. Other discontinuities in these welds, but not in the baseline welds, include porosity, overfill, overlap, and underfill (labeled in Figure 0-12

Figure 0-12). These discontinuities are common in welding and are typically either passable or repairable during weld inspection [40].

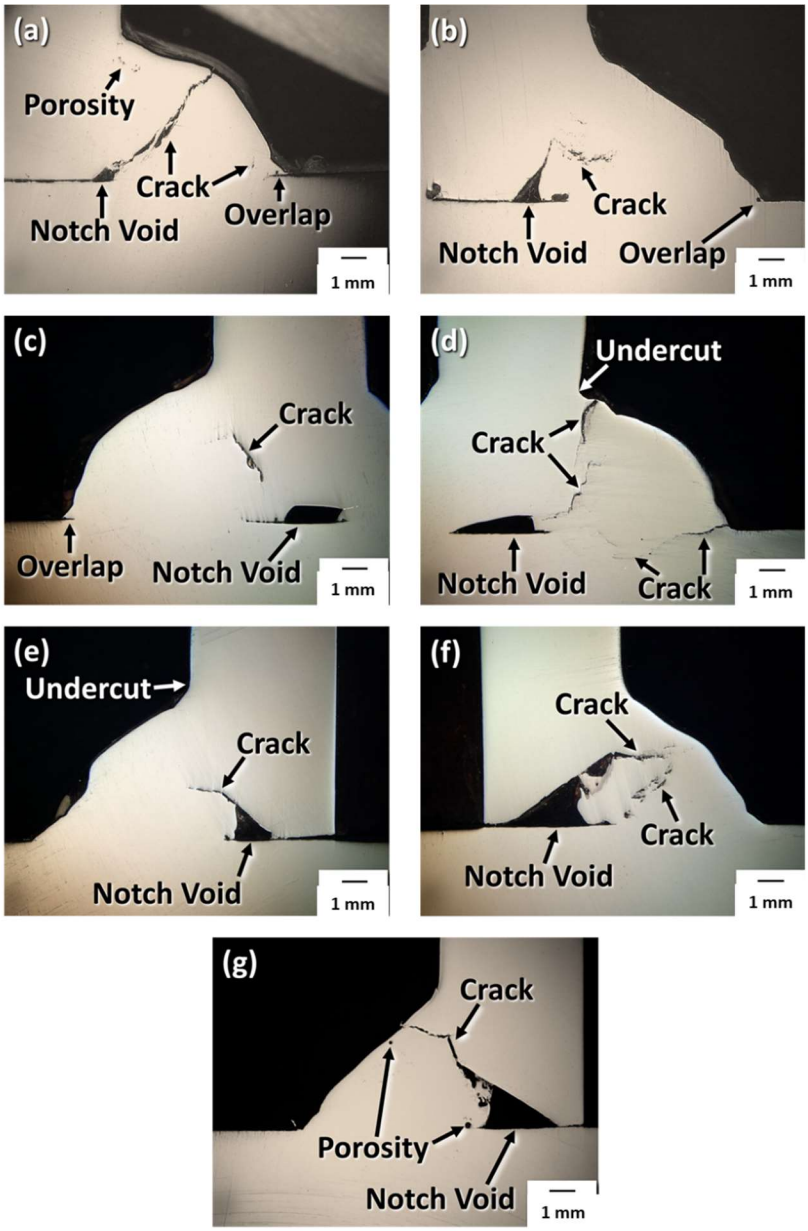

Figure 0-12 – Steel (a-d) plate-to-plate and (e-g) pipe-to-plate weld joint cross-sections where the Cu and notch were placed. All samples resulted in one or more cracks that were subsurface or surface-breaking. In addition to cracks, the defect welds possessed overlap, porosity, and undercut effects.

Aluminum Joints

The methods used to manufacture cracks into the Al welds are as follows:

- Machining a cut in the root of the weld joint.

The welds from these trials were cross-sectioned and then polished to a 0.05-μm grit finish using the Buehler MasterPolish alumina and colloidal silica suspension.

This method utilized a band saw blade to machine a thin cut horizontally through the weld joint. This machined cut serves as the pseudo-crack in the Al welds, and this method will be referred to as the “machined crack” method. The machined crack procedures differed for each Al joint type and will be described in the following sections.

The Al plate-to-plate joint was first welded on one side, and upon completion of that single weld, a band saw was used to machine a cut horizontally through the entirety of the weld joint, as shown in Figure 0-13. Then, a single-pass weld was performed on the other side of the joint, which was the side that was imaged with the IR cameras. Finally, the first side was given two more weld passes to form a multi-pass weld, patching the cut on that side of the joint.

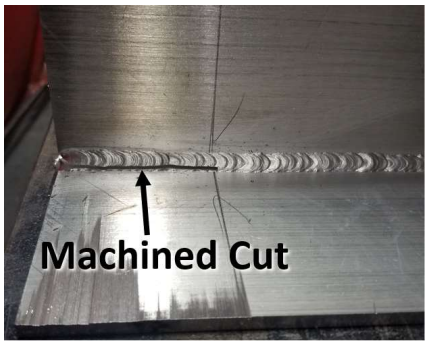

Figure 0-13 – The Al plate-to-plate joint after one side was welded, and then a band saw was used to machine a cut horizontally through the weld.

Subsurface pseudocracks in Al plate-to-plate weld joints were successfully created in-shop by machining a cut into the root of the joint before welding (Figure 0-14).

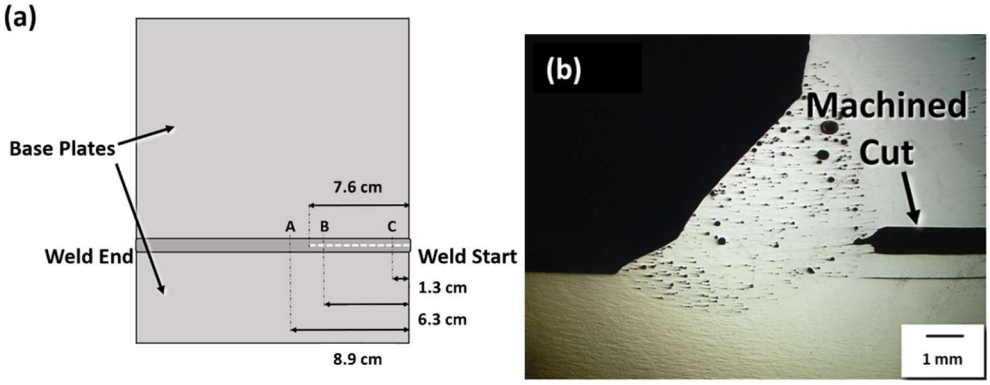

Figure 0-14 – (a) Schematic representation of the machine-cut into the root of the joint before welding to create a subsurface pseudocrack. (b) Cross-sections of the Al plate-to-plate weld joint with a machined cut going through 7.6 cm of the weld.

Surface-breaking drill hole

Several Al plate-to-plate, Al pipe-to-plate, steel plate-to-plate, and steel pipe-to-plate welds were IR tested with enlarged defects machined by a handheld drill with a 1.6-mm

(1/16") drill bit. This created a surface-breaking defect. Figure 0-15 shows a schematic representation of the drilling procedure.

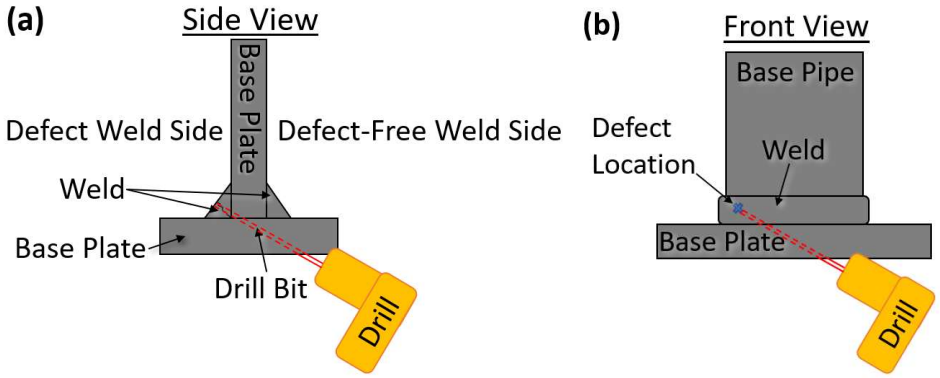

Figure 0-15 – Schematic representation of the drill holes applied to the weld joints using a 1.6-mm (1/16”) diameter drill bit to create a surface-breaking hole. (a) Side view of the plate-to-plate weld joint and (b) front view of the pipe-to-plate weld joint.

Coating application to the steel weld samples

The steel pipe-to-plate and plate-to-plate samples with the surface-breaking drill hole were coated with two protective coatings. Both coatings were applied following the coating manufacturer’s instructions. Before applying protective coatings, all samples underwent a surface preparation procedure, according to SSPC-SP-1 [41]. Welds were wire-brushed to remove residue from the drilling process and cleaned with solvent. The solvent was applied using a wetted rag. The surface was then wiped with a clean and dry rag.

The organic Zinc-it® galvanizing spray was applied inside a fume hood, spraying approximately 30 cm from the sample surface. The weld joint was kept at room temperature upon coating. Steel welds were investigated with 1 and 3 layers of the Zinc-it® spray to address the effect of the coating thickness on defect detection. Following the technical data sheet [42], the wait time between the application of each layer was 8 hours, allowing each layer to dry thoroughly between coatings. Finally, IR-TNDT was performed at least 8 hours after drying the last layer.

The epoxy-based coating, AMERCOAT® 399, required a mixing procedure, which followed the provided product data sheet [43]. Before mixing, each component was homogenized by agitation with compressed air. The mixing ratio was 1:1 base-to-hardener. After 15 minutes, the mixture was applied to the pre-cleaned weld surfaces using a well-loaded brush to avoid air retention. The coating was applied in a fume hood, and the sample’s surface temperature did not exceed 22°C during the procedure. IR-TNDT was performed after at least 4.5 hours of drying.

Textured surface finish of the Al weld samples

The Al weld joints received a surface finish according to the Al standard designations for mechanical finishes provided by FDOT – 2018 Aluminum Association Finishes Manual [44]. Grinding with a 120-grit rub was performed using a DREMEL grinding bit for a directional textured coarse-to-medium satin (between 80- and 220-grit) with a peripheral wheel speed of 6,000 rpm. The final step of manual grinding with 800-grit sandpaper was performed after grinding the weld joint with the DREMEL bit.

IR camera preparation

The FLIR T620 has a higher resolution than the FLIR C5 camera and can resolve a spot size of 0.05 cm from a 25 cm focus distance, while the C5 can only resolve a spot size of 0.5 cm from the same focus distance. These spot sizes were measured using the camera's spatial resolution, or instantaneous field of view (IFOV), and solving for the corresponding spot size at the camera's focus distance and then multiplying that value by 3 since the recommended thermal reading should be taken from the average of at least 3 pixels to minimize the error from optical aberrations [45], [46]. Although higher in resolution, the FLIR T620 costs ~$20-30k, while the FLIR C5 is significantly cheaper, costing ~$700 [47]. A summary of each camera's specifications can be found in Appendix B.

Both the FLIR T620 and C5 cameras were first calibrated to the local environment to compensate for the thermal radiation generated by the surrounding atmosphere, reflections in the moisture in the air, and reflections emitting from the weld joint being imaged. Camera calibration was performed by inputting the following settings into the camera: emissivity (ε), atmospheric temperature, relative humidity, and reflected temperature. These settings were determined using a thermometer and hydrometer in the same area where imaging was performed. A wrinkled sheet of Al foil was used to measure the reflected temperature. Inputting these settings allows the camera to take accurate thermal readings of the target by compensating for the thermal radiation in the surrounding environment [48].

Emissivity was determined by wire-brushing the welds to ensure minimal variation in the emissivity across the weld surface. Therefore, the emissivity was measured based on the wire-brushed finish of the weld surfaces. A carbon steel wire brush was used on the steel welds, and a stainless-steel wire brush was used on the Al welds. The emissivity was measured by placing a highly emissive (~0.97) electrical tape near the weld surface. Next, the weld joint was placed on a hot plate and heated at least 7°C above room temperature. Once stabilized, the temperature of the tape was measured to determine the emissivity of the nearby weld surface. The emissivity values for the weld joints are given in Table 0-2.

Table 0-2 – Measured weld emissivity for the weld joints studied in this work.

Joint Type	Weld Emissivity
Steel A36 plate-to-plate (uncoated)	0.79
Steel A36 plate-to-plate (coated)	0.49
Steel A500 pipe-to-steel A36 plate (coated and uncoated)	0.45
Al extruded 6061-T6 plate-to-plate (untextured and textured)	0.20
Al extruded 6061-T6 pipe-to-Al cast 356-T6 plate (untextured and textured)	0.20

FLIR T620 setup

Figure 0-16 gives a frontal of weld joints and indicates the location of the defect relative to where the lens of the camera will be centered. The dimensions shown in Figure 0-17 for the FLIR T620 setup are based on the plate-to-plate joint configuration. The camera was kept in the same position with respect to the side view for the pipe-to-plate joints.

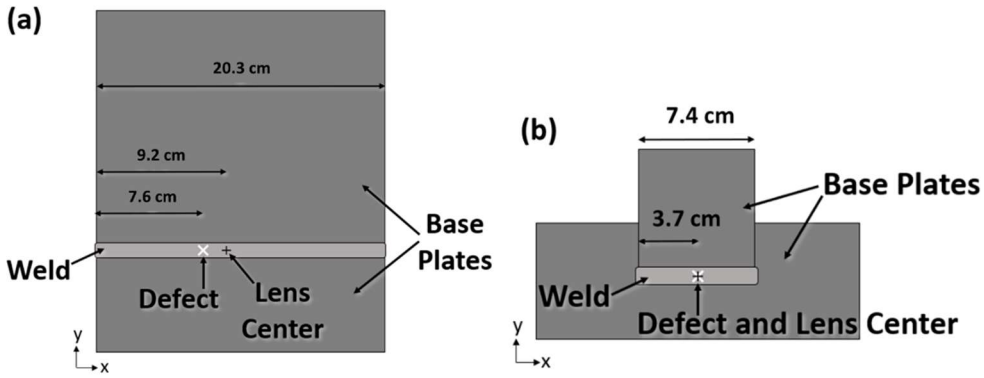

Figure 0-16 – Front view of the two different geometries of weld joints with labels indicating where the defect was located and where the FLIR T620 lens center was positioned. (a) Steel and Al plate-to-plate joint, (b) steel and Al pipe-to-plate joint.

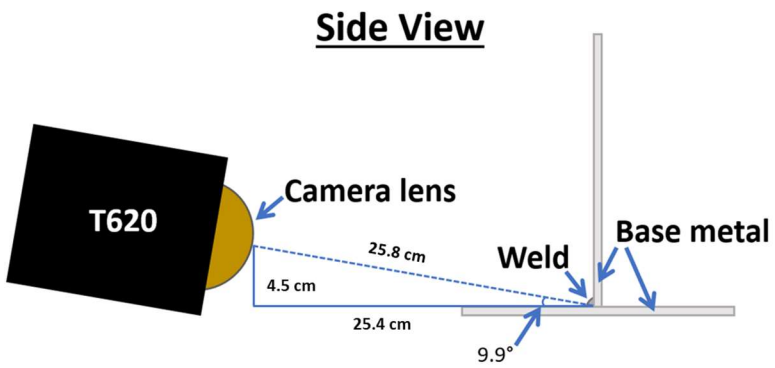

Figure 0-17 – Side view of the setup for the FLIR T620 camera based on the plate-to-plate weld joint.

FLIR C5 setup

The FLIR C5 camera was positioned at an equivalent distance used for imaging with FLIR T620, as illustrated in Figure 0-18. IR images were captured manually every 30 seconds since the C5 camera does not allow an automatic acquisition rate. All infrared images were analyzed using the native software provided on the FLIR website [49].

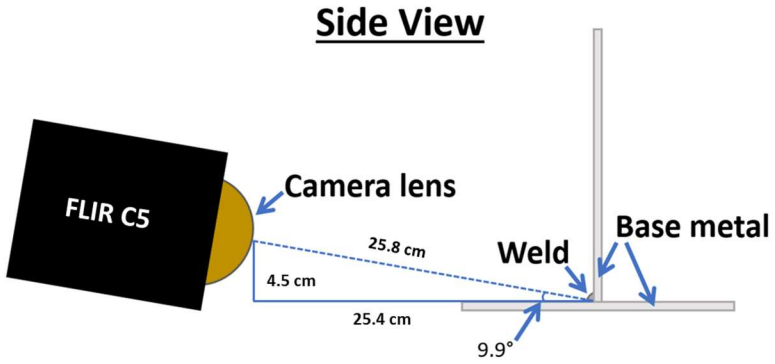

Figure 0-18 – Side view of the setup for the FLIR C5 camera based on the plate-to-plate weld joint.

Sample heating

When using the active thermography technique for the NDT of weld joints, the sample must be preheated to obtain an IR thermal image. Two common types of portable heating equipment are heat guns and flame torches. The heat gun allows for tunable temperature control, so it was chosen for use in this work instead of the flame torch to minimize thermally-induced damage to the samples.

The test temperatures for the steel samples were designed not to exceed those where the mechanical performance of the A36 and A500 steel could be affected. In A36 and A500 steels, tensile and yield strength loss begins at 500°C, and creep begins at 370°C [50], [51]. However, the applied organic coatings present a maximum temperature resistance, above which the coating properties degrade. Thus, the maximum

temperature reached during IR-TNDT of the uncoated and the Zinc-It® coated steel samples was 160°C, while the epoxy-based coated steel weld joints were heated up to 93°C. Test temperatures were set in this study to reflect those that could be obtained during in-field inspections and accommodate potential temperature fluctuations during the heating, not damaging either the base material or coating layers. The test temperatures were pre-defined for the Al weld joints and did not exceed 160°C for the uncoated samples and textured surface. Table 0-3 summarizes the sample test matrix.

Table 0-3 – A listing of the sample population to be tested and the maximum test temperature used in the study.

Sample	Sample Description	Max. Test Temperature
Al Pipe-to-Plate Weld Joint	Surface-breaking drill hole, uncoated	160°C
	Surface-breaking drill hole, textured surface finish	160°C
Al Plate-to-Plate Weld Joint	Surface-breaking drill hole, uncoated	160°C
	Surface-breaking drill hole, textured surface finish	160°C
Al Plate-to-Plate Weld Joint	Subsurface pseudocrack, uncoated	160°C
	Subsurface pseudocrack, textured surface finish	160°C
Steel Pipe-to-Plate Weld Joint	Surface-breaking drill hole, uncoated	160°C
	Surface-breaking drill hole, Epoxy-based coating	93°C
	Surface-breaking drill hole, Zinc-It spray coating – 1 layer	160°C
	Surface-breaking drill hole, Zinc-It spray coating – 3 layers	160°C
Steel Plate-to-Plate Weld Joint	Surface-breaking drill hole, uncoated	160°C
	Surface-breaking drill hole, Epoxy-based coating	93°C
	Surface-breaking drill hole, Zinc-It spray coating – 1 layer	160°C
	Surface-breaking drill hole, Zinc-It spray coating – 3 layers	160°C

Figure 0-19 depicts the heating positions for the two weld joint geometries, where the red circle indicates where the heat gun nozzle will be placed. Once the weld reached the target test temperature, it was held for an additional 30 sec to equilibrate the sample. Then, the heat gun was removed, and IR imaging immediately ensued. The

measuring spot in the camera interface was placed on top of the defect to measure the temperature.

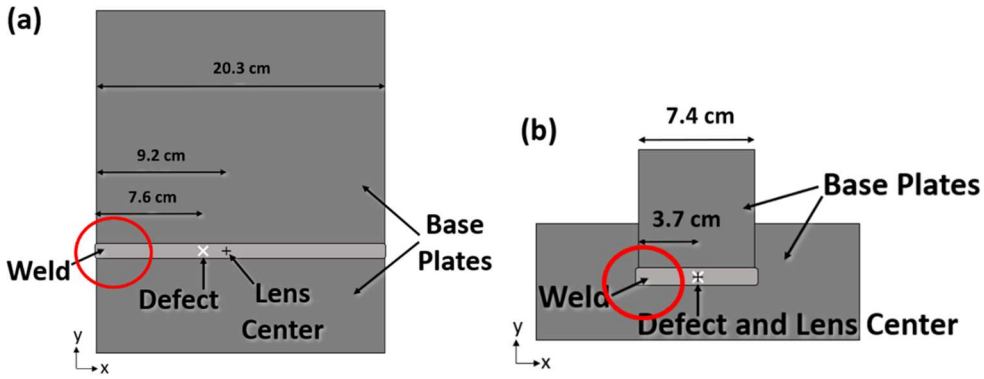

Figure 0-19 – Schematics indicating the location of the heat gun nozzle on both weld joints geometries when heating. (a) Steel and Al plate-to-plate weld joint, (b) steel and Al pipe-to-plate weld joint.

IR imaging and IR image analysis

Infrared images were taken every 15 seconds for the Al samples and every 30 seconds for the steel samples until the sample cooled to 35°C. The temperature measurement during the cool-down was taken by positioning the measuring spot on top of the drilled hole. For the subsurface pseudocrack, the measuring spot was placed at the beginning of the machined region. The visual analysis examined any discontinuities in the weld thermal signal in regions with known defects. This technique simulates the investigation performed in the field, as represented in the trial assembly shown in Figure 0-20.

Figure 0-20 – Photography of the trial assembly, showing sample, camera, and heat gun positioning.

The images were analyzed using the proprietary software available on the FLIR website [49]. The software allows the images to be organized into libraries, which can be shared between multiple users.

Destructive tests for optical microscopy

Five weld samples were selected for destructive quantitative analysis:

- Al pipe-to-plate weld joint with a surface-breaking drill hole
- Al plate-to-plate weld joint with a surface-breaking drill hole
- Al plate-to-plate weld joint with a subsurface pseudocrack
- Steel plate-to-plate weld joint with a surface-breaking drill hole
- Steel pipe-to-plate weld joint with a surface-breaking drill hole.

The samples were cross sectioned using a high-speed bandsaw. Final cuts before grinding and polishing were performed using a precision low-speed saw with a diamond blade. For metallographic examination, successive SiC abrasive papers from 320 to 1200 grit were used for grinding to reach the cross-section of the detected defects and reveal the weld features. The final polishing step was performed with 6 μm diamond paste. Polished samples were characterized using an optical microscope. The open-source image processing software, Image J, was used to analyze defects dimensions.

Chapter 4 Results

In-shop infrared trials

The welded samples underwent a mock in-field inspection to determine if the IR-TNDT method could locate the defects after in-shop welding. This section provides a visual analysis of the IR images. Each image shows the emissivity (ε), temperature scale, welding direction, and observed welding artifacts.

Steel plate-to-plate weld joint

The IR images from two baseline defect-free control samples, and steel plate-to-plate weld joint samples that were taken using the FLIR T620 camera are given in Figure 0-1(a-b). The observed weld artifacts include slag and weld spatter.

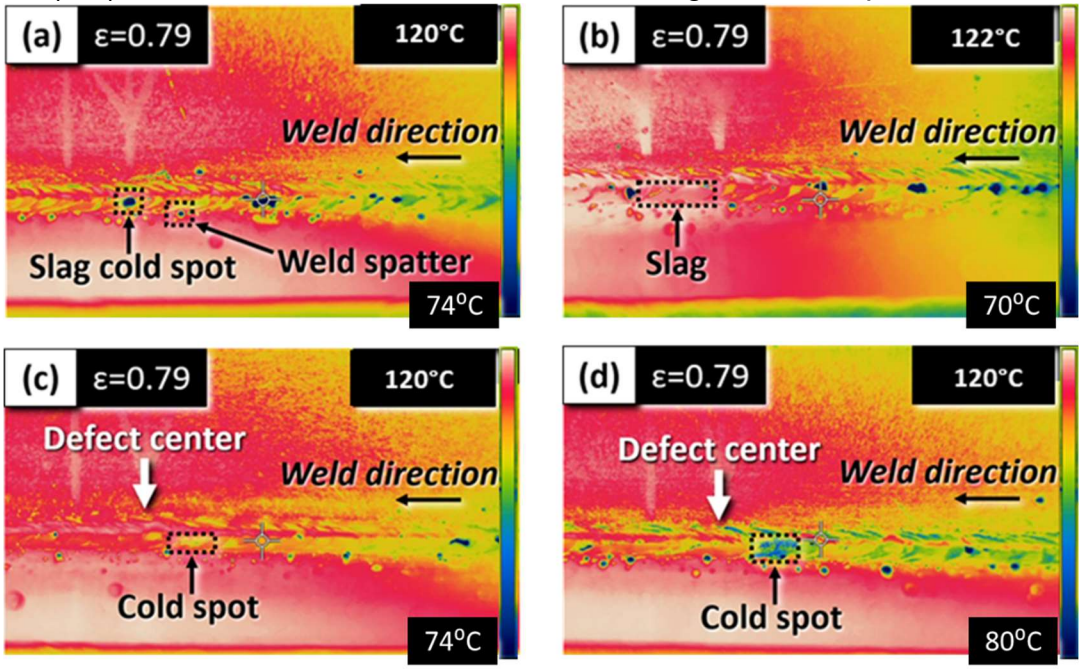

Figure 0-1(b-c) shows representative IR images from two of the twelve defect steel plate-to-plate weld joints. The defects in the steel plate-to-plate joints have subsurface cracks formed by a Cu contaminant in the root of the joint. These images show a white arrow above the weld region where defects were placed (labeled defect center). The defects were not visually detectable in steel plate-to-plate joints using the FLIR T620 camera.

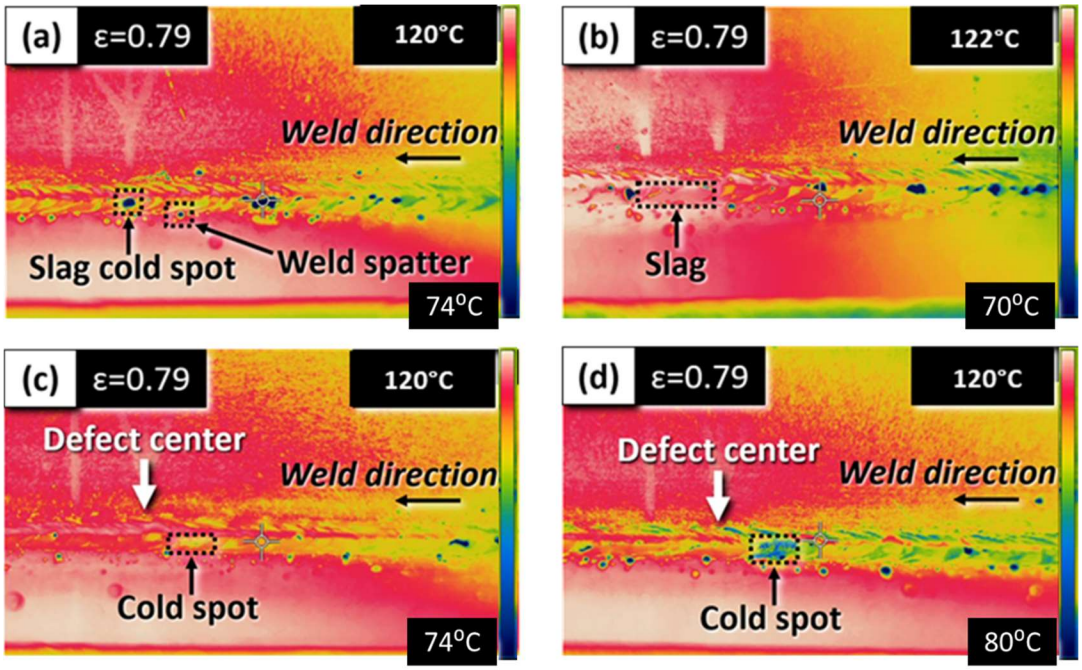

Figure 0-1 – (a-b) The defect-free IR images of the steel plate-to-plate joint using the FLIR T620 camera. (c-d) The FLIR T620 IR images of the steel plate-to-plate joints with manufactured subsurface cracks from a Cu contaminant (defect location labeled). The emissivity (ε) that the user sets in the camera is shown on the top left and on the right of the image is the corresponding temperature scale color scheme, which is automatically performed by the camera.

The defect-free IR images from the FLIR C5 are shown in Figure 0-2(a-b). The weld artifacts include cold spots from regions where slag was present. Representative IR images of two of the twelve weld joints with defects for the FLIR C5 are shown in Figure 0-2(c-d). The defects were not visually detectable in the steel plate-to-plate joints using the FLIR C5 camera.

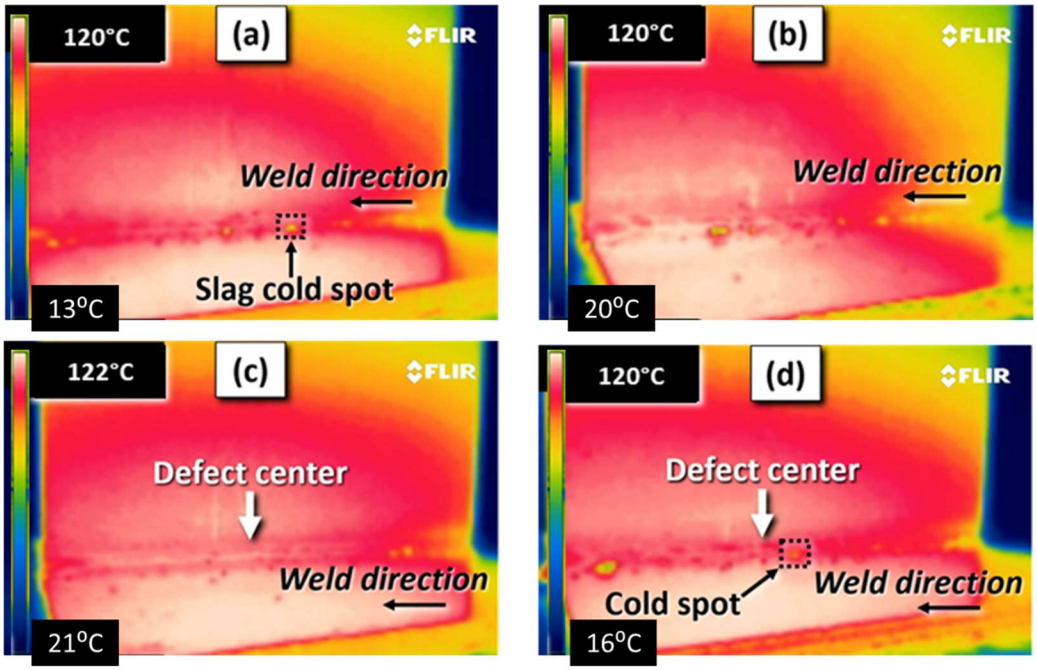

Figure 0-2 – (a-b) The defect-free IR images of the steel plate-to-plate joint using the FLIR C5 camera. (c-d) The FLIR C5 IR images of the steel plate-to-plate joints with manufactured subsurface cracks from a Cu contaminant (defect location labeled). The temperatures on the left of the images correspond to the temperature scale color scheme which is automatically performed by the camera.

Steel pipe-to-plate weld joint

The IR images from the two defect-free steel pipe-to-plate weld joint samples that were taken using the FLIR T620 camera are given in Figure 0-3(a-b). Representative IR images from two of the twelve defect steel pipe-to-plate weld joint samples that were taken using the FLIR T620 camera are provided in Figure 0-3(c-d). The defects in the steel plate-to-plate joints are subsurface cracks formed by a Cu contaminant in the root of the joint. These images show an arrow indicating the location of the defect center. Figure 0-4 shows an optical image of slag covering the defect center, thus obscuring the subsurface defect in Figure 0-3(c). The defects were not visually detectable in the steel pipe-to-plate joints using the FLIR T620 camera.

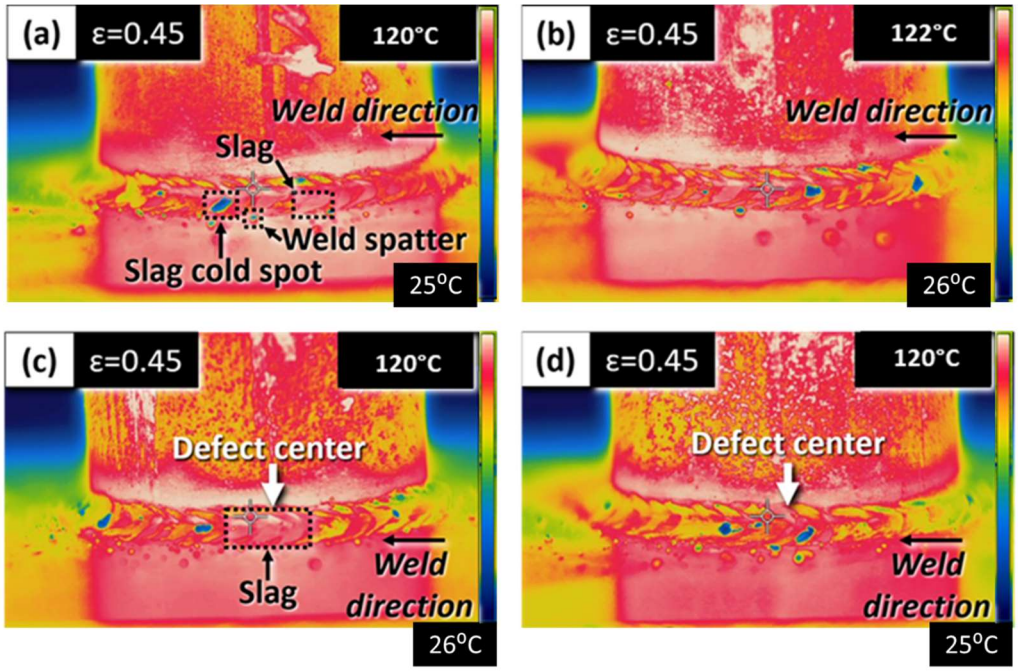

Figure 0-3 – (a-b) The defect-free IR images of the steel pipe-to-plate joint using the FLIR T620 camera. (c-d) The FLIR T620 IR images of the steel pipe-to-plate joints with manufactured subsurface cracks from a Cu contaminant (defect location labeled). The emissivity (ε) that the user sets in the camera is shown on the top left and on the right of the image is the corresponding temperature scale color scheme, which is automatically performed by the camera.

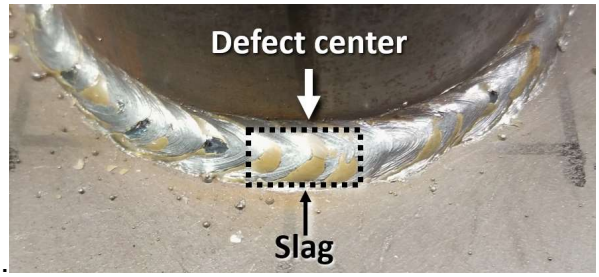

Figure 0-4 – Optical image of the steel pipe-to-plate weld joint with slag over the defect center corresponding to the IR image in Figure 35(c).

The defect-free IR images from the FLIR C5 are shown in Figure 0-5(a-b). Weld artifacts include cold spots from regions with slag in the images. Representative IR images of two of the twelve weld joints with defects for the FLIR C5 are shown in Figure 0-5(c-d). These images show a white arrow above the weld region where defects were placed (labeled defect center). The defects were not visually detectable in the steel pipe-to-plate joints using the FLIR C5 camera.

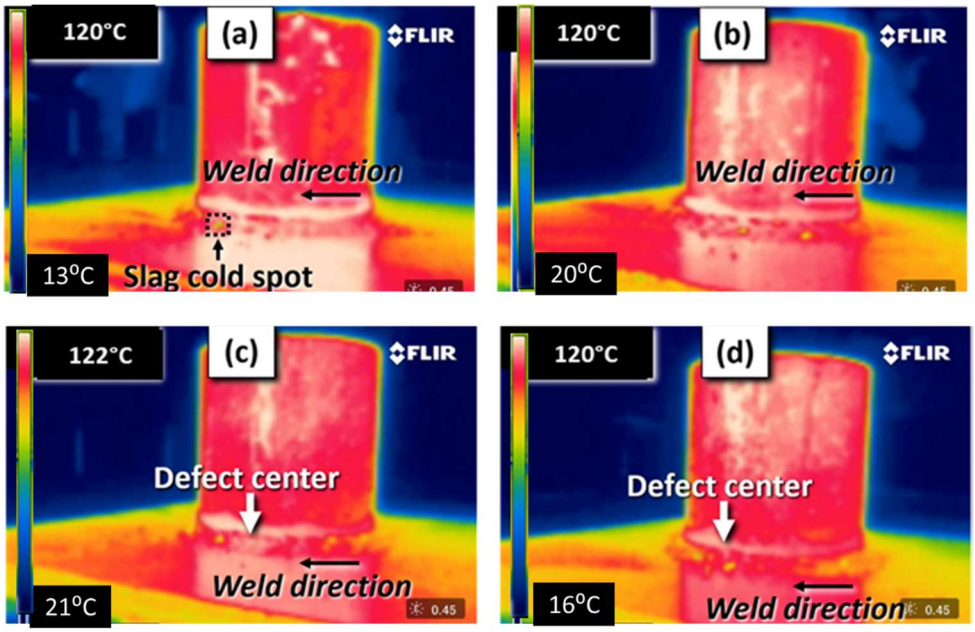

Figure 0-5 – (a-b) The defect-free IR images of the steel pipe-to-plate joint using the FLIR C5 camera. (c-d) The FLIR C5 IR images of the steel pipe-to-plate joints with manufactured subsurface cracks from a Cu contaminant (defect location labeled). The temperatures on the left of the images correspond to the temperature scale color scheme, which is automatically performed by the camera.

Potential challenges in identifying defects in the steel joints

Analysis of the steel weld joint IR images did not identify the subsurface cracks in any of the steel welds IR imaged. One of the challenges in identifying the thermal signal from the cracks is the presence of weld artifacts that produces a thermal signal. These weld artifacts include thermal gradients, slag, slag cold spots, weld spatter, and residual Cu melting into sound regions of the weld. Thermal gradients were present in the steel plate-to-plate joints, and slag, cold spots, and weld spatter were present in both types of steel weld joints despite being wire-brushed before imaging. An example of the slag in an optical image is given in Figure 0-6. Slag may interfere with analysis by blocking the thermal signal of the weld behind it. For some samples, this slag obscured the defect location.

To determine the impact of the thermal signal from the slag, the FLIR Tools software was used to measure the average temperature of a 4x4 pixel box within a slag spot and in a non-slag weld zone vertical to it, as demonstrated in Figure 0-7. The average temperature of the pixels measured in the slag spot was 115°C, and the average temperature of the pixels measured in the non-slag zone was 112°C when the emissivity of the weld was used. However, there is a difference in emissivity between the slag and non-slag zone, which can result in incorrectly calculated temperature readings from the camera. Suppose the emissivity of the slag is only 0.06 higher than the surrounding weld, as it has a less reflective finish. If this new emissivity is used, the calculated average temperature of the pixels in the slag zone decreases by 12°C

(calculated using FLIR Tools software). Therefore, artifacts on the weld, such as slag, with varying emissivity from the weld will result in errors in the temperature readings since the emissivity used in the camera's calculations is that of the weld. This creates challenges in quantifying subsurface crack defects.

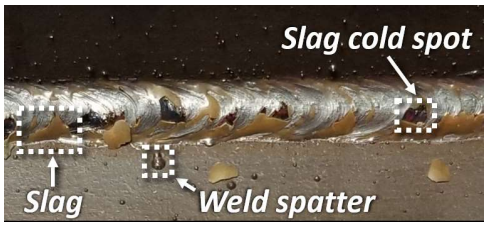

Figure 0-6 – Optical image of the baseline sample steel plate-to-plate weld joint with labels showing examples of slag, cold spots (regions where slag spontaneously removed from the weld during cool-down), and weld spatter.

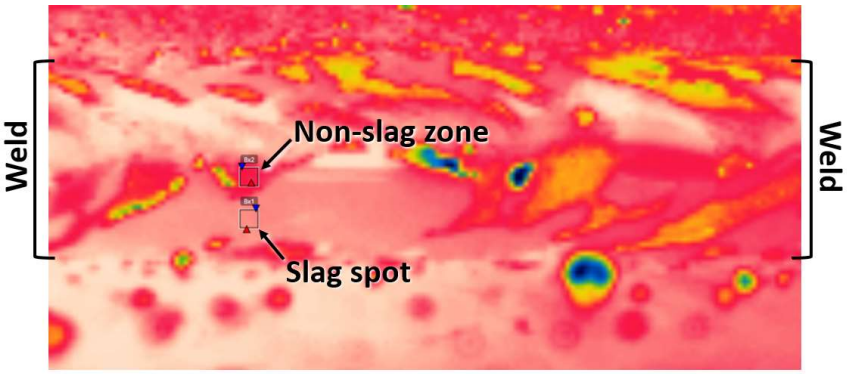

Figure 0-7 – The steel plate-to-plate weld joint with a 4x4-pixel box over a slag spot and a non-slag spot to measure the average temperatures of those regions. The slag spot box average temperature was 115°C, and the non-slag spot box average temperature was 112°C.

In addition to the slag, there are regions where slag was present on the weld but spalled during cooling. These regions are referred to as cold spots. These spots result in weld metal with a different surface finish (emissivity) than the surrounding weld metal, as shown in Figure 0-6. For some weld samples, these cold spots can also be present in the regions of interest, e.g., defective location.

To determine the impact of the thermal signal from the cold spots, the FLIR Tools software was used to measure the average temperature of a 4x4 pixel box placed in the slag cold spot and compared to another 4x4 pixel box of the surrounding weld metal above it, as demonstrated in. Figure 0-8. The average temperature of the pixels over the slag cold spot was 51°C, while the average temperature in the non-slag zone was 107°C. As a result, these cold spots result in a significant temperature differential from the surrounding weld metal and will disrupt the temperature readings taken from the weld. In addition, the cold spots have a different emissivity than the surrounding weld, which will result in incorrect temperature readings.

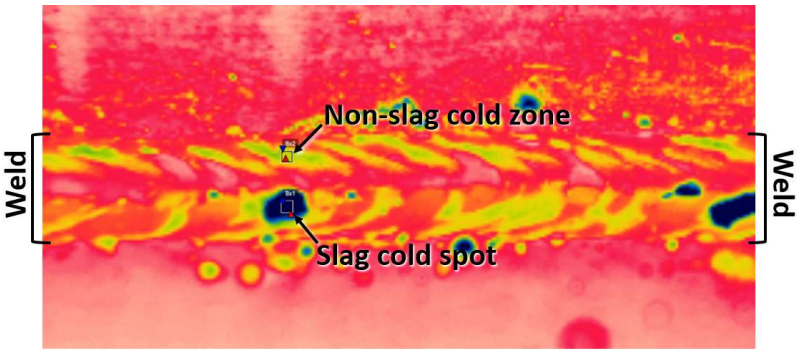

Figure 0-8 – The steel plate-to-plate weld joint with a 4x4-pixel box over a slag cold spot and a non-slag cold spot to measure the average temperatures of those regions. The cold spot box average temperature was 51°C, and the non-slag cold spot box average temperature was 107°C.

Weld spatter was another welding artifact found to cause a thermal signal in the steel welds. To determine the impact of the thermal signal from the weld spatter, the FLIR Tools software was used to measure the average temperature of a 4x4 pixel box within a region of weld splatter and compare it to a 4x4 pixel box placed in the surrounding weld metal above it, as demonstrated in Figure 0-9. The average temperature of the pixels in the weld spatter box was 77°C, while the average temperature in the non-weld spatter zone was 109°C. Similar to the cold spot, the weld spatter results in a significant temperature differential from the surrounding weld metal.

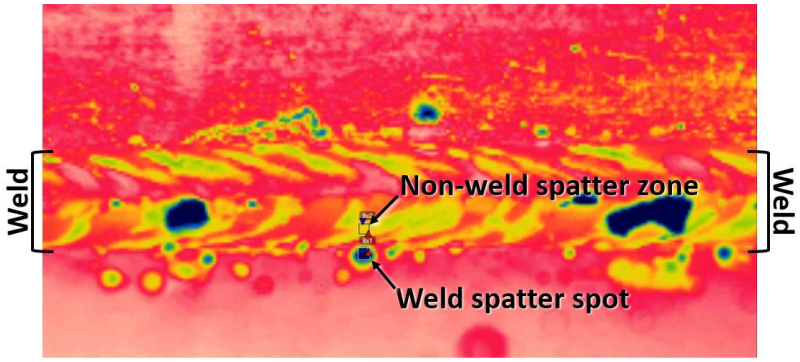

Figure 0-9 – The steel plate-to-plate weld joint with a 4x4-pixel box over a weld splatter spot and a non-weld splatter spot to measure the average temperatures of those regions. The weld splatter spot box average temperature was 77°C, and the non-weld splatter spot box average temperature was 109°C.

A weld artifact present in the FLIR T620 IR images and most of the FLIR C5 IR images of the steel plate-to-plate joints with artificial defects was a cold spot region located near

the defect center labeled in

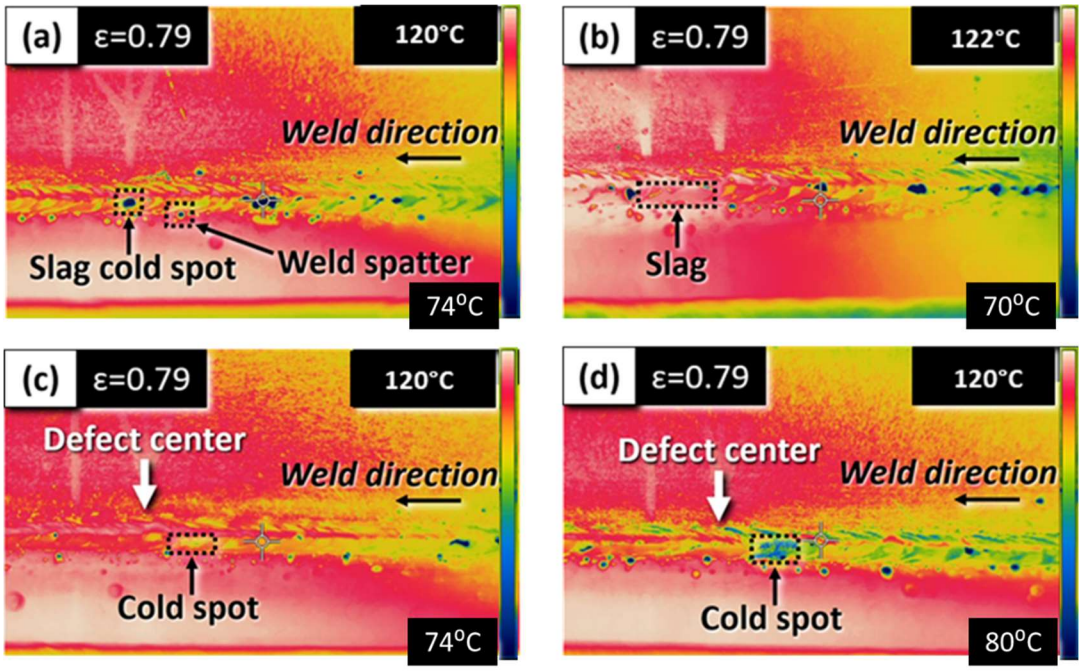

Figure 0-1(c-d) and Figure 0-2d. This cold spot region is marked in the optical image of a defective weld in Figure 0-10. This sample was polished using the Buehler MasterPolish 0.05-μm grit alumina and silica suspension and etched with 2% nital, shown in Figure 0-11. Etching revealed a phase separation between the weld metal and a portion of Cu that melted away from the defect center. The Cu melting on the top of the weld creates a cold spot in the IR images due to having a higher thermal conductivity than the steel, which results in that region cooling faster than the rest of the weld around it [52].

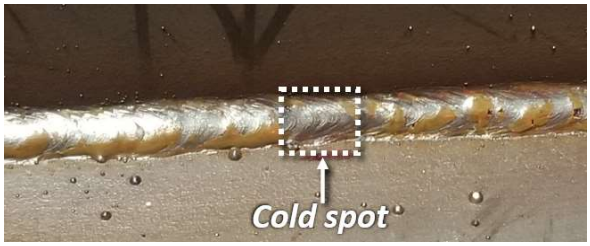

Figure 0-10 – Optical image of the defect sample steel plate-to-plate weld joint with a label showing the cold spot location.

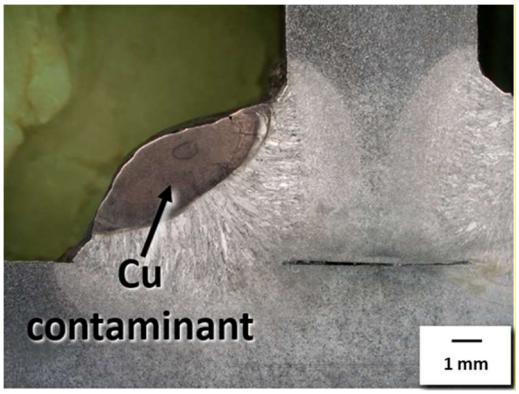

Figure 0-11 – Cross-section of the steel plate-to-plate defect weld joint where the cold spot was present in the IR images, labeled as Cu contaminant. A portion of Cu from the defect center melted backwards into this region, and this phenomenon resulted in the cold spots in the defect weld joint IR images.

This cold spot does reveal the ability of IR to qualitatively show regions of different thermal conductivities, especially due to elemental contamination. All FLIR T620 IR images of the defective steel plate-to-plate weld joints had the presence of the cold spot produced from the Cu deposits. All FLIR C5 IR images showed a cold spot except for one sample.

To summarize, there were no thermal indications of the subsurface crack defects in the IR images of the steel joints. There was difficulty detecting the steel joint defects due to weld artifacts throughout the tested weld joints. These artifacts include thermal gradients, slag, cold spots, and weld spatter. The joints with defects also had a cold spot generated by the Cu contaminant, which does not indicate the presence of the subsurface crack defects but reveals the IR's ability to give a qualitative indication of regions within a weld of varying thermal conductivities. The defect may become detectable if the steel joints receive a finishing treatment during the in-field phase using a wire or grinding wheel to remove surface flaws. Additionally, defect detection may still be possible for the steel plate-to-plate joint if other IR image analysis techniques are explored, including quantitative methods.

Al plate-to-plate weld joint

The IR images from the two baseline defect-free Al plate-to-plate weld joint samples that were taken using the FLIR T620 and C5 cameras are shown in Figure 0-12. These images show the temperature scale, the direction of welding, emissivity (ε), and a thermal signal from the permanent marker line indicating the location of the defect. A weld discontinuity where less weld mass was present in regions of the weld, called underfill, is represented in both defect-free samples. The locations of underfill are labeled in the IR image of defect-free (Figure 0-12(a-b)) but not marked in the IR image of defect-free (Figure 0-12(c-d)) because it is present throughout the entirety of the portion of weld shown in the IR image.

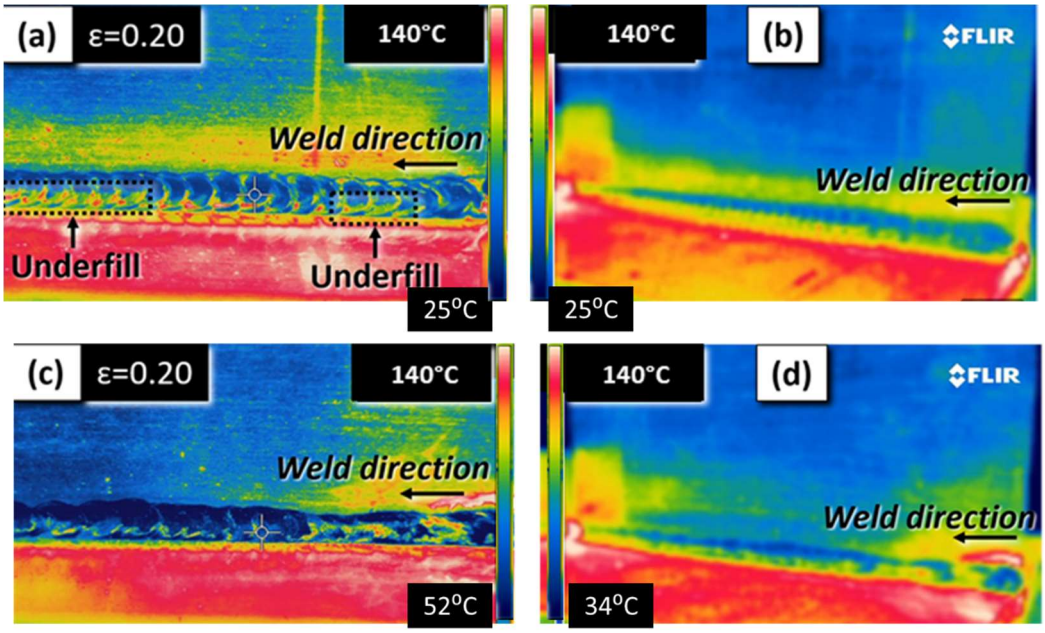

Figure 0-12 – (a-b) The baseline IR images of the Al plate-to-plate weld joints with less underfill and (c-d) with more underfill. The emissivity (ε) that the user sets in the camera is shown on the top left and the corresponding temperature scale color scheme, which is automatically performed by the camera.

The defects in the Al plate-to-plate joints were detectable in all defect weld joints tested using both IR cameras. The FLIR T620 and C5 IR images of one of the Al plate-to-plate defect weld joints are shown in Figure 0-13(a-b). The defects in the Al plate-to-plate joints are machined cuts made at the root of the joint before welding, which act as a subsurface pseudocrack. These images show the temperature scale, the direction of welding, and a bracket indicating the location of the defect. A hotter thermal signal is present in the FLIR T620 IR image where the defect is located, in contrast to the defect-free weld joint IR image (Figure 0-13a)), which has a similar occurrence of underfill in it to this defect sample.

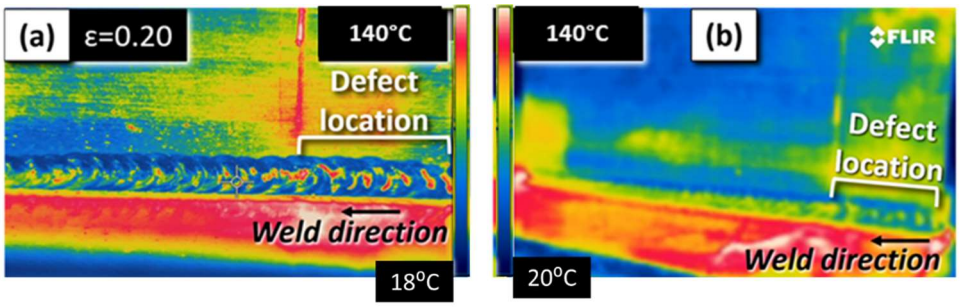

Figure 0-13 – The IR images of the defect sample Al plate-to-plate weld joint with a manufactured subsurface machined cut (defect location labeled). (a) FLIR T620 IR image of the defect sample weld joint. (b) FLIR C5 IR image of the defect sample weld joint. The emissivity (ε) that the user sets in the camera is shown on the top left and on the right of the image 'a' and left in 'b' is the corresponding temperature scale color scheme, which is automatically performed by the camera.

The ability to observe the thermal signal from the pseudocrack is attributed to all the tested welds with defects having a consistent weld mass. This resulted in a continuous thermal signal pattern from the non-defect weld zones. Furthermore, a lack of welding artifacts that generate thermal signals improved defect detectability.

Al pipe-to-plate weld joint

The FLIR T620 and C5 IR images from one of the two defect-free Al pipe-to-plate weld joint samples are given in Figure 0-14(a-b). These images show the temperature scale, the direction of welding, a thermal signal from the permanent marker lines indicating where the defect would begin, and a hot spot present in all welds tested of this joint type. The FLIR T620 and C5 IR images of one of the nine defect Al pipe-to-plate weld joints are shown in Figure 0-14(c-d). The defects in the Al pipe-to-plate joints are machined cuts made at the root of the joint before welding, which act as a subsurface pseudocrack. These images show the temperature scale, the direction of welding, a bracket over the marker lines indicating the location of the defect, and the hot spot in the welds. The defects were not visually detectable in the Al pipe-to-plate joints using either IR camera.

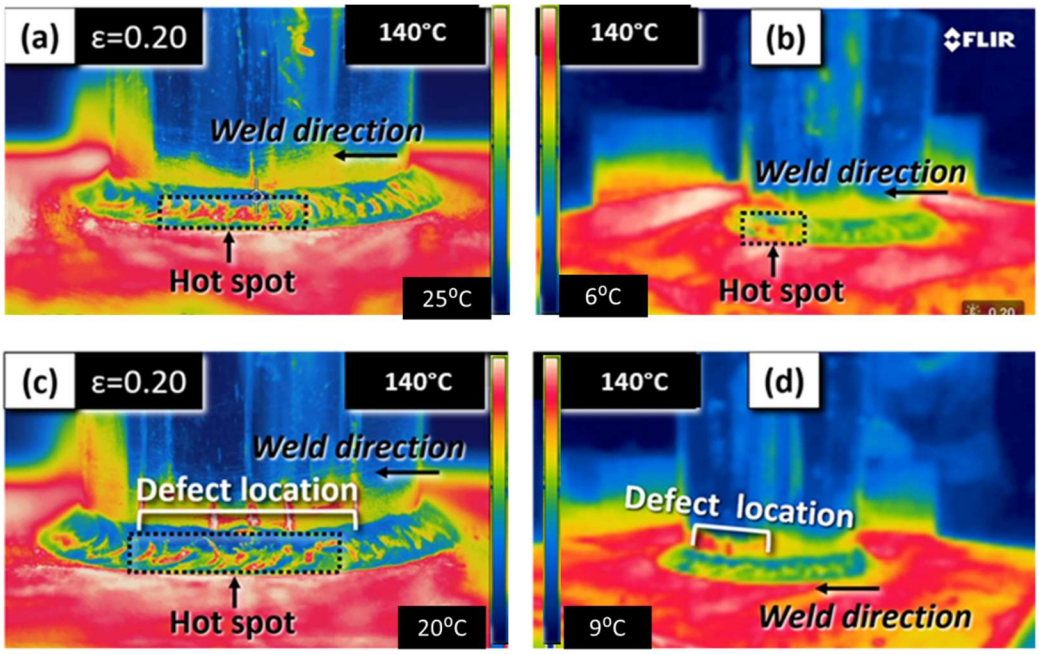

Figure 0-14 – (a-b) The IR images of the defect-free Al pipe-to-plate weld joint. (c-d) The IR images of the defect in Al pipe-to-plate weld joint with a manufactured subsurface machined cut (defect location labeled). The emissivity (ε) that the user sets in the camera is shown on the top left, and each image shows the corresponding temperature scale color scheme, which is automatically performed by the camera.

Potential challenges in identifying defects in the Al joints

In the Al plate-to-plate weld joints, despite the slight visual indication of the machined subsurface pseudocrack, there were thermal signals from underfill that could be falsely identified as a defect signal. In the Al pipe-to-plate joints, defects could not be identified. A possible challenge in visually identifying the defect thermal signal comes from the hot spots in the central weld region of every defect-free and defected weld joint tested.

There are qualitative differences between the thermal signals in the two defect-free Al plate-to-plate weld joints tested (Figure 0-12). These differences in the thermal signal are attributed to varying amounts of underfill present in each defect-free joint. Specifically, the defect-free weld joint (Figure 0-12(c-d)) has a higher occurrence of underfill than the defect-free weld joint (Figure 0-12(a-b)). The underfill indicates less weld mass than the surrounding weld metal, which will result in differences in thermal diffusivity. Optical images of the two baseline joints are shown in Figure 0-15 and include locations of weld underfill. Although the defects were always detectable, some joints also produced thermal signals in the sound regions of the weld where underfill was present that could be falsely identified as a defect.

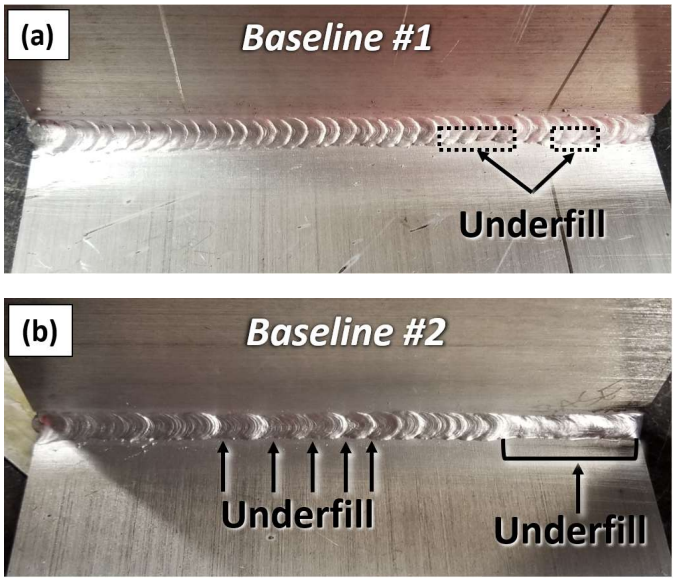

Figure 0-15 – Optical images of the two baseline Al plate-to-plate weld joints. (a) The baseline weld joint has some occurrences of underfill. (b) The baseline weld joint has a more frequent occurrence of underfill.

In all the baseline and defect Al pipe-to-plate weld joints tested, there was a hot spot present in the central region of the welds IR imaged. Two more sound weld joints were produced to analyze the presence of this hot spot. The IR images from these two sound weld joints are shown in

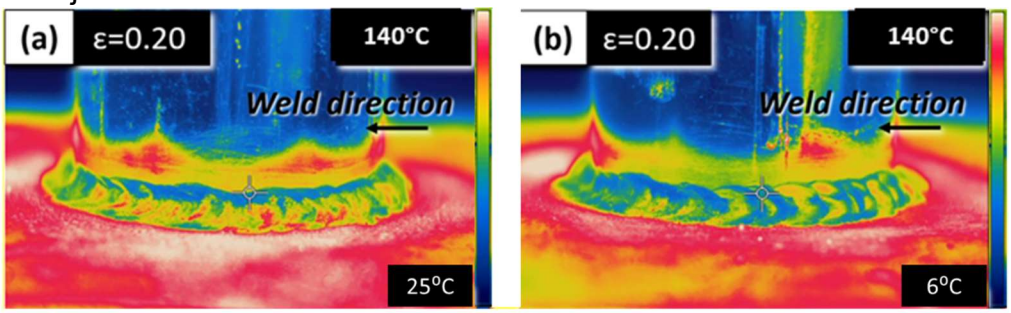

Figure 0-16. In the sound weld joint shown in

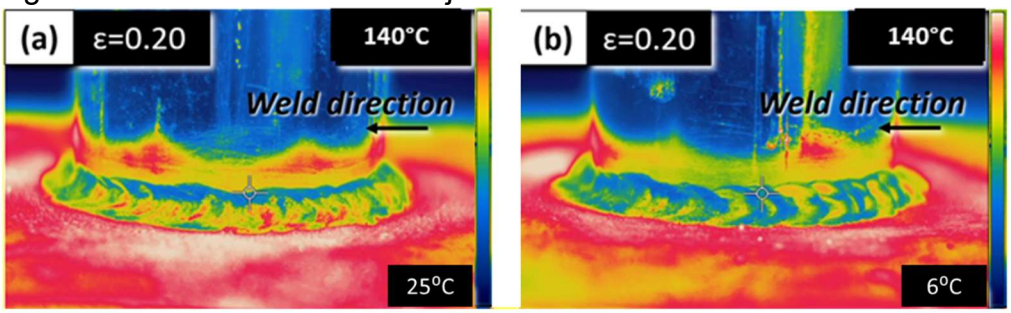

Figure 0-16(a), baseline, the hot spot is present, but in the other sound weld joint shown in

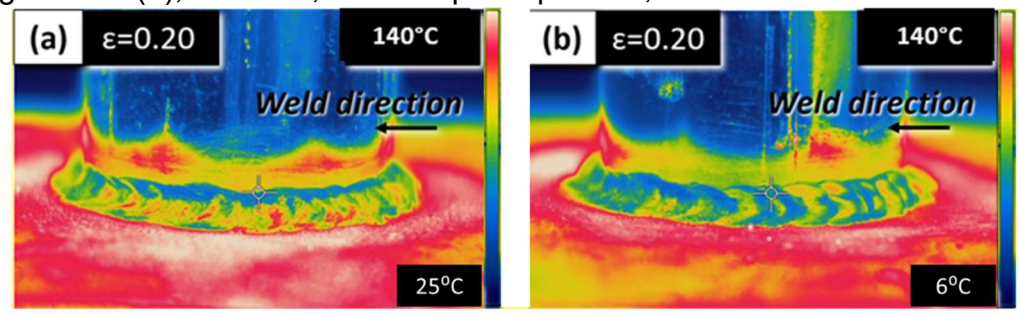

Figure 0-16(b), baseline, there is not a hot spot.

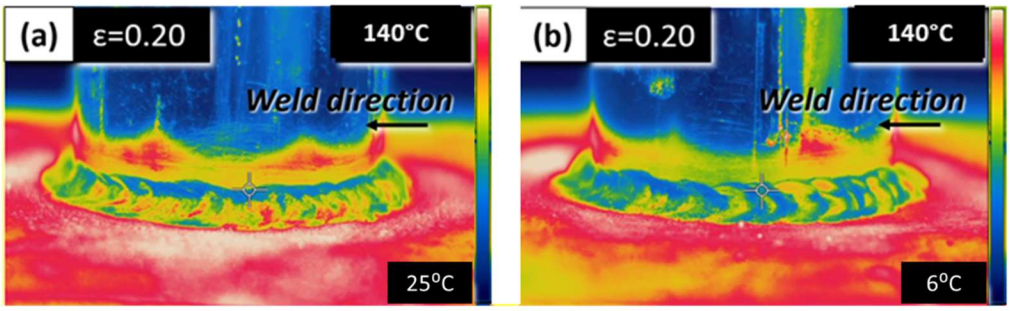

Figure 0-16 – FLIR T620 IR images of two additional baseline (defect-free) Al pipe-to-plate weld joints tested to further analyze the hot spot present in this joint type. (a) IR image of the baseline weld joint with the hot spot present. (b) IR image of the baseline weld joint imaged without a hot spot. The emissivity (ε) that the user sets in the camera is shown on the top left and on the right of the image is the corresponding temperature scale color scheme, which is automatically performed by the camera.

Despite a correlation between longer weld times and the presence of the hot spot, the relative location of the hot spot in those joints is stochastic. In the baseline, the hot spot is more centralized, while in defect (Figure 0-14(c-d)) and baseline sample (

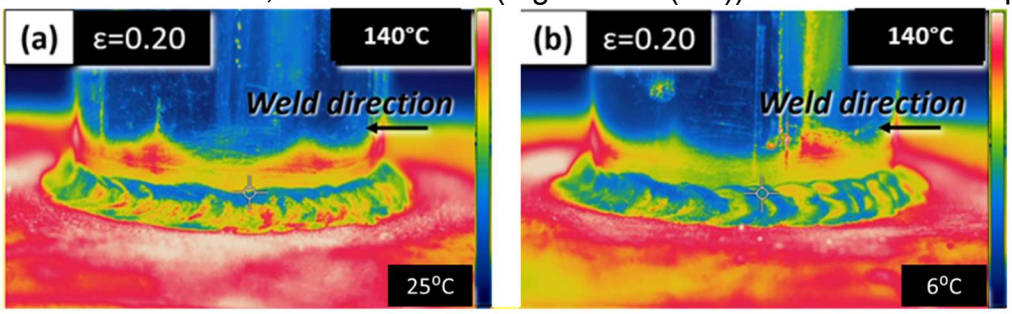

Figure 0-16a)), the hot spot is spread throughout most of the weld pass imaged. This makes it challenging to place the defect in a location that would not have the hot spot present to determine if the defect can be visually detected without obstruction from the hot spot.

A hot spot in all the baseline and defect Al pipe-to-plate weld joints makes it challenging to identify the defect visually. In addition to the time to weld the joint influencing the presence of the hot spot, other weld parameters can vary the heat input in the welds. An example of a welding parameter that could lead to a higher heat input in some areas of the weld is increased electrode extension, where the electrode extension is the distance between the end of the electrode and the end of the gun tip [53]. This parameter may vary more in a joint with curvature, such as when manually welded, due to the constant change in work angle (the angle between the electrode and work surface [53]). Although visual detection of the defect was not possible for this joint, using quantitative analysis techniques or reheating the joint in the in-field inspection to obtain a more consistent thermal pattern may be possible.

In-laboratory infrared trials

After acquiring a complete dataset of thermal images by active IR-TNDT, the images were analyzed using the native software provided by FLIR. Appendix C of this report provides a range of IR images from the samples at reference temperatures of approximately 50°C, 100°C, and 150°C.

Al weld joints with surface finish

Analysis from the Al weld samples in the pipe-to-plate and plate-to-plate surface-breaking drill hole conditions are shown in Figure 0-17 and Figure 0-18, respectively. Visual and IR images of the weld joints are demonstrated for uncoated and surface-finished samples. In the IR images, the temperature color scale is positioned on the right side of each image. The temperature read by pointing to the measuring spot (Sp1) on the top of the drilled hole location is approximately 100°C, shown in the upper left corner of their IR image.

Analogously to the temperature versus position analysis presented by Teyssieux et al. [54] based on IR images, a linear temperature profile was plotted along the weld line and across the drilled defect, shown in Figure 0-17(c) and Figure 0-18(c). In those plots, the x-axis refers to the position relative to the defect center, and the y-axis refers to the temperature reading. The IR images with the reference temperature of 100°C were used to build the profiles. The uncoated and surface finish samples for Al pipe-to-plate and plate-to-plate geometries show a temperature peak at the defect center.

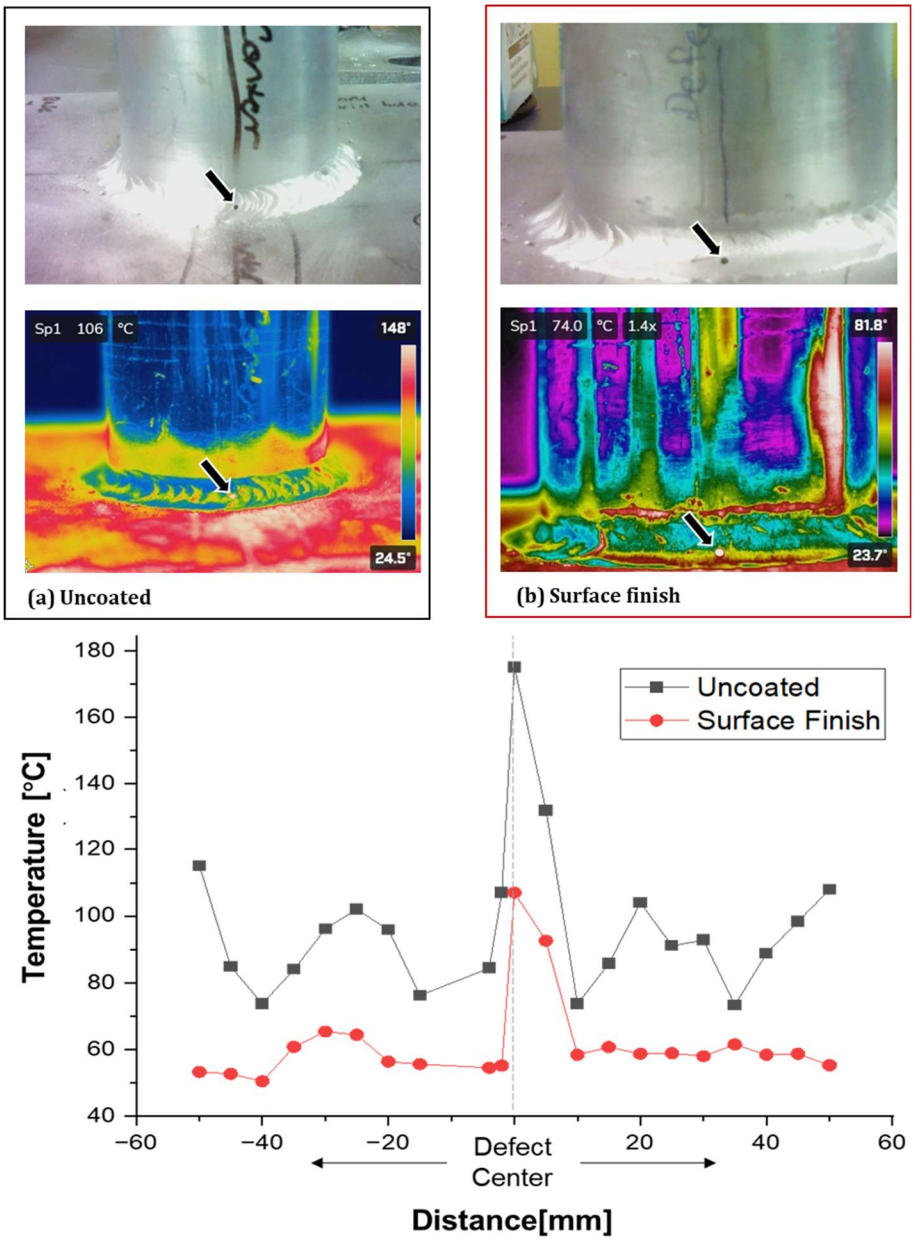

Figure 0-17 – Visual (top) and IR-TNDT (bottom) images at 100°C of the Al pipe-to-plate samples with the surface-breaking drill hole: (a) in the uncoated condition, (b) with the applied surface finish. The black arrows point to the location of the surface-breaking drill hole. (c) Analysis of the temperature profile along the weld line plotted from the IR images of the uncoated and with surface finish samples.

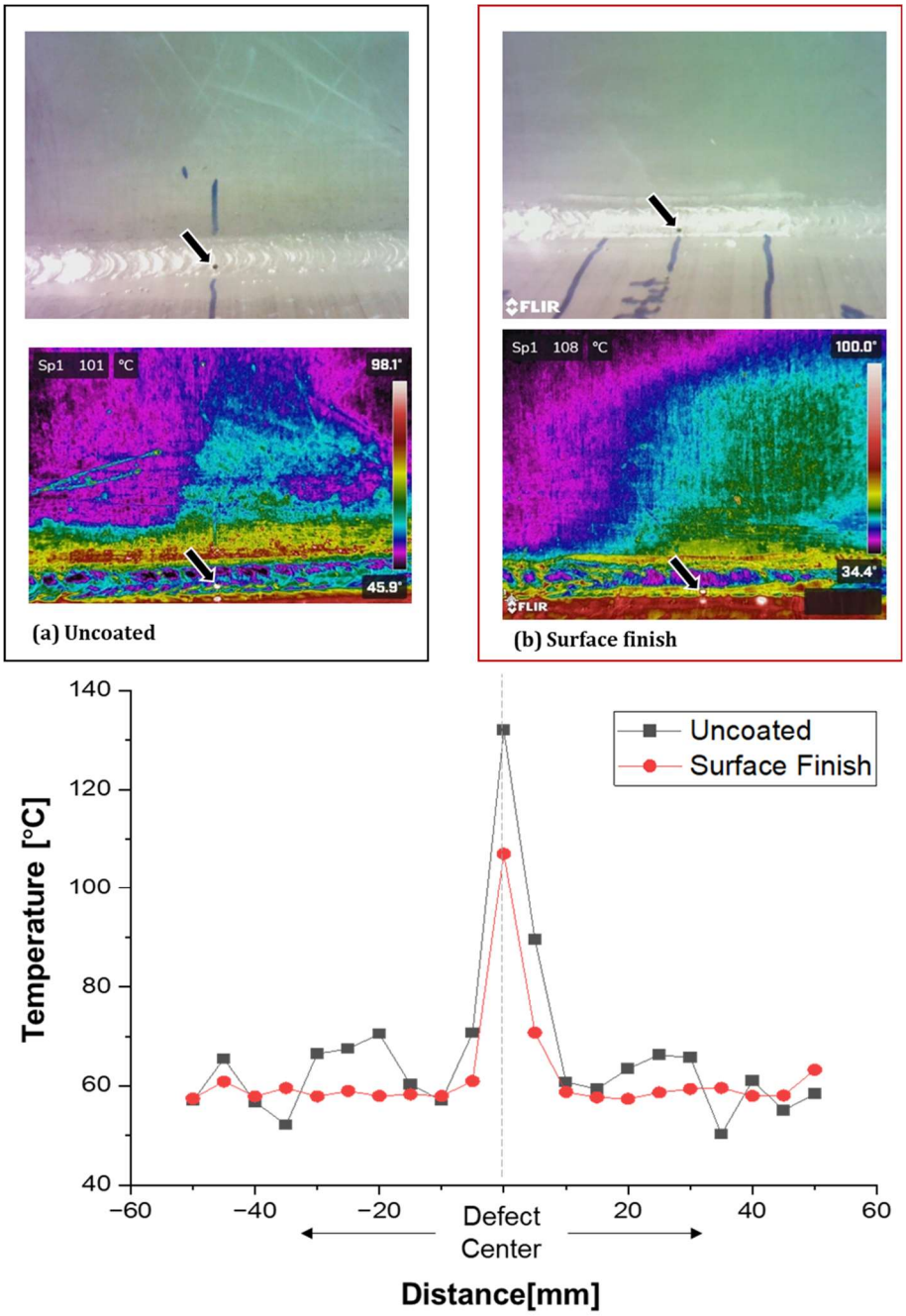

Figure 0-18 – Visual (top) and IR-TNDT (bottom) images at 100°C of the Al plate-to-plate samples with the surface-breaking drill hole: (a) the uncoated condition, (b) with the applied surface finish. The black arrows point to the location of the surface-breaking drill hole. (c) A linear temperature profile along the weld line plotted from the IR images of the uncoated and with surface finish samples.

Figure 0-19 displays visual and IR images of Al plate-to-plate weld joints with a subsurface pseudocrack. The machined subsurface pseudocrack could not be identified in the uncoated (a) or applied surface finished condition (b). The temperature color

scale is positioned on the right side of each IR image. The temperature was read by pointing the camera on the measuring spot, Sp1, at the beginning of the machined pseudocrack and is shown in the upper left corner of the image. Since no defect could be detected, no temperature profile was produced.

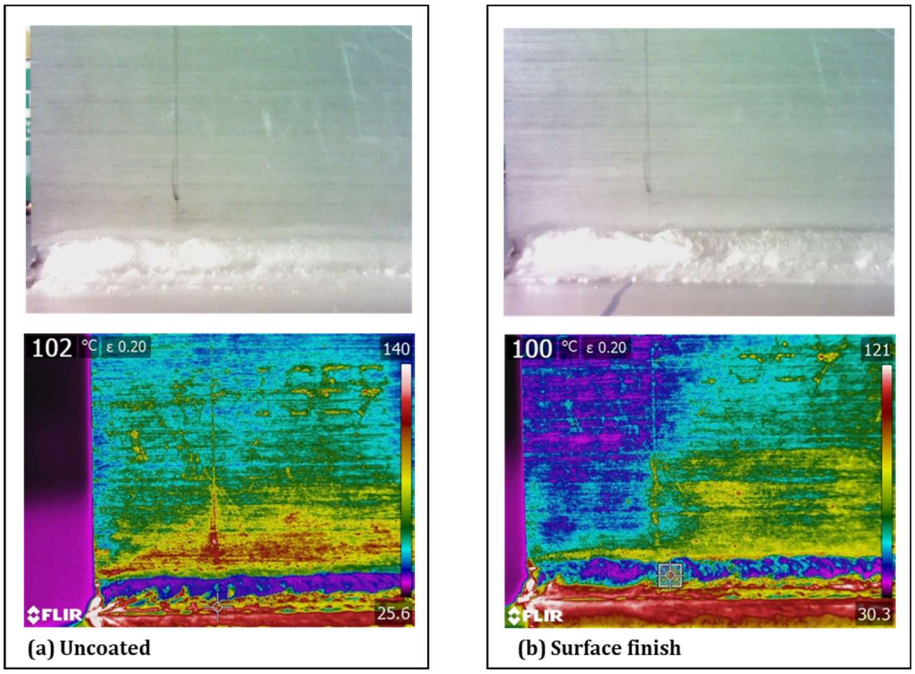

Figure 0-19 – Visual (top) and IR-TNDT (bottom) images at 100°C of the Al plate-to-plate samples with subsurface pseudocrack: (a) in the uncoated condition, (b) with the applied surface finish. No subsurface defect could be identified.

Steel weld joints with protective coatings

For the steel pipe-to-plate and plate-to-plate analysis presented in Figure 0-20 and Figure 0-21, the three sections compare the uncoated condition and samples with one and three layers of the Zinc-it® coating. The defect is visible in the IR images in all the samples with the surface-breaking drill hole, as highlighted by a black arrow. The temperature color scale appears on the right side of each IR image. The temperature on the upper left corner of each IR image refers to the reference temperature read by Sp1.

Analogously to the temperature *versus* position analysis presented by Teyssieux et al. [54] based on IR images, a linear temperature profile was plotted along the weld line and across the drilled defect, shown in Figure 0-20(d) and Figure 0-21(d). In those plots, the x-axis refers to the position at the defect center, and the y-axis refers to the temperature reading. The IR images with the reference temperature of 100°C were used to build the profiles.

A peak in temperature at the defect center can be perceived in the uncoated, one layer of Zinc-It®, and three layers of Zinc-It® samples for both steel pipe-to-plate and plate-to-plate geometries. However, there are two main observations:

1. In the uncoated condition, represented by the black line in Figure 0-20(d) and Figure 0-21(d), the temperature profile varies continuously across the sample, affecting the ability to identify the defect visually.
2. The defect center's temperature peak decreased considerably upon applying the third layer of Zinc-It® coating in the steel pipe-to-plate geometry, as shown in Figure 0-20(d).

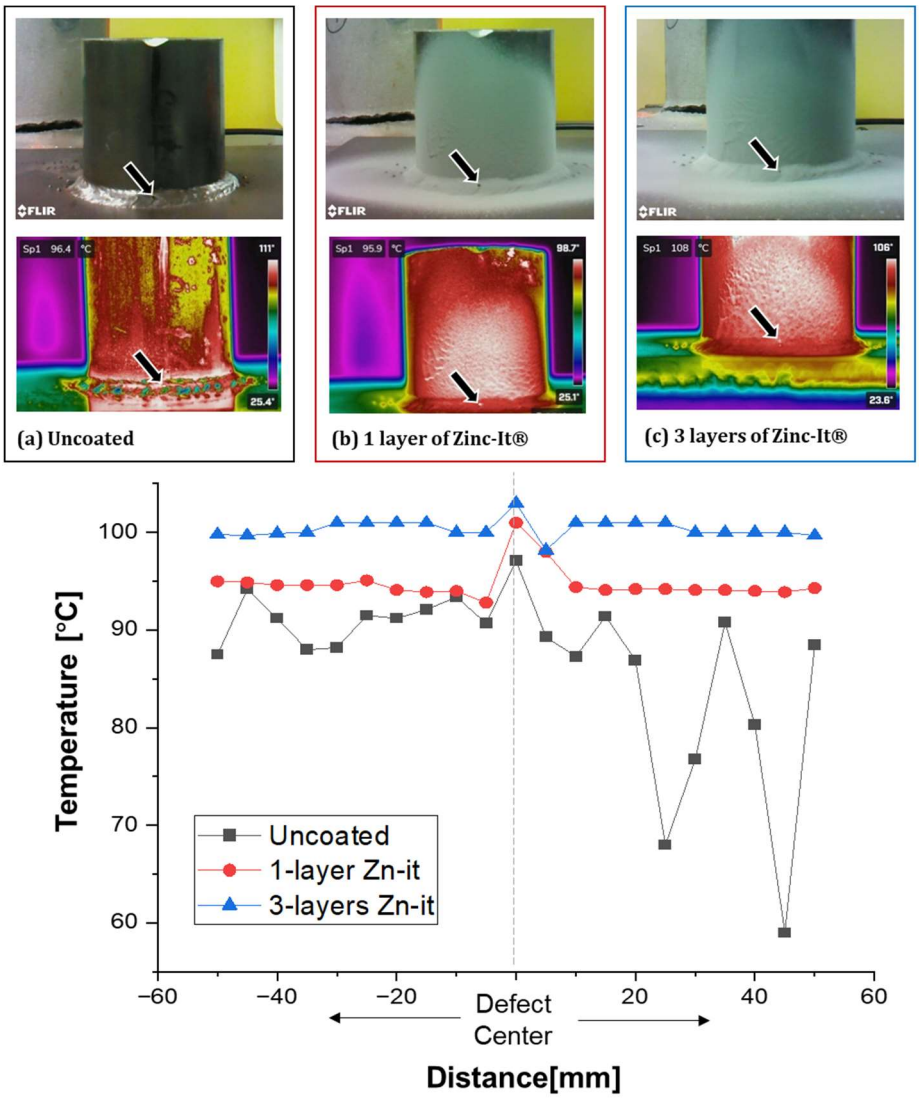

Figure 0-20 – Visual (top) and IR-TNDT (bottom) images at 100°C of the steel pipe-to-plate samples with the surface-breaking drill hole: (a) in the uncoated condition, (b) coated with 1 layer of Zinc-It® spray, (c) with 3 layers of Zinc-It® spray. Black arrows point to the location of the surface-breaking drill hole. (d) A linear temperature profile along the weld line plotted from the IR images of the uncoated and coated samples.

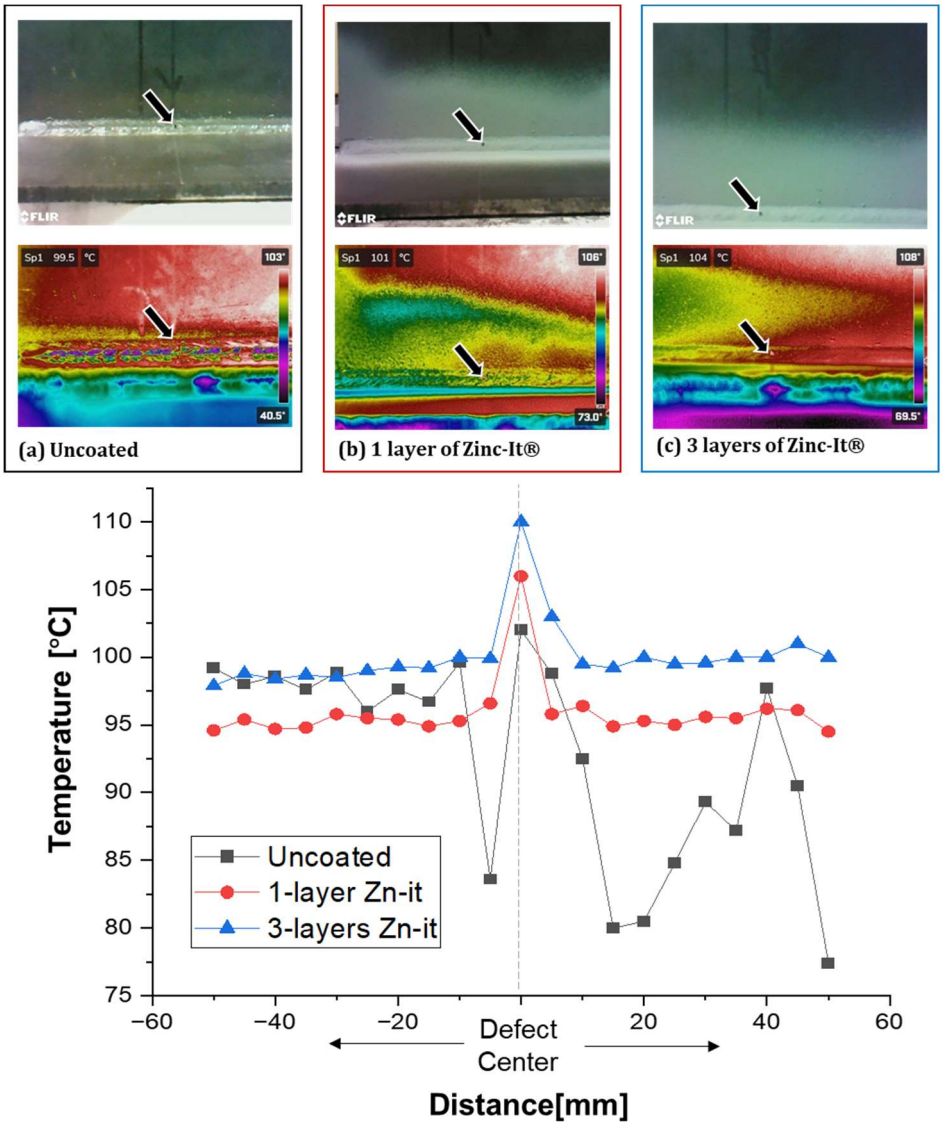

Figure 0-21 – Visual (top) and IR-TNDT (bottom) images at 100°C of the steel plate-to-plate samples with the surface-breaking drill hole: (a) in the uncoated condition, (b) coated with 1 layer of Zinc-It® spray, (c) with 3 layers of Zinc-It® spray. Black arrows point to the location of the surface-breaking drill hole. (d) A linear temperature profile along the weld line plotted from the IR images of the uncoated and coated samples.

The IR-TNDT in the steel welds coated with the epoxy-based coating is presented in Figure 0-22 and Figure 0-23. The temperature color scale appears on the right in the IR images. The temperature on the upper left corner of each image refers to the reference temperature read by Sp1. The defect is only visible in the IR images of the uncoated condition in Figure 0-22(a) and Figure 0-23(a) and is highlighted by a black arrow. Figure 0-22(b) and Figure 0-23(b) display the epoxy-based coating covering and obscuring surface-breaking drill holes.

A linear temperature profile was plotted along the weld line and is shown in Figure 0-22(c) and Figure 0-23(c), where the x-axis refers to the position in relation to the defect and the y-axis refers to the temperature reading. The IR images with the reference temperature of 100°C were used to build the profiles. In Figure 0-22(c) and Figure 0-23(c), the noisiness in the temperature profile of the uncoated samples can be noticed by the black line, however, a temperature peak can be observed at the defect center. Meanwhile, the red line shows the application of the epoxy-based coating, which covered and obscured the defect in the IR images.

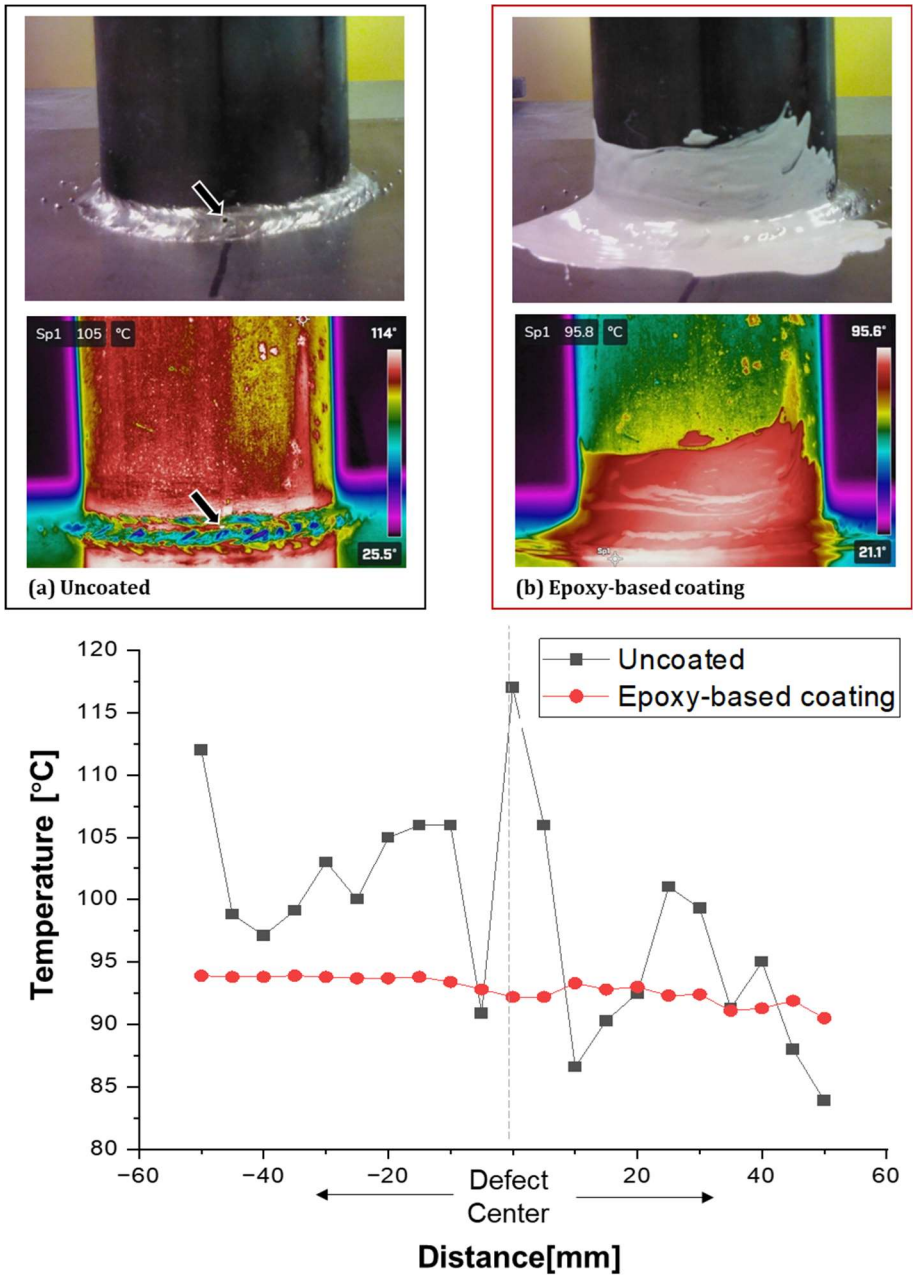

Figure 0-22 – Visual (top) and IR-TNDT (bottom) images at 100°C of the steel pipe-to-plate samples with the surface-breaking drill hole: (a) in the uncoated condition, (b) coated with the epoxy-based coating. The black arrows point to the location of the surface-breaking drill hole. In 'b', no defect can be detected. (c) A linear temperature profile along the weld line plotted from the IR images of the uncoated and coated samples.

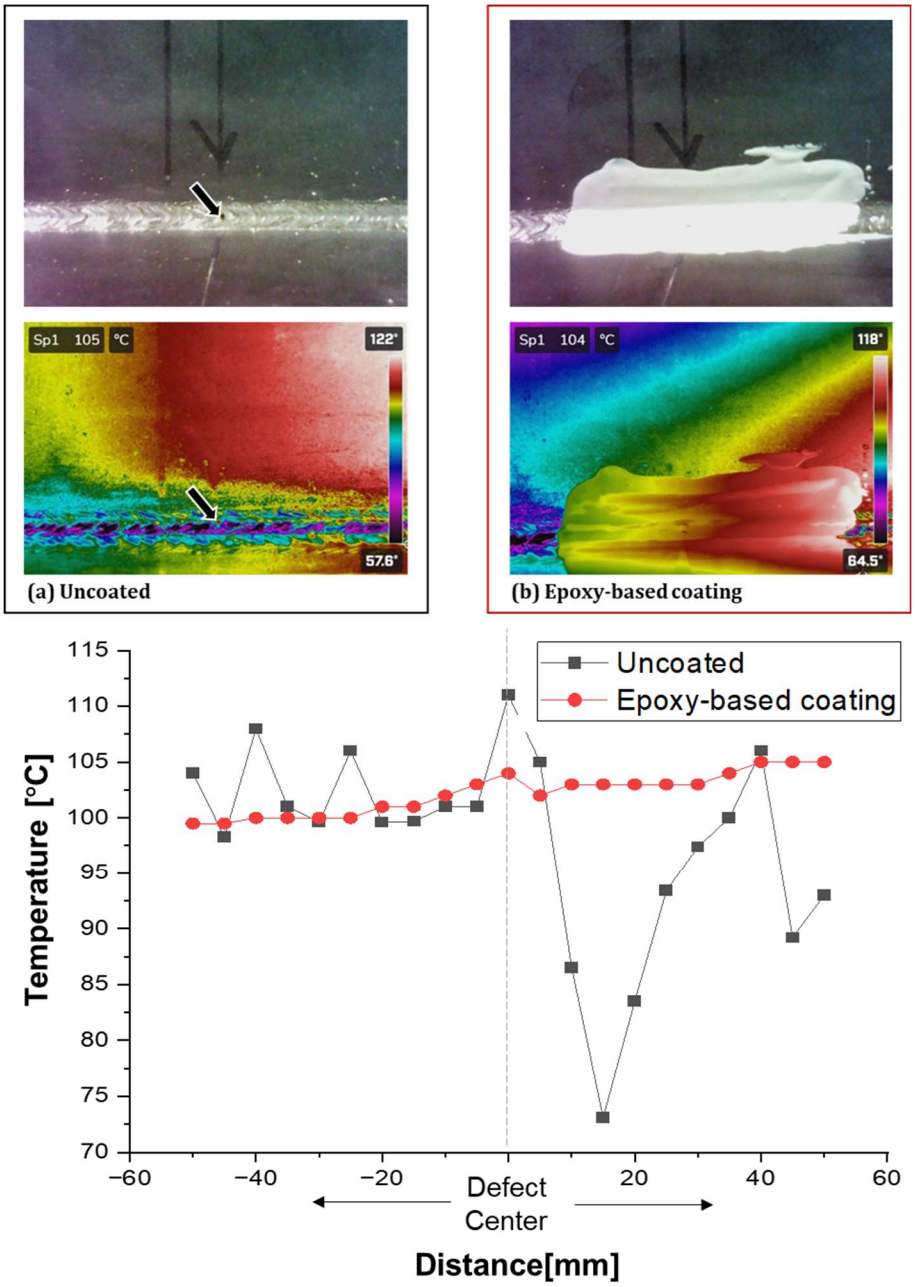

Figure 0-23 – Visual (top) and IR-TNDT (bottom) images at 100°C of the steel plate-to-plate samples with the surface-breaking drill hole: (a) in the uncoated condition, (b) coated with the epoxy-based coating. The black arrows point to the location of the surface-breaking drill hole. The defect was not observable after coating with the epoxy-based coating. (c) A linear temperature profile along the weld line plotted from the IR images of the uncoated and coated samples.

Summary and potential challenges in defect detectability upon coating

Identifying the drill hole in both the uncoated and surface finished conditions of Al weld joints was possible. Although the surface finish procedure generated a smoother IR image background, it did not significantly improve defect detectability. The defect was not detectable in the Al plate-to-plate samples with subsurface pseudocrack in the uncoated and surface-finished conditions. In the steel weld samples with a surface-breaking hole, an enhancement in the IR contrast between the background and defect was observed in the steel pipe-to-plate and steel plate-to-plate samples with one and three layers of Zinc-It® coating. The epoxy-based coating covered and obscured the defect, preventing it from being detected in the IR images.

In the literature [9], [27]–[29], noise and surface topography can considerably affect IR-TNDT images. Therefore, for the particular case of weld inspection by active IR thermography, it has been recommended that the inspector grind the weld surface or cover it with high-emissivity paint to provide a mono-contrast background for thermography [9], as illustrated in this report. According to Luong [28], matte spray paint raises the surface emissivity to a uniformly high level. This reduces surface reflections, improving the detectability of the onset of defects under fatigue loading.

For both base metals (steel and Al), the reliance on interpreting a defect is more strongly tied to the FLIR software temperature readings along each of the sample weld lines than relying on any individual image taken by the camera. Most of the temperature plots along the weld line showed a peak in temperature, allowing for the identification of the surface-breaking defect. Adding a surface finish in the Al samples created a smoother background, reducing noise related to topographical features in the defect surroundings.

Regarding the steel weld samples with the Zinc-It® protective coating, the application of the spray reduced the background noise in the IR images. However, additional layers of the Zinc-It® coating decreased the temperature peak in the defect center for the pipe-to-plate geometry. On the contrary, applying the epoxy-based coating obscured the presence of the surface-breaking defect, and no temperature peak was observed.

In-laboratory complimentary infrared trials

Comparing FLIR T620 and C5 IR images

Although the FLIR T620 showed a higher resolution than the FLIR C5 camera and increased quality images with better focus and contrast, this task aims to compare the performance of the FLIR C5 camera imaging a set of samples with the surface-breaking drill hole and subsurface pseudocrack. After acquiring a complete dataset of the weld joint thermal images, defect detection was visually performed. All infrared images were analyzed using the native software provided on the FLIR website [49] and, afterward, by Image J® for defect measurement. This section compares IR images taken with a FLIR C5 and T620 cameras for each of the selected weld joint samples in a chosen temperature range.

Al weld joint samples

The IR images from different Al weld joint samples with 120-grit surface finish are given in Figure 0-24, Figure 0-25, and Figure 0-26Figure 0-26, taken using the FLIR C5 and T620 cameras. These images show the temperature scale in °C, a white arrow pointing to the weld region where defects were visible, and labels giving information about the defect diameter in mm. Some examples of welding artifacts that produce a thermal signal are also pointed out in the IR images.

Despite being taken at a similar position and with the same parameter settings and environment calibration, it is possible to observe a very different temperature contrast acquired from FLIR C5 (Figure 0-24(a) to Figure 0-25(a)) and T620 (Figure 0-24(b) to Figure 0-25b)). Artifacts can be seen in the IR images obtained from both cameras. However, the decreased focus and contrast capabilities are evident in the FLIR C5 IR images compared to those acquired with the FLIR T620 camera.

Ultimately, surface-breaking drill hole defects are visible using the FLIR C5 or T620 cameras. In Figure 0-26(a-b), neither camera delivered an enhanced subsurface defect detectability.

(a)

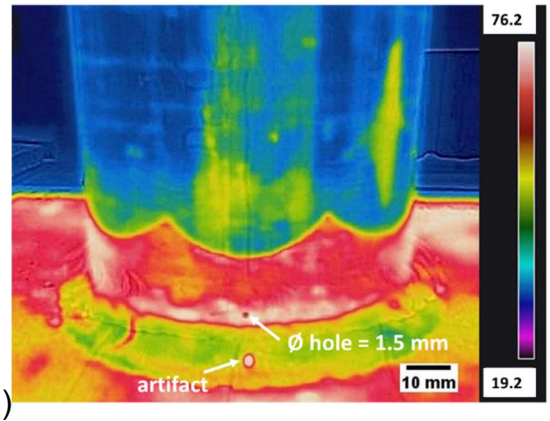

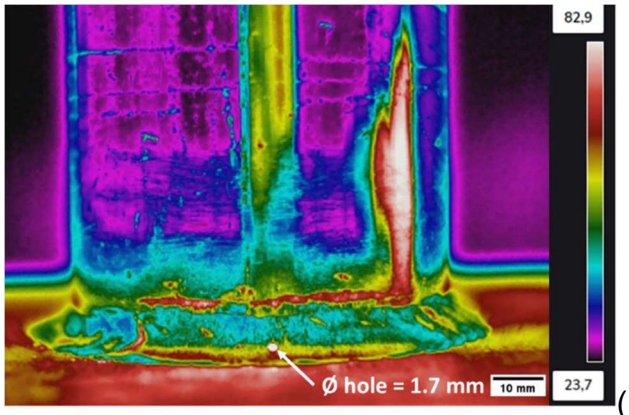

(b)

Figure 0-24 – Al pipe-to-plate weld joint sample, with surface-breaking drill hole and 120-grit surface finish: (a) IR image taken with FLIR C5 camera, (b) IR image taken with FLIR T620 camera. A white arrow points to the defect and a label informs the diameter of the hole. Some examples of artifacts are also labeled. A temperature scale in °C is provided on the right side of each IR image.

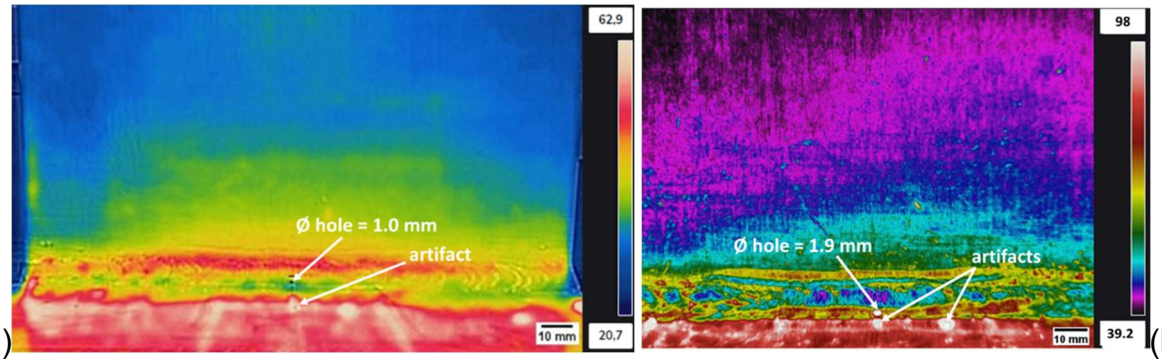

(a) (b)

Figure 0-25 – Al plate-to-plate weld joint sample, with surface-breaking drill hole and 120-grit surface finish, in (a) IR image taken with FLIR C5 camera and in (b) with FLIR T620 camera. A white arrow points to the defect and a label informs the diameter of the hole. Some examples of artifacts are also labeled. A temperature scale in °C is provided on the right side of each IR image.

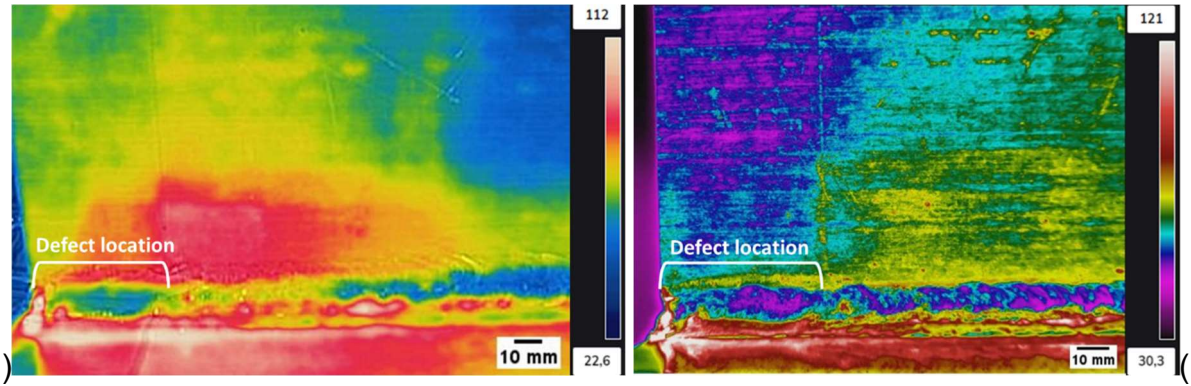

(a) (b)

Figure 0-26 – Al plate-to-plate weld joint sample, with subsurface pseudocrack and 120-grit surface finish, in (a) IR image taken with FLIR C5 camera and in (b) with FLIR T620 camera. The location of the machined cut pseudocrack is indicated. A temperature scale in °C is provided on the right side of each IR image.

Steel weld joint samples

The steel plate-to-plate weld joint samples with surface-breaking drill holes were imaged with the FLIR C5 camera in the uncoated and coated with AMERCOAT® 399 conditions, as shown in Figure 0-27(a) and

Figure 0-28(a), respectively. In Figure 0-27(b) and

Figure 0-28(b), the IR images taken with the FLIR T620 camera are presented for comparison. Figure 61(a) shows the steel pipe-to-plate weld joint sample with a surface-breaking drill hole imaged with C5 and T620 in the uncoated condition in Figure 0-29(b).

These images show the temperature scale in °C, a white arrow pointing to the weld region where defects were visible, and labels giving information about the hole diameter

in mm. Some examples of weld artifacts that produce a thermal signal are also pointed out in the IR images.

Again, a very different temperature contrast acquired from FLIR C5 compared to T620 is observed. Artifacts can be seen in the IR images obtained from both cameras. However, the decreased focus and contrast capabilities are evident in the FLIR C5 IR images compared to those acquired with the FLIR T620 camera.

Ultimately, surface-breaking drill hole defect is visible in Figure 0-27(a-b) and Figure 0-29(a-b) in both the plate-to-plate and pipe-to-plate uncoated conditions. In

Figure 0-28, both cameras delivered poor defect detectability after coating with AMERCOAT® 399. Thermal contrast at the drill hole position was barely observed. Despite that, an estimation of the hole dimension was made for comparison.

(a) 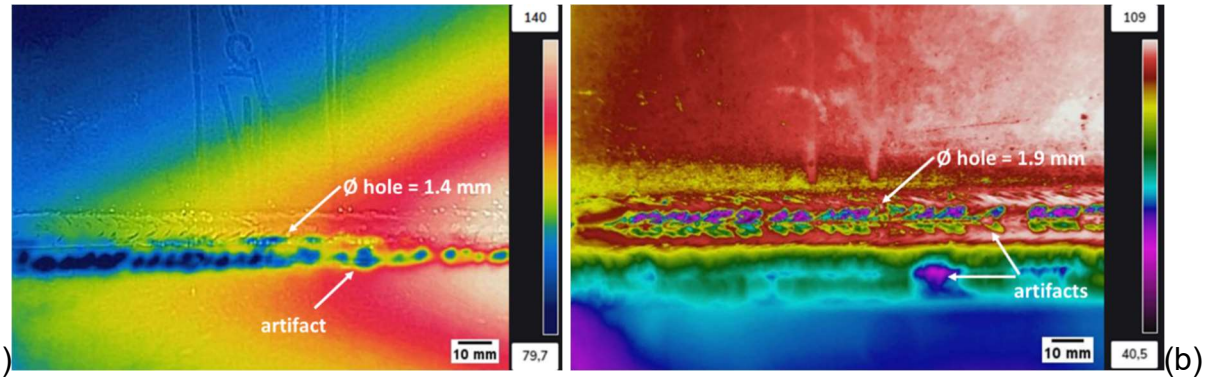

(b)

Figure 0-27 – Steel plate-to-plate weld joint sample, with surface-breaking drill hole without coating, in (a) IR image taken with FLIR C5 camera and in (b) with FLIR T620 camera. A white arrow points to the defect and a label informs the diameter of the hole. Some examples of artifacts are also labeled. A temperature scale in °C is provided on the right side of each IR image.

(a) 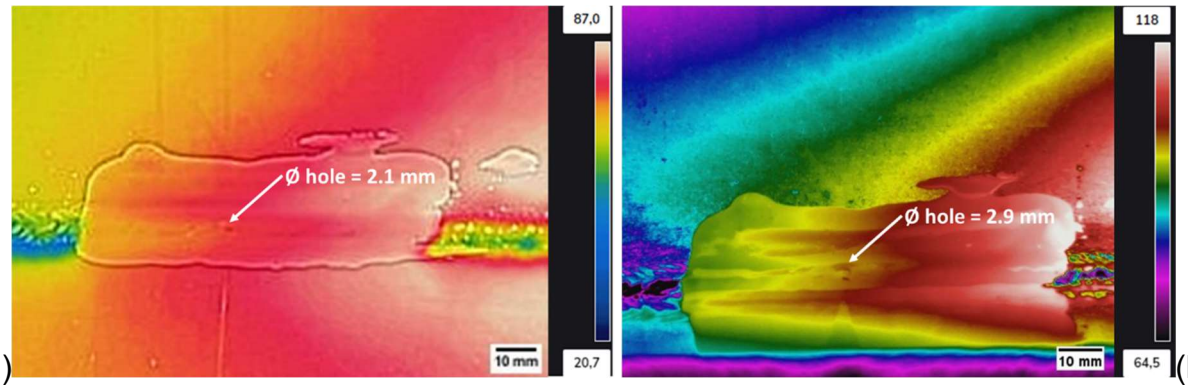

(b)

Figure 0-28 – Steel plate-to-plate weld joint sample, with surface-breaking drill hole coated with AMERCOAT® 399, in (a) IR image taken with FLIR C5 camera and in (b) with FLIR T620 camera. A white arrow points to the defect and a label informs the

diameter of the hole. A temperature scale in °C is provided on the right side of each IR image.

(a) 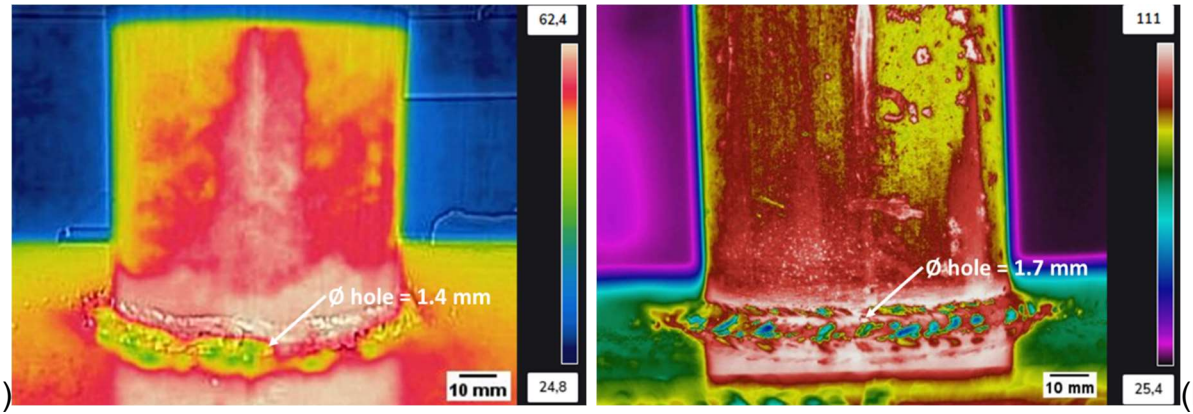

(b)

Figure 0-29 – Steel pipe-to-plate weld joint sample, with surface-breaking drill hole without coating, in (a) IR image taken with FLIR C5 camera and in (b) with FLIR T620 camera. A white arrow points to the defect and a label informs the diameter of the hole. A temperature scale in °C is provided on the right side of each IR image.

Potential challenges with FLIR C5 camera

The results illustrated that the FLIR C5 IR camera delivers lower quality thermograms with decreased focus and contrast. The specifications of the IR camera play an essential role in the IR-TNDT weld inspection. Another important IR camera capability that might positively impact the IR data acquisition is the image recording frequency, another drawback for the FLIR C5 use in-field. This capability allows for the post-processing evaluation of the cooling curves and temperature evolution with time, enabling the calculation of the cooling rate of a defective area compared to that of a non-defective region, which ultimately is known to improve subsurface defect detectability [7].

Defect quantification through destructive analysis

This subsection presents the optical micrographs taken from a cross-section of the weld joint samples. The defect quantification, i.e., measurement of the detected defect diameter, is shown to establish a basis for comparison with (1) the drill bit used to produce the surface-breaking defect and (2) the dimensions obtained from the IR thermal imaging.

The diameter of the drill hole measured from the optical images in Figure 0-30, Figure 0-31, and Figure 0-32 ranged from 1.8 to 2.0 mm. Values are in accordance with the actual drill bit diameter used to machine the defects (1/16” = 0.0625” = 1.6 mm), knowing that the drilling procedure results in a larger diameter than the nominal drill bit dimension. Nevertheless, the cross-section of the steel pipe-to-plate weld joint sample, shown in Figure 0-33, is misadjusted to the center of the drill hole, which led to an inaccurate measurement of the hole diameter. This value was then underestimated.

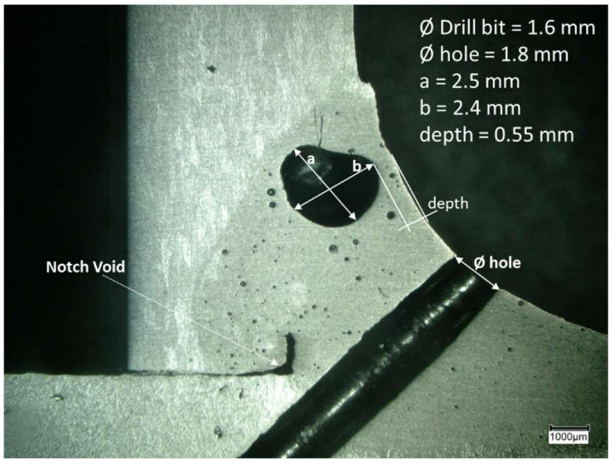

Figure 0-30 – Cross-section of the Al pipe-to-plate weld joint sample, showing the produced surface-breaking drill hole. Other subsurface weld defects could be observed from the cross-section and are pointed out in the optical image. Dimensions are labeled.

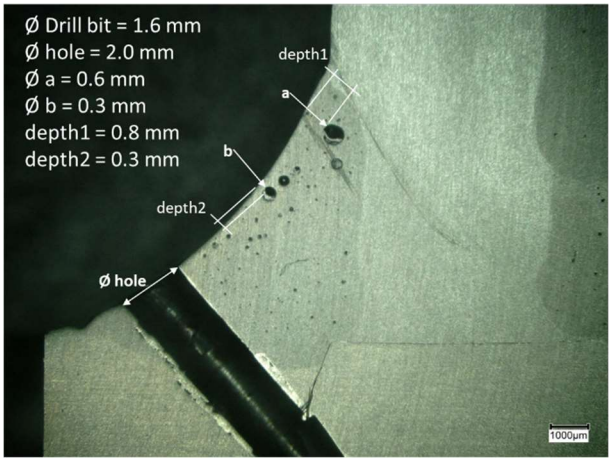

Figure 0-31 – Cross-section of the Al plate-to-plate weld joint sample, showing the produced surface-breaking drill hole. Other subsurface weld defects could be observed from the cross-section and are pointed out in the optical image. Dimensions are labeled.

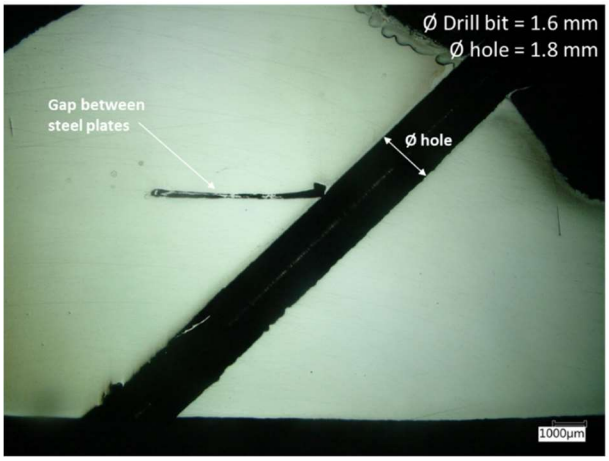

Figure 0-32 – Cross-section of the steel plate-to-plate weld joint sample, showing the produced surface-breaking drill hole. Other subsurface weld defects could be observed from the cross-section and are pointed out in the optical image. Dimensions are labeled.

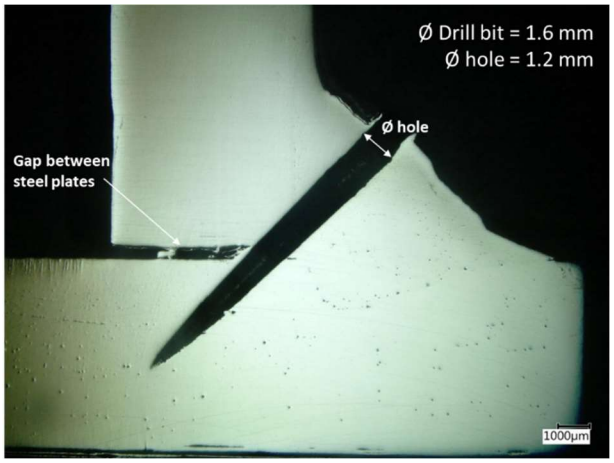

Figure 0-33 – Cross-section of the steel pipe-to-plate weld joint sample, showing the produced surface-breaking drill hole. Other subsurface weld defects could be observed from the cross-section and are pointed out in the optical image. Dimensions are labeled.

An important observation that can be addressed from the optical images presented in Figure 0-30, Figure 0-31, Figure 0-32, and Figure 0-33 is that most of the investigated weld joints showed other subsurface defects such as LOF, notch voids, porosity, etc., which were not evidenced in any of the IR images. For instance, the LOF observed in Figure 0-30 presents a significant cross-section area of almost 5 mm^2 at a depth of 0.55 mm. There was no indication of such a significant subsurface defect in the IR images shown in Figure 0-24. Besides the surface-breaking drill hole, no feature was observed in these IR images. Accordingly, it has been stated in the literature that single raw IR thermograms might be misinterpreted when used to investigate subsurface features

[26]. Additionally, to increase the reliability and enhance the accuracy of quantitative results, it is recommended to combine complementary non-destructive methods [26].

Analogously, the Al plate-to-plate weld joint sample cross-section, showing the machine cut subsurface pseudocrack, was also investigated through destructive analysis and optical microscopy, as shown in Figure 0-34. Other subsurface weld defects were observed from the cross-section and are pointed out in the optical image. None of these subsurface defects were identified in the corresponding IR image presented in Figure 0-26.

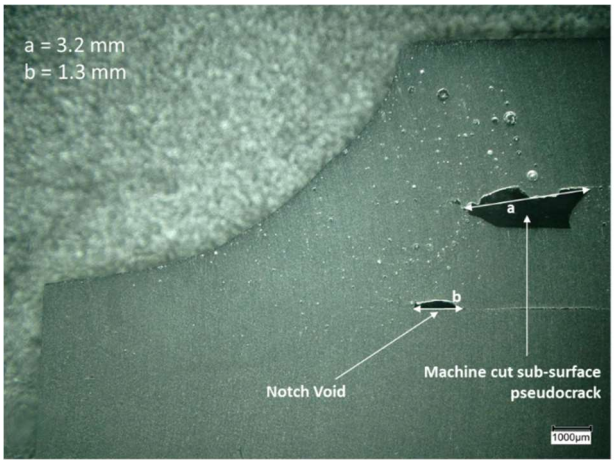

Figure 0-34 – Cross-section of the Al plate-to-plate weld joint sample, showing the machine cut subsurface pseudocrack. Other subsurface weld defects could be observed from the cross-section and are pointed out in the optical image. Dimensions are labeled.

Thereafter, we will compare the quantitative defect information (hole diameter) extracted from the IR-TNDT with the same information obtained from the destructive analysis (optical microscopy). To achieve that, the percentage deviation in dimensions (PDD) has been calculated according to Equation 1 [55]:

$$PDD = \frac{OM\ hole\ diameter - IR\ hole\ diameter}{OM\ hole\ diameter} x\ 100 \qquad \text{Equation 1}$$

The “OM hole diameter,” taken as the reference, was measured after destructive analysis from the cross-section optical micrographs (Figure 0-30, Figure 0-31, Figure 0-32, and Figure 0-33). The average OM and IR hole diameters and the calculated PDD values are listed in Table 0-1. For the “OM hole diameter,” the averages were calculated from 5 to 7 measurements at different positions along the hole section for each sample. Thus, the standard deviations represent the distribution and variability of the hole diameter along the hole length. The “IR hole diameter” was obtained from IR images for FLIR C5 and T620 cameras. Averages were calculated from 5 to 7 diameter

measurements from IR images taken at various time intervals for each sample. Thus, the standard deviations represent the distribution and variability of hole diameters measured from multiple IR images of one sample.

Table 0-1 – Summary of measurements from the optical micrographs (OM) and IR images using the FLIR T620 and FLIR C5 cameras. Defect data are represented as averages with standard deviation.

Sample	Ø hole optical image [mm]	Ø hole IR image C5 [mm]	PDD C5	Ø hole IR image T620 [mm]	PDD T620
Al pipe-to-plate (surface finish)	1.86 ± 0.10	1.51 ± 0.10	19%	1.74 ± 0.15	7%
Al plate-to-plate (surface finish)	2.05 ± 0.06	1.02 ± 0.17	50%	1.94 ± 0.15	5%
Steel plate-to-plate (uncoated)	1.81 ± 0.04	1.40 ± 0.24	23%	1.92 ± 0.24	-6%
Steel plate-to-plate (AMERCOAT®)	1.81 ± 0.04	2.11 ± 1.11	-16%	2.89 ± 0.96	-59%
Steel pipe-to-plate (uncoated)	1.16 ± 0.07	1.36 ± 0.32	-17%	1.75 ± 0.37	-51%

The Al pipe-to-plate, Al plate-to-plate (both with the surface finish), and uncoated steel plate-to-plate demonstrate a stronger correlation between the OM and IR images when using the FLIR T620 camera than the FLIR C5 camera. PDD values are larger for the IR images taken with the FLIR C5 camera, as would be expected due to its lower focus and contrast capabilities. Figure 0-35 illustrates how the defect edges present increased sharpness in the FLIR T620 IR image, ultimately leading to a more precise defect quantification.

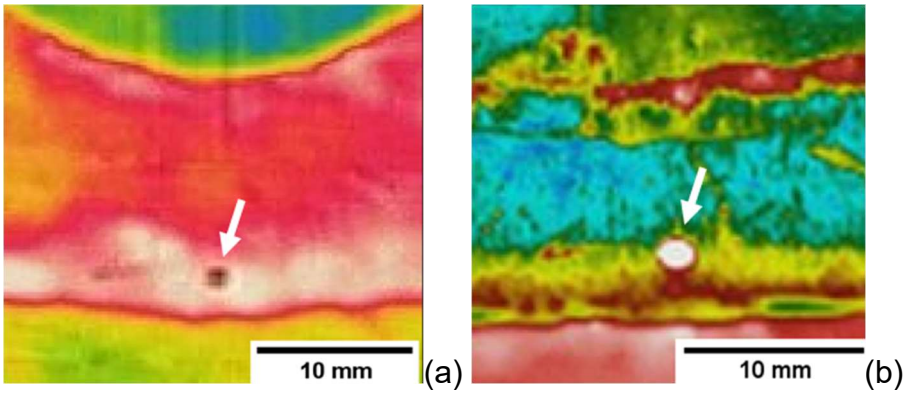

Figure 0-35 – Example of a zoomed in IR image (of the Al pipe-to-plate sample) taken with (a) C5 and (b) T620 cameras, evidencing increased sharpness of defect edges in the T620 image in 'b'.

For the steel plate-to-plate weld joint coated with AMERCOAT®, the epoxy-based coating hindered the defect detectability leading to poor thermal contrast in the IR images taken by both cameras, FLIR T620 and C5. This led to a high uncertainty (e.g., standard deviation) in the defect size due to topographical issues and imprecise edges, as shown in Figure 0-36.

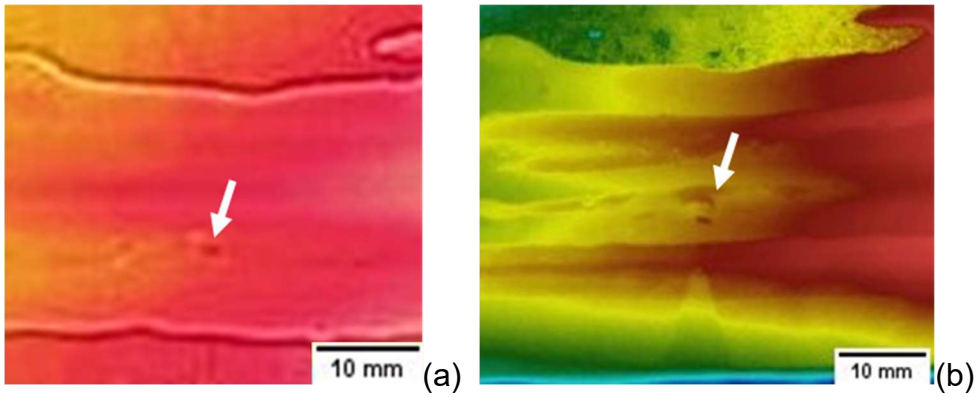

Figure 0-36 – Zoomed in IR image of the steel plate-to-plate sample coated with AMERCOAT®, taken with (a) C5 and (b) T620 cameras, evidencing very imprecise defect edges in both images.

The uncoated steel pipe-to-plate weld joint sample had lower OM values due to the cross-section's misalignment to the hole's midline, leading to hole diameters smaller than the drill bit. This increased the PDD value since the reference value from the optical image was underestimated. However, the defect diameters obtained from the IR images were consistent with the values obtained in the uncoated steel plate-to-plate weld joints. Thus, similar performance and results would be expected.

Potential challenges in defect quantification using IR-TNDT

The proposed IR active thermographic non-destructive technique has been verified using destructive tests and OM. To increase the applicability, acceptance, and reliability

of IR-TNDT in-field, several authors have worked on the comparison of the IR-TNDT results with other well-established destructive and non-destructive techniques [1], [23]–[25].

Additionally, single raw IR images are not the best method to quantify defects. Authors [26] claim that only qualitative analysis is possible using IR-TNDT. At the same time, the defect quantification (size and depth) cannot be determined without prior knowledge of the internal structure and application of image post-processing analysis techniques. Furthermore, there is a difference between the observation of in-lab produced defects and actual defects found in-field. It has also been argued that researchers use empirical information, which often lacks conclusive physical meaning to interpret IR images [26].

Chapter 5 Conclusions and Recommendations

Conclusions

To date, IR-TNDT has proven to be a promising NDT method to identify surface-breaking defects in weld joints. However, inspectors must be aware that the geometry of the weld, surface roughness, defect size, geometry, and position are all parameters that can potentially deliver false positive defect identification.

Based on the results presented, the following conclusions were drawn from this study:

- After acquiring a complete dataset of the weld joint thermal images by active IR-TNDT in different conditions, defect detection was visually performed. Surface-breaking defects were found to produce detectable indications using the IR-TNDT technology. No subsurface defects were detectable.
- IR camera FLIR T620 delivered better contrast, focus, and image acquisition capabilities than the FLIR C5. However, none of the cameras allowed subsurface defect detection.
- Using Zinc-It protective coating on steel weld joint surfaces reduced the background noise, enhancing thermal contrast in the IR images taken with FLIR T620. Thus, applying high emissivity coatings or paints onto the weld surface appears promising.
- For steel and Al weld joints, a consistent and reliable interpretation of the surface-breaking type of defect was aided by an analysis of the linear temperature data plotted along the weld line. Observing defects in any individual IR image was not straightforward, demonstrating that further data interpretation should be required for proper defect identification.

Recommendations

According to AASHTO/AWS D1.5 and D1.6, visual inspection is mandatory, and recommendations are made regarding tolerable defect types, sizes, and positions. In most cases, if a defect is found during visual inspection in any test length of a weld, the remainder of the weld shall be tested by conventional radiography or ultrasonic test (UT).

Based on the findings from this study, the following recommendations are made:

Weld joint preparation:

- Whenever possible, it is recommended that, previous to inspection, the steel weld joint is covered with a single layer of high-emissivity, low-viscosity protective coating (e.g. Zinc-It® spray).
- For Al weld joints, the surface finish did not result in improved defect identification. Therefore, unless it is feasible to apply a very smooth surface polishing in the field before each inspection to homogenize the IR image background, a directional textured coarse-to-medium satin surface finish [56] is not recommended.

Camera setup and calibration:

- The FLIR T620 camera is preferred over the FLIR C5, whenever possible.
- The IR camera needs to be calibrated according to the environment by inputting the following settings: atmospheric temperature (°C), relative humidity (%), and reflected temperature (°C). These settings should be determined using a thermometer and hydrometer in the same inspection area.
- Materials emissivity (ε) should also be input into the camera settings before imaging. Results from this investigation determined materials' emissivity as: 0.45-0.79 for steel and 0.20 for Al weld joints.
- Using a tripod and setting an IR image acquisition every 30 sec is recommended.
- The IR camera should be placed 10 in away from the object of interest, and the best possible focus must be achieved before acquiring infrared data.

Sample heating:

- In-field inspection via active IR-TNDT, the sample should be heated to 100°C before imaging using a heat gun.
- Select a spot to monitor the temperature measurement within the region of interest and wait until it reaches 100°C. Wait 30 sec for the temperature to stabilize, then acquire the IR image.
- Acquisition should remain until the same spot reaches 50°C.

IR image analysis:

- A trained and experienced inspector should analyze the IR images and search for possible abnormalities and flaws.
- A historical comparison between IR images taken during an inspection of the same area of interest at similar temperature ranges should be established. Inspectors should build a timeline record of the NDT analyses to help the accurate identification of a surface defect onset.

General:

- Since IR-TNDT delivered only surface-breaking defect identification, further investigation is recommended to use IR-TNDT combined with other conventional NDT for surface-breaking defects analysis, such as dye penetrant or magnetic particle testing.
- Further investigation of different types of high emissivity paints/coatings is recommended, based on the promising results obtained after applying a single Zin-It layer coating on steel welds.
- It is also recommended to develop built-in data processing techniques to improve the signal/noise ratio in the crack detection process by IR-TNDT.
- Using active IR-TNDT as a sole substitution for any other conventional NDT is not recommended. However, IR-TNDT can be used to visually inspect either in-

shop, after the welding procedure during cool down, or in-field, after an external heat source is applied to post-welding periodic inspection.

References

[1] A. S. Madhvacharyula, A. V. S. Pavan, S. Gorthi, S. Chitral, N. Venkaiah, and D. V. Kiran, “In situ detection of welding defects: a review,” *Welding in the World*, vol. 66, no. 4, pp. 611–628, 2022, doi: 10.1007/s40194-021-01229-6.

[2] S. Kumar and D. Mahto, “Recent Trends in Industrial and other Engineering Applications of Non-Destructive Testing: A Review,” *International Journal of Scientific & Engineering Research*, vol. 4, no. 9, pp. 183-195, 2013.

[3] D. Balageas *et al.*, “Thermal (IR) and Other NDT Techniques for Improved Material Inspection,” *Journal of Nondestructive Evaluation*, vol. 35, no. 1, pp. 1–17, 2016, doi: 10.1007/s10921-015-0331-7.

[4] G. R. Edwards, “Inspection of Welded Joints,” *ASM International*, vol. 6, pp. 1081–1088, 1993.

[5] X. Maldague, *Theory and Practice of Infrared Technology for Nondestructive Testing*. Wiley & Sons, Inc., 2001.

[6] V. Vavilov, “Thermal NDT: Historical milestones, state-of-the-art and trends,” *Quantitative InfraRed Thermography Journal*, vol. 11, no. 1, pp. 66–83, 2014.

[7] M. Rodríguez-Martin, S. Lagüela, D. González-Aguilera, and P. Arias, “Cooling analysis of welded materials for crack detection using infrared thermography,” *Infrared Physics and Technology*, vol. 67, pp. 547–554, 2014, doi: 10.1016/j.infrared.2014.09.025.

[8] M. Manuel and G. Washer, “Research Progress Report Use of Infrared Thermography for the Inspection of Welds in the Shop and Field,” no. December, 2017.

[9] S. Dorafshan, M. Maguire, and W. Collins, “Infrared thermography for weld inspection: Feasibility and application,” *Infrastructures*, vol. 3, no. 4, 2018, doi: 10.3390/infrastructures3040045.

[10] C. L. Tsai, U. S. Design, and U. S. Design, “Heat Flow in Fusion Welding,” in *Welding Fundamentals and Processes*, ASM International, 2011, pp. 55–66. doi: 10.31399/asm.hb.v06a.a0005588.

[11] D. L. Olson, T. A. Siewert, S. Liu, and G. R. Edwards, “Overview of Weld Discontinuities,” *ASM International*, vol. 6, pp. 1073–1080, 1993.

[12] S. C. Chapple, P. I. Temple, D. A. Senatore, K. Barras, and R. McCoy, “Weld Quality,” in *Welding Handbook, volume 1*, American Welding Society (AWS), 2001, pp. 533–577.

[13] W. D. Callister and D. G. Rethwisch, *Materials Science and Engineering*, 8th ed. John Wiley & Sons, Inc., 2010.

[14] F. E. Alzofon, L. E. Florant, R. K. Ronald, M. J. Vann, and J. E. Fitzgerald, “IR Nondestructive Testing of Glass Filament-Wound Rocket Motor Cases,” in *Proceedings of the Fourth Pacific Area National Meeting of ASTM*, Los Angeles, Calif., 1962.

[15] F. E. Alzofon, L. E. Florant, R. H. Anderson, and L. K. Loomer, “IR Nondestructive Testing of Glass Filament-Wound Rocket Motors,” in *Proceedings of the Fourth Annual Symposium on Nondestructive Testing of Aircraft and Missile Components*, San Antonio, Texas, 1963, pp. 153–170.

[16] F. E. Alzofon, “Factors Influencing the Detection of Flaws in Glass Filament-Wound Rocket Motor Cases by IR Scanning,” in *Second ICRPG Symposium on the Nondestructive Inspection of Solid Propellant Rocket Motors*, 1963.

[17] L. E. Florant, “Testing Using Infrared,” *ISA Journal*, 1964.

[18] M. Walker, J. Roschen, and E. Schlegel, “An IR Scanning Technique for the Determination of Temperature Profiles in Microcircuits,” *IEEE Transactions on Electron Devices*, pp. 263–267, 1963.

[19] B. B. Lahiri *et al.*, “Defect detection in weld joints by infrared thermography,” *International Conference on NDE in Steel and allied Industries, NDESAI*, pp. 191–197, 2011.

[20] I. Kryukov, M. Hartmann, S. Bohm, M. Mund, K. Dilger, and F. Fischer, “Defect Detection in Friction Stir Welding by Online Infrared Thermography,” *Journal of Welding and Joining*, vol. 32, no. 5, pp. 50–57, 2014.

[21] A. Garcia De La Yedra, A. Echeverria, A. Beizama, R. Fuente, and E. Fernández, “Infrared Thermography as an Alternative to Traditional Weld Inspection Methods thanks to Signal Processing Techniques,” *11th European Conference on Non-Destructive Testing*, no. Ecndt, 2014.

[22] A. Kylili, P. A. Fokaides, P. Christou, and S. A. Kalogirou, “Infrared thermography (IRT) applications for building diagnostics: A review,” *Applied Energy*, vol. 134, pp. 531–549, 2014, doi: 10.1016/j.apenergy.2014.08.005.

[23] C. Meola, G. M. Carlomagno, A. Squillace, and G. Giorleo, “The use of infrared thermography for nondestructive evaluation of joints,” *Infrared Physics and Technology*, vol. 46, no. 1-2 SPEC. ISS., pp. 93–99, 2004, doi: 10.1016/j.infrared.2004.03.013.

[24] C. Meola, R. Di Maio, N. Roberti, and G. M. Carlomagno, “Application of infrared thermography and geophysical methods for defect detection in architectural structures,” *Engineering Failure Analysis*, vol. 12, no. 6 SPEC. ISS., pp. 875–892, 2005, doi: 10.1016/j.engfailanal.2004.12.030.

[25] F. Khan and I. Bartoli, “Detection of delamination in concrete slabs combining infrared thermography and impact echo techniques: a comparative experimental study,” *Structural Health Monitoring and Inspection of Advanced Materials, Aerospace, and*

Civil Infrastructure 2015, vol. 9437, no. April 2015, p. 94370I, 2015, doi: 10.1117/12.2084096.

[26] B. Milovanović and I. B. Pečur, “Review of active IR thermography for detection and characterization of defects in reinforced concrete,” *Journal of Imaging*, vol. 2, no. 2, pp. 1–27, 2016, doi: 10.3390/jimaging2020011.

[27] V. Jacintha, S. Karthikeyan, and P. Sivaprakasam, “Surface Flaw Detection of Plug Valve Material Using Infrared Thermography and Weighted Local Variation Pixel-Based Fuzzy Clustering Technique,” *Advances in Materials Science and Engineering*, vol. 2022, 2022, doi: 10.1155/2022/7919532.

[28] M. P. Luong, “Fatigue limit evaluation of metals using an infrared thermographic technique,” *Mechanics of Materials*, vol. 28, no. 1–4, pp. 155–163, 1998, doi: 10.1016/S0167-6636(97)00047-1.

[29] F. Ciampa, P. Mahmoodi, F. Pinto, and M. Meo, “Recent advances in active infrared thermography for non-destructive testing of aerospace components,” *Sensors (Switzerland)*, vol. 18, no. 2, 2018, doi: 10.3390/s18020609.

[30] S. Henke, D. Karstädt, K. Möllmann, F. Pinno, and M. Vollmer, “Identification and suppression of thermal reflections in infrared thermal imaging,” *InfraMation*, vol. 5, pp. 1–11, 2004.

[31] J. Yang, W. Wang, G. Lin, Q. Li, Y. Sun, and Y. Sun, “Infrared Thermal Imaging-Based Crack Detection Using Deep Learning,” *IEEE Access*, vol. 7, no. Mm, pp. 182060–182077, 2019, doi: 10.1109/ACCESS.2019.2958264.

[32] R. Shrestha, S. Sfarra, S. Ridolfi, G. Gargiulo, and W. Kim, “A numerical–thermal–thermographic NDT evaluation of an ancient marquetry integrated with X-ray and XRF surveys,” *Journal of Thermal Analysis and Calorimetry*, vol. 147, no. 3, pp. 2265–2279, 2022, doi: 10.1007/s10973-021-10571-2.

[33] C. Ibarra-Castanedo, D. González, M. Klein, M. Pilla, S. Vallerand, and X. Maldague, “Infrared image processing and data analysis,” *Infrared Physics and Technology*, vol. 46, no. 1-2 SPEC. ISS., pp. 75–83, 2004, doi: 10.1016/j.infrared.2004.03.011.

[34] D. L. Balageas, J. M. Roche, F. H. Leroy, W. M. Liu, and A. M. Gorbach, “The thermographic signal reconstruction method: A powerful tool for the enhancement of transient thermographic images,” *Biocybernetics and Biomedical Engineering*, vol. 35, no. 1, pp. 1–9, 2015, doi: 10.1016/j.bbe.2014.07.002.

[35] P. Bagavac, L. Krstulovic-Opara, and Ž. Domazet, “Infrared thermography of steel structure by FFT,” *Materials Today: Proceedings*, vol. 12, pp. 298–303, 2019, doi: 10.1016/j.matpr.2019.03.127.

[36] F. D. of Transportation, “Standard Plans for Road Construction- FY 2020-21,” 2019. https://www.fdot.gov/design/standardplans/current/default.shtm

[37] American Welding Society, *AWS D1.1./D1.1M:2015 Structural Welding Code-Steel*, 23rd ed. 2015.

[38] American Welding Society, *AWS D1.2./D1.2.M:2014 Structural Welding Code-Aluminum*. 2014.

[39] G. F. Vander Voort, *ASM Handbook, Volume 9: Metallography And Microstructures*. ASM International, 2004.

[40] American Welding Society, *AWS D1.1./D1.1M:2015 Structural Welding Code-Steel*, 23rd ed. 2015.

[41] The Society for Protective Coatings (SSPC) Standards, “SSPC: The Society for Protective Coatings Surface Preparation Specification No. 1 Solvent Cleaning,” *Policy*, no. 8, pp. 70–71, 2003.

[42] “Zinc-It Instant Cold Galvanize™ Technical Data Sheet”.

[43] “Product data sheet Amercoat 399.”

[44] M. E. Finn, “Mechanical Finishing of Aluminum,” *ASM International*, vol. 2A, 2018.

[45] FLIR, “FOV Calculator,” 2019.

[46] FLIR, “Spot Size Ratio- Technical Note.” 2018.

[47] FLIR, “Handheld Thermal Cameras,” 2020.

[48] FLIR, “User’s manual FLIR 600 series.” 2009.

[49] FLIR, “https://ignite.flir.com/library/.” https://ignite.flir.com/library/ (accessed Jan. 20, 2023).

[50] Y. Yu, L. Lan, F. Ding, and L. Wang, “Mechanical properties of hot-rolled and cold-formed steels after exposure to elevated temperature: A review,” *Construction and Building Materials*, vol. 213, pp. 360–376, 2019.

[51] J. R. Davis, “Service Characteristics of Carbon and Alloy Steels,” in *Metals Handbook Desk Edition*, 2nd ed.ASM International, 1998, pp. 274–300.

[52] ASM International, *Metals Handbook*, 2nd ed. 1998.

[53] D. B. Holliday, “Gas-Metal Arc Welding,” *Welding, Brazing, and Soldering*, vol. 6, pp. 180–185, 2018, doi: 10.31399/asm.hb.v06.a0001354.

[54] D. Teyssieux, L. Thiery, and B. Cretin, “Near-infrared thermography using a charge-coupled device camera: Application to microsystems,” *Review of Scientific Instruments*, vol. 78, no. 3, 2007, doi: 10.1063/1.2714040.

[55] J. S. Chohan, R. Singh, K. S. Boparai, R. Penna, and F. Fraternali, “Dimensional accuracy analysis of coupled fused deposition modeling and vapour smoothing operations for biomedical applications,” *Composites Part B: Engineering*, vol. 117, pp. 138–149, 2017, doi: 10.1016/j.compositesb.2017.02.045.

[56] F. D. of Transportation, “Standard Plans for Road Construction- FY 2021-22,” 2022.

[57] FLIR, “FLIR T620 25 Datasheets,” 2017.

[58] FLIR, “FLIR C5 Datasheets,” 2020.

Appendix A – Welding Procedure Specifications

The welding procedure specifications (WPSs) for the steel and Al welds investigated in the present work with additional details on the welding procedures performed and can be found in this Appendix.

STATE OF FLORIDA DEPARTMENT OF TRANSPORTATION

WELDING PROCEDURE SPECIFICATION (WPS)

AWS D1.1 WPS
Form # 675-070-05
April 2019

(D1.1) PREQUALIFIED ☑ QUALIFIED BY TESTING ☐

Contractor/Organization: University of Florida	Identification #: UF-GMAW-STEEL-01
Welding Process(es): GMAW	Revision: Date: 06/05/2020 By: Brittani Maskley
Supporting: PQR No.(s): Prequalified FWST No.(s):	Authorized By: Date:
JOINT DESIGN USED	Type: Manual ☐ Mechanized ☐ Semiautomatic ☑ Automatic ☐
Groove Type: Fillet: ☑	
Backing: Yes ☐ No ☑	**ELECTRICAL CHARACTERISTICS**
Backing Mat'l:	Transfer Mode (GMAW): Short-Circuiting ☐
Root Opening: NA Root Face Dimension:	Globular ☐ Spray ☑
Groove Angle: Radius (J-U):	Current: AC ☐ DCEP ☑ DCEN ☐ Pulsed ☐
Backgouging: Yes ☐ No ☑ Method:	Power Source: CC ☐ CV ☑
Root Treatment: Stainless steel wire brush	Other:
POSITION	Tungsten Electrode (GTAW):
Position of Groove: Fillet: 2F	Size: Type:
Vertical Progression: Up ☐ Down ☐	**TECHNIQUE**
BASE METALS	Stringer or Weave Bead: Stringer
Material Spec: ASTM A36	Multi-Pass or Single Pass (per side): Multi-pass side 1, single-pass side 2
Type or Grade:	Number of Electrodes:
Thickness: Groove: Fillet: 1/4"	Electrode Spacing: Longitudinal:
Diameter (Pipe):	Lateral: Angle:
FILLER METALS	Electrical Stick Out: 1/2"
AWS Specification: AWS-A5.18	Peening: Interpass Cleaning: Stainless steel wire brush
AWS Classification: ER70S-6	**PREHEAT AND INTERPASS TEMPERATURE CHART**
Mfg. Trade Name: WA. Alloy. Co.	
SHIELDING	
Flux:	
Electrode Flux Class:	
Gas: Argon/Carbon dioxide Composition: 75%A, 25%CO2	
Flow Rate: 40 CFH Gas Cup Size:	
POSTWELD HEAT TREATMENT	
Temp: NA Time:	

Base Metal Thickness Range	Min Preheat & Interpass (°F)	Max Preheat & Interpass (°F)
1/8"-3/4"	32	NA

WELDING PROCESS

Pass or Weld Layer(s)	Filler Metal Diam.	Current	Volts	Travel Speed IPM
3/16"<=X<=3/8"	0.035"	160-300A	23-26V	11-22

Joint Designation: Fillet

UPLOAD JOINT DETAILS

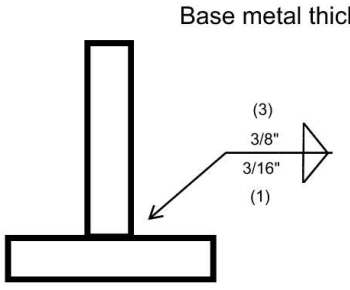

FABRICATOR'S CWI DIGITAL SIGNATURE

AWS CWI #: CWI Exp. Date:

UPLOAD FDOT CONSULTANT STAMP

Date:

Notes:

UPLOAD FDOT STAMP

Tim McCullough

Digitally signed by: Tim McCullough
DN: CN = Tim McCullough email = timothy.mccullough@dot.state.fl.us C = US OU = FDOT State Materials
Date: 2020.07.28 16:38:26 -04'00'

Date:

Comments:

E-Mail the completed digital form to SM-StructuresCI@dot.state.fl.us, FDOT State Materials Office

FDOT Note: Qualified for Flat (1F) and Horizontal (2F) plate use only. (Table 4.10)
Single Pass fillet weld are qualified to the max. size shown in the Joint Designation
WPS is invalid if the essential variables listed in Table 3.6 and Table 3.7 are not met;

STATE OF FLORIDA DEPARTMENT OF TRANSPORTATION

WELDING PROCEDURE SPECIFICATION (WPS)

AWS D1.1 WPS
Form # 675-070-05
April 2019

(D1.1) PREQUALIFIED ☐ QUALIFIED BY TESTING ☑

Contractor/Organization: University of Florida	Identification #: UF-GMAW-STEEL-02
Welding Process(es): GMAW	Revision: Date: 06/05/2020 By: Brittani Maskley
Supporting: PQR No.(s): 2x Macroetches FWST No.(s):	Authorized By: Date:
JOINT DESIGN USED	Type: Manual ☐ Mechanized ☐ Semiautomatic ☑ Automatic ☐
Groove Type: Fillet: ☑	
Backing: Yes ☐ No ☑	**ELECTRICAL CHARACTERISTICS**
Backing Mat'l:	Transfer Mode (GMAW): Short-Circuiting ☐
Root Opening: NA Root Face Dimension:	Globular ☐ Spray ☑
Groove Angle: Radius (J-U):	Current: AC ☐ DCEP ☑ DCEN ☐ Pulsed ☐
Backgouging: Yes ☐ No ☑ Method:	Power Source: CC ☐ CV ☑
Root Treatment: Stainless steel wire brush	Other:
POSITION	Tungsten Electrode (GTAW):
Position of Groove: Fillet: 2F	Size: Type:
Vertical Progression: Up ☐ Down ☐	**TECHNIQUE**
BASE METALS	Stringer or Weave Bead: Stringer
Material Spec: ASTM A500 (Gr. B min.) or API 5Lx42 PSL2 pipe to ASTM A36 plate	Multi-Pass or Single Pass (per side): Single
Type or Grade:	Number of Electrodes:
Thickness: Groove: Fillet: 1/4"	Electrode Spacing: Longitudinal:
Diameter (Pipe): 2-7/8" OD	Lateral: Angle:
FILLER METALS	Electrical Stick Out: 1/4"-1/2"
AWS Specification: AWS-A5.18	Peening: Interpass Cleaning: Stainless steel wire brush
AWS Classification: ER70S-6	**PREHEAT AND INTERPASS TEMPERATURE CHART**
Mfg. Trade Name: Wa. Alloy Co.	
SHIELDING	
Flux:	
Electrode Flux Class:	
Gas: Argon/Carbon Dioxide Composition: 75%A, 25%CO2	
Flow Rate: 40 CFH Gas Cup Size:	
POSTWELD HEAT TREATMENT	
Temp: NA Time:	

Base Metal Thickness Range	Min Preheat & Interpass (°F)	Max Preheat & Interpass (°F)
1/8"-3/4"	32	N/A

WELDING PROCESS

Pass or Weld Layer(s)	Filler Metal Diam.	Current	Volts	Travel Speed IPM
3/16"<=X<=3/8"	0.035"	160-300A	23-26V	11-22

Joint Designation: Fillet

UPLOAD JOINT DETAILS

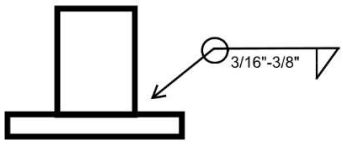

Base metal thickness for pipe and plate: 1/4"-1/2"

FABRICATOR'S CWI DIGITAL SIGNATURE

AWS CWI #: CWI Exp. Date:

UPLOAD FDOT CONSULTANT STAMP

Date:

Notes:

UPLOAD FDOT STAMP

Tim McCullough

Digitally signed by: Tim McCullough
DN: CN = Tim McCullough e = timothy.mccullough@dot.state.fl.us C = US OU = FDC State Materials
Date: 2020.07.28 17:09:33 -04'00'

Date:

Comments: FDOT Research Only. Not Applicable for Production. Additional Qualification is required for D1.2 production welding

E-Mail the completed digital form to SM-StructuresCI@dot.state.fl.us, FDOT State Materials Office

FDOT Note: Qualified for Flat (1F) and Horizontal (2F) plate use only. (Table 4.10)
Single Pass fillet weld are qualified to the max. size shown in the Joint Designation
WPS is invalid if the essential variables listed in Table 3.6 and Table 3.7 are not met;
Preheat Constraint on API and A252 pipe. Using the formula below, if the carbon equivalence (CE) is > 0.4, increase the preheat 200°F.

STATE OF FLORIDA DEPARTMENT OF TRANSPORTATION

WELDING PROCEDURE SPECIFICATION (WPS)

AWS D1.2 WPS
Form # 675-070-06
April 2019

(D1.2 ALUMINUM) QUALIFIED BY TESTING ☑

Contractor/Organization: University of Florida	**WELDING PROCEDURE**
BACKING	Specification No: UF-GMAW-AL-01 Date: 06/05/2020 By: Brittani Maskley
Type: N/A Permanent:	Revision: Date: By:
Removed: Other:	Authorized By: Date:
WELDING PROCESS(ES)	Supporting PQR No(s): 2x Successful Macroetches, per Fig. 3.17
Process: GMAW *Type: Manual, DCEP, Spray mode	**POSITION**
Process: *Type:	Position of Groove: Fillet: 2F
Electrode: (GTAW):	Welding Progression (Forehand/Backhand): Forehand
*Manual, Automatic, Polarity Pulsed, etc.	Vertical Welding (Upward/Downward):
BASE METALS	**TECHNIQUE**
M No.: M23 Thickness: 1/4" to 1/2"	Stringer or Weave Bead: Stringer
Alloy & Temper: 6061-T6	Orifice or Gas Cup Size: 1/2"
FILLER METAL	Oscillation: None
F-No.: F23 AWS No. (Class): ER4043	Contact Tube to Work Distance: 3/4"
Size of Electrode: 0.035"	Single Pass or Multipass (per side): Single-pass side 1, multi-pass side 2
Type of Electrode: Wire Spool	Tungsten Extension:
Mfg. Trade Name: Blackstone	Method of Backgouging: N/A
SHIELDING GAS	Other:
Shielding Gas(es): Argon	**POSTWELD HEAT TREATMENT**
Percent Composition: 100%	Original Temper: T6
Flow Rate: 40 CFH	Final Temper: N/A
Other:	Temp: Time:
CLEANING	Quench:
Initial Cleaning Oxide: Stainless steel wire brush	**PREHEAT**
Initial Cleaning Oil & Dirt: Solvent wipe	Preheat Temperature: > 32F
Interpass Cleaning: Stainless steel wire brush	Interpass Temperature: <= 250F

WELDING PROCESS

Pass No.	Welding Process	Current	Volts	Travel Speed IPM
1	GMAW	130-225A	22-28V	14-22

FABRICATOR'S CWI DIGITAL SIGNATURE

AWS CWI #: CWI Exp. Date:

UPLOAD FDOT CONSULTANT STAMP

Date:

Notes:

UPLOAD JOINT GROOVE DESIGN SKETCH

Joint Designation:

UPLOAD WELDING SEQUENCE SKETCH

Joint Designation: Fillet

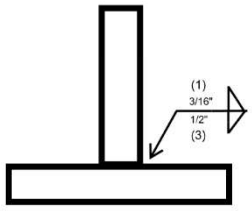

UPLOAD FDOT STAMP

Tim McCullough

Digitally signed by: Tim McCullough
DN: CN = Tim McCullough email = timothy.mccullough@dot.state.fl.us US OU = FDOT State Mate
Date: 2020.07.29 12:58:26 -04'00'

Date:

Comments: Research WPS Only. Production requires Welder qualification and fracture testing.

E-Mail the completed digital form to SM-StructuresCI@dot.state.fl.us, FDOT State Materials Office

FDOT Note: Qualified for Flat (1F) and Horizontal (2F) plate use only. (Table 3.3)
Single Pass fillet weld are qualified to the max. size qualified in testing and smaller. (Table 3.6)
Multi-Pass fillet weld are qualified to the min. size qualified in testing and larger. (Table 3.6)
WPS is invalid if the essential variables listed in Table 3.1 are not met;

STATE OF FLORIDA DEPARTMENT OF TRANSPORTATION

WELDING PROCEDURE SPECIFICATION (WPS)

AWS D1.2 WPS
Form # 675-070-06
April 2019

(D1.2 ALUMINUM) QUALIFIED BY TESTING ☑

Contractor/Organization: University of Florida	**WELDING PROCEDURE**
BACKING	Specification No: UF-GMAW-AL-02 Date: 06/05/2020 By: Brittani Maskley
Type: N/A Permanent:	Revision: Date: By:
Removed: Other:	Authorized By: Date:
WELDING PROCESS(ES)	Supporting PQR No(s): 2 Successful Macroetches, per Fig. 3.18
Process: GMAW *Type: Manual, DCEP, Spray mode	**POSITION**
Process: *Type:	Position of Groove: Fillet: 2F
Electrode: (GTAW):	Welding Progression (Forehand/Backhand): Forehand
*Manual, Automatic, Polarity Pulsed, etc.	Vertical Welding (Upward/Downward):
BASE METALS	**TECHNIQUE**
M No.: M23 (6061) and M26 (356) Thickness: 1/4" to 1/2"	Stringer or Weave Bead: Stringer
Alloy & Temper: 6061-T6 pipe to ASTM B26 or ASTM B108 alloy 356-T6 pipe	Orifice or Gas Cup Size: 1/2"
FILLER METAL	Oscillation: None
F-No.: F23 AWS No. (Class): ER4043	Contact Tube to Work Distance: 3/4"
Size of Electrode: 0.035"	Single Pass or Multipass (per side): Single pass
Type of Electrode: Wire Spool	Tungsten Extension:
Mfg. Trade Name: Blackstone	Method of Backgouging: N/A
SHIELDING GAS	Other:
Shielding Gas(es): Argon	**POSTWELD HEAT TREATMENT**
Percent Composition: 100%	Original Temper: T6
Flow Rate: 40 CFH	Final Temper: N/A
Other:	Temp: Time:
CLEANING	Quench:
Initial Cleaning Oxide: Stainless steel wire brush	**PREHEAT**
Initial Cleaning Oil & Dirt: Solvent wipe	Preheat Temperature: > 32F
Interpass Cleaning: Stainless steel wire brush	Interpass Temperature: <= 250F

WELDING PROCESS

Pass No.	Welding Process	Current	Volts	Travel Speed IPM
1	GMAW	130-225A	22-28V	14-22

FABRICATOR'S CWI DIGITAL SIGNATURE

AWS CWI #: CWI Exp. Date:

UPLOAD FDOT CONSULTANT STAMP

Date:

Notes:

UPLOAD JOINT GROOVE DESIGN SKETCH

Joint Designation:

UPLOAD WELDING SEQUENCE SKETCH

Joint Designation: Fillet

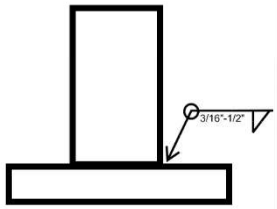

Pipe Diameter: 3" OD

UPLOAD FDOT STAMP

Tim McCullough

Digitally signed by: Tim McCullough
DN: CN = Tim McCullough email = timothy.mccullough@dot.state.fl.us US OU = FDOT State Mater
Date: 2020.07.29 13:00:12 -04'00'

Date:

Comments: Research WPS Only. Production requires Welder qualification

E-Mail the completed digital form to SM-StructuresCI@dot.state.fl.us, FDOT State Materials Office

FDOT Note: Qualified for Flat (1F) and Horizontal (2F) plate and pipe. (Table 3.3)
Single Pass fillet weld are qualified to the max. size qualified in testing and smaller. (Table 3.6)
WPS is invalid if the essential variables listed in Table 3.1 are not met;

Appendix B – Cameras Specifications

Technical specification for the FLIR T620 camera used in this study.

→ **FLIR T620 25° lens**[1]

P/N	55901-1102
Item status	Discontinued, FLIR recommends T1010 as a replacement
Image and IR resolution	640 x 480 pixels
Field of view (FOV)	25° x 19°
Minimum focus distance	0.25m
Focal length	25mm
Spatial resolution	0.69mrad
Temperature range	-40°C to 650°C
Temperature accuracy	±2°C
Spectral range	7.5-14µm
Reference temperature	Manually set
Atmospheric transmission correction	Automatic, based on the user inputs for distance, atmospheric temperature, and relative humidity
Emissivity correction	Variable from 0.01 to 1.0 based on users input
Reflected apparent temperature correction	Automatic, based on the input of reflected temperature
Periodic image storage	14 seconds to 24 hours (IR and visual)
File formats	JPEG, measurement data included
Operating temperature range	-15°C to 50°C

[1] Specifications taken from [57]

Technical specification for the FLIR C5 camera used in this study.

→ **FLIR C5**[2]

P/N	89401-0101
Item status	Item available
Image resolution	640 x 480 pixels
Field of view (FOV)	54° x 42°
Minimum focus distance	0.1m
Spatial resolution	6.3mrad
IR resolution	160 x 120 pixels
Temperature range	-20°C to 400°C
Temperature accuracy	±3°C
Spectral range	8-14µm
Atmospheric transmission correction	Automatic, based on the user inputs for distance, atmospheric temperature, and relative humidity
Emissivity correction	Variable from 0.01 to 1.0 based on users input
Reflected apparent temperature correction	Automatic, based on the input of reflected temperature
File formats	JPEG, measurement data included
Operating temperature range	-10°C to 50°C

[2] Specifications taken from [58]

Appendix C – IR images of coated samples in comparison to uncoated conditions at different temperature ranges

After acquiring a complete dataset of thermal images by active IR-TNDT, the images were analyzed using the native software provided by FLIR. A range of IR images from the samples listed in Table 0-3, at reference temperatures of approximately 50°C, 100°C, and 150°C, is provided.

Al pipe-to-plate with surface-breaking drill hole

T	Uncoated	120-grit rub
Photo	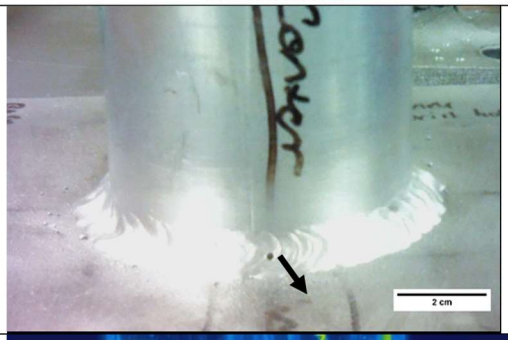	
150°C	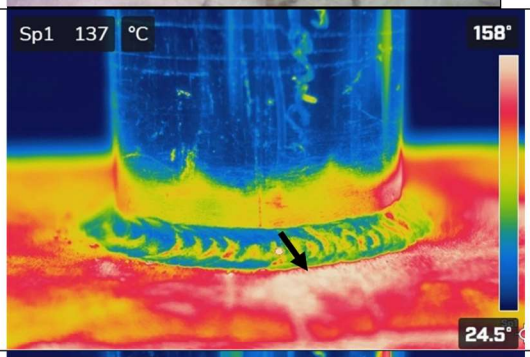	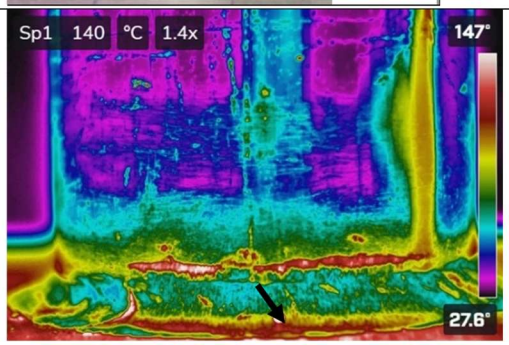
100°C	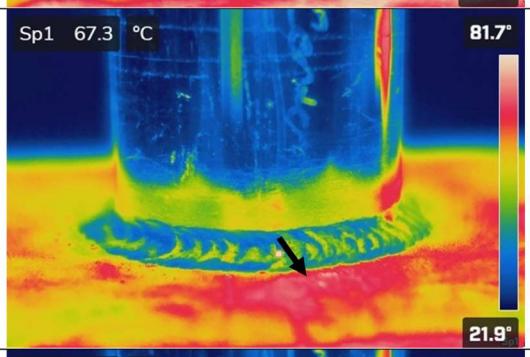	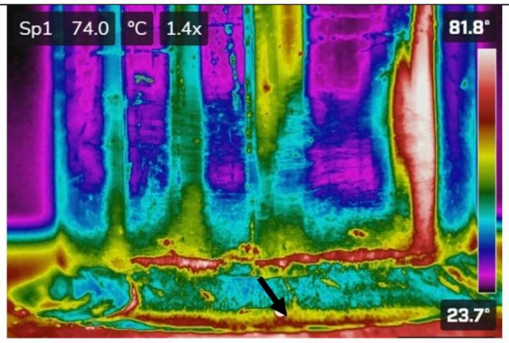
50°C	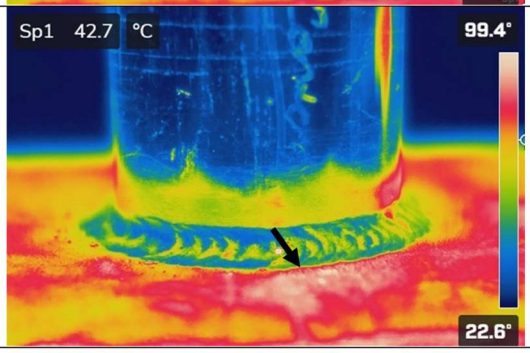	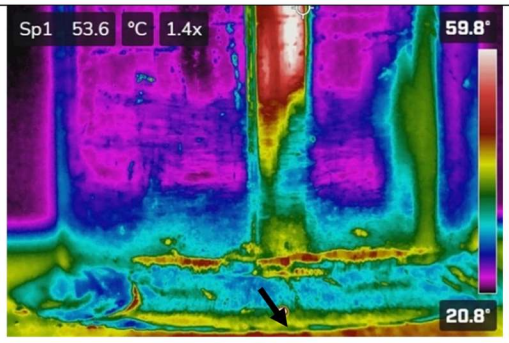

Al plate-to-plate with surface-breaking drill hole

T	Uncoated	120-grit rub
Photo	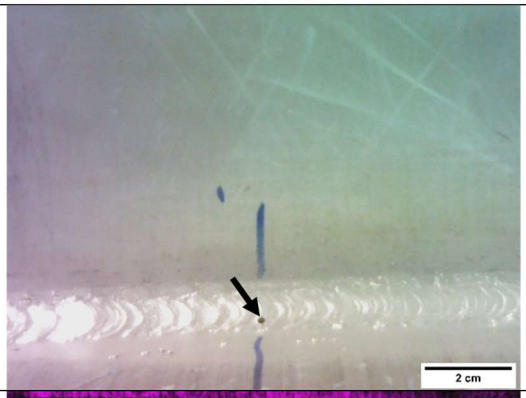	
150°C	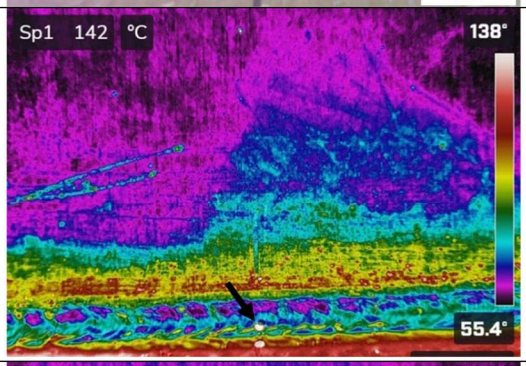	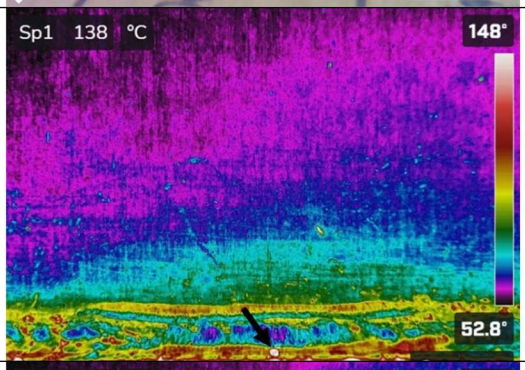
100°C	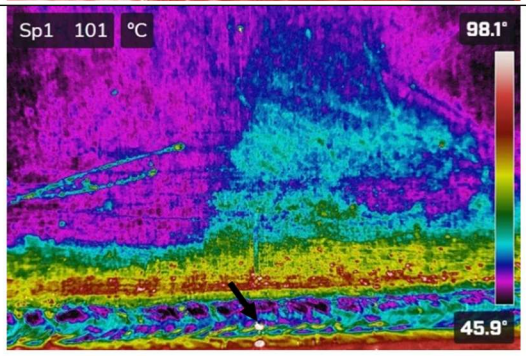	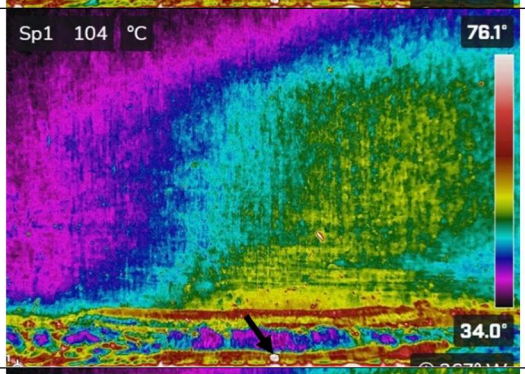
50°C	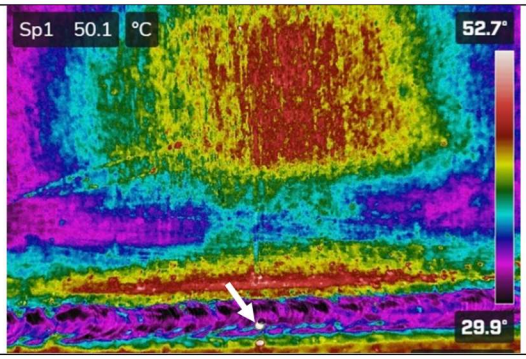	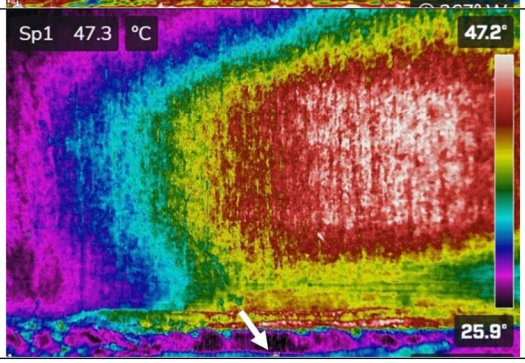

Aluminum plate-to-plate subsurface pseudocrack

T	Uncoated	120-grit rub
Photo		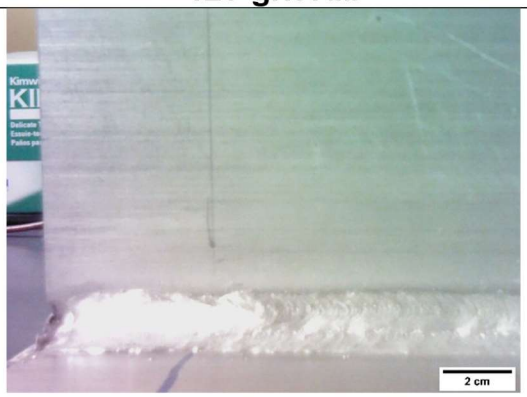
150°C	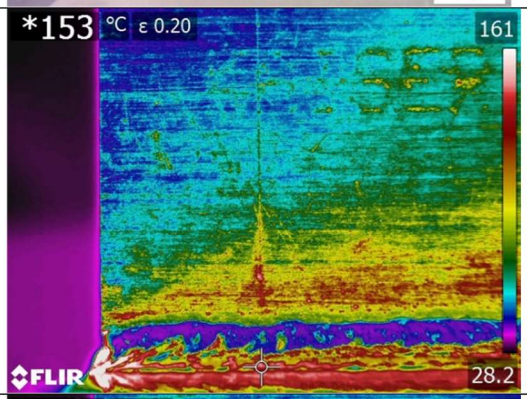	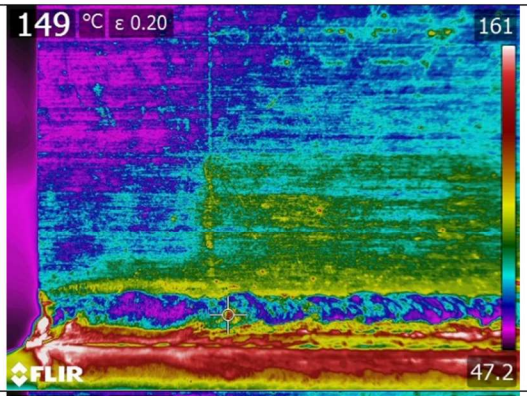
100°C	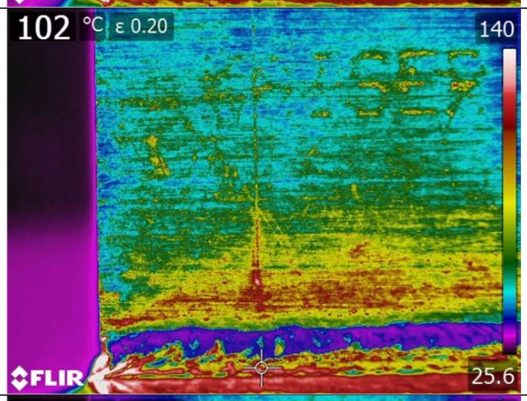	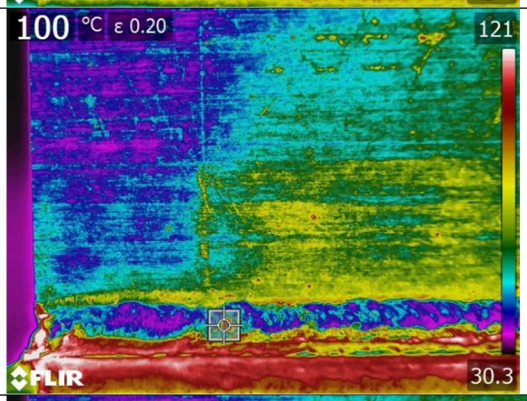
50°C	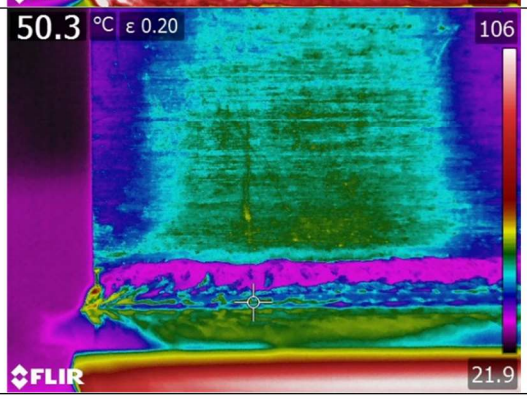	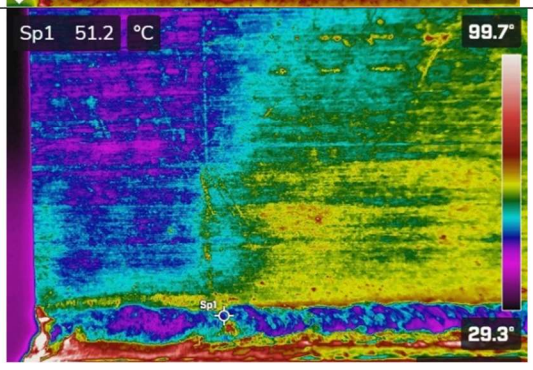

Steel pipe-to-plate – Zinc-it spray

T	Uncoated	1-layer	3-layers
Photo	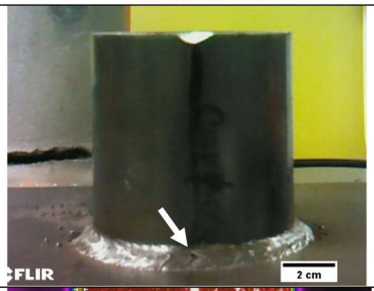	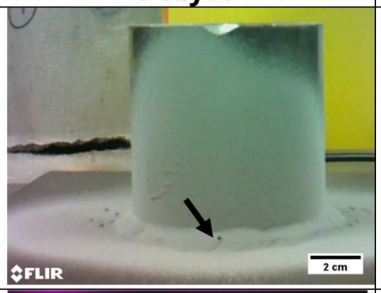	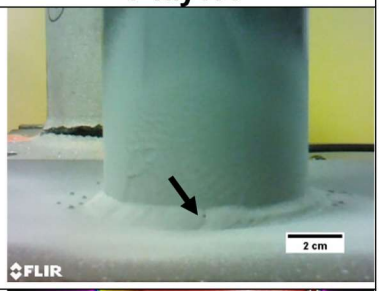
150°C		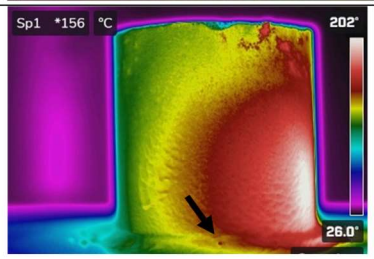	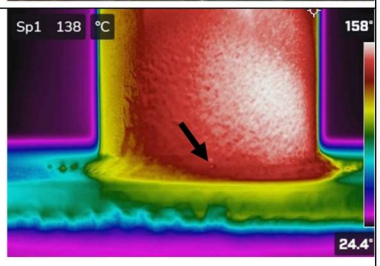
100°C	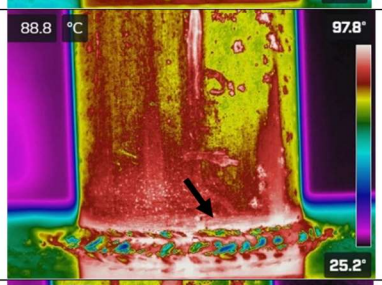	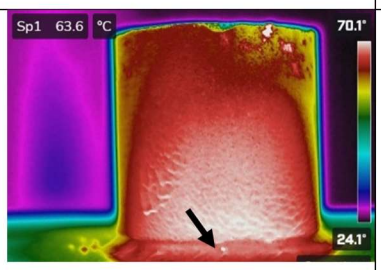	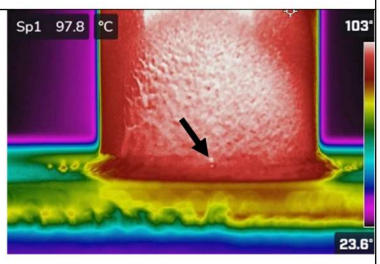
50°C	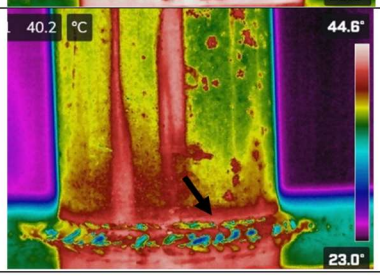	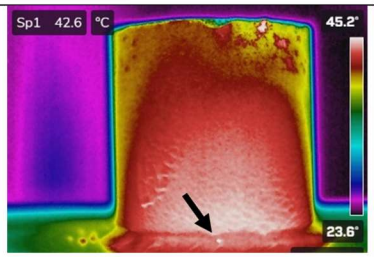	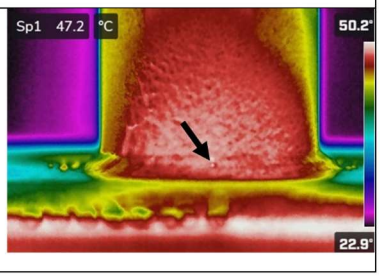

Steel pipe-to-plate – Epoxy-based coating

T	Uncoated	Coated
Photo		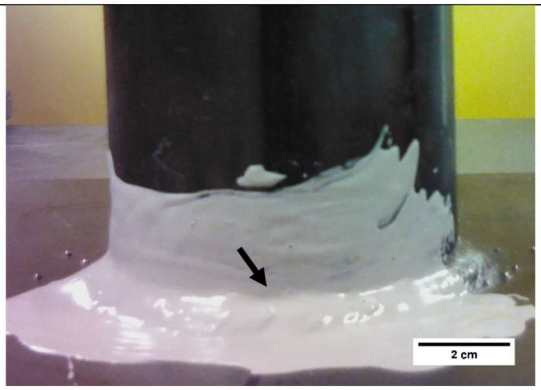
150°C	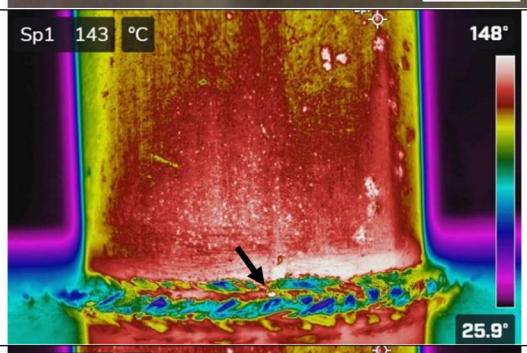	-
100°C	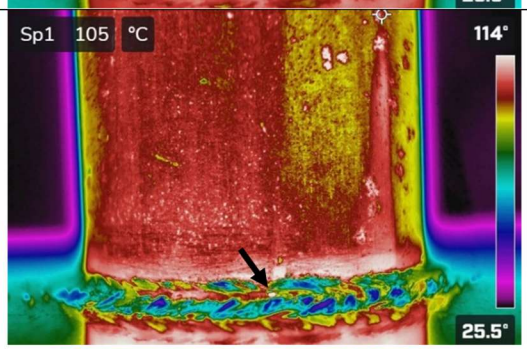	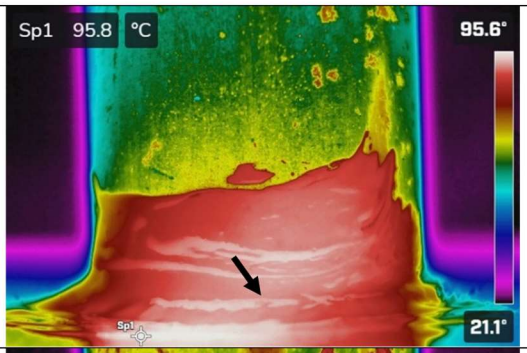
50°C	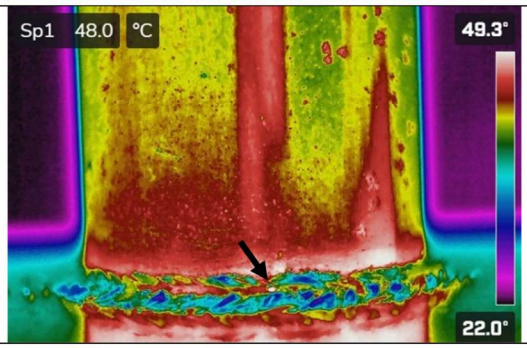	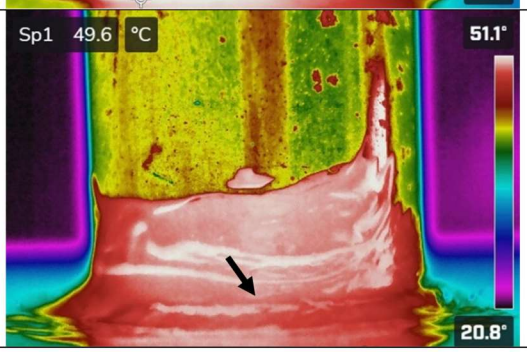

Steel plate-to-plate – Zinc-it spray

T	Uncoated	1-layer	3-layers
Photo	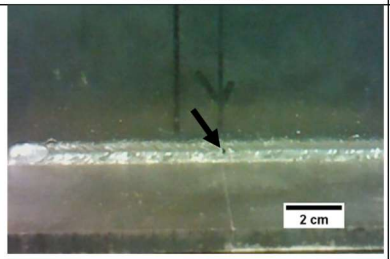	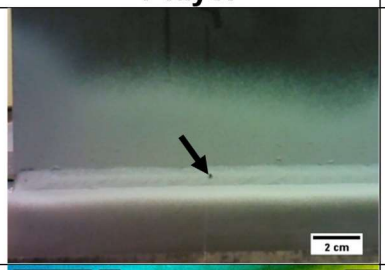	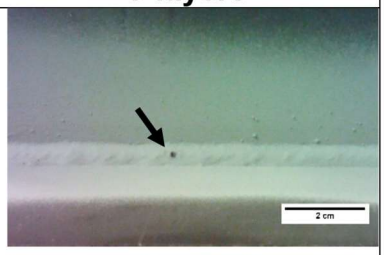
150°C	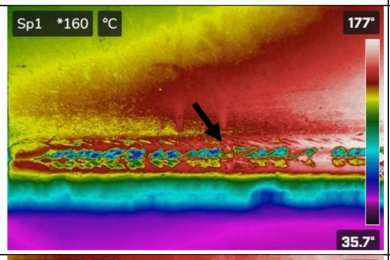	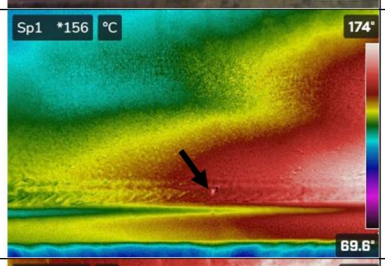	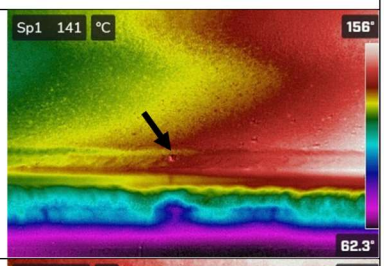
100°C	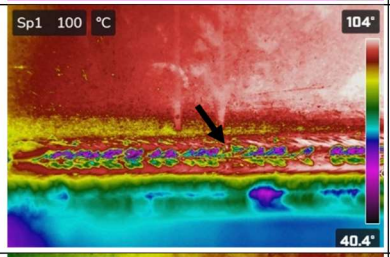	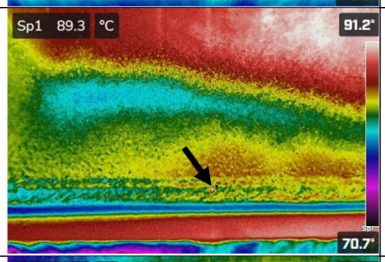	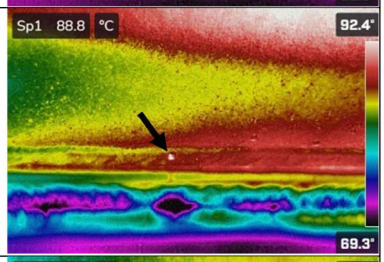
50°C	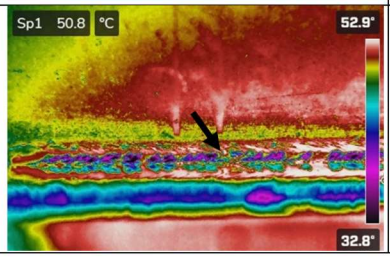	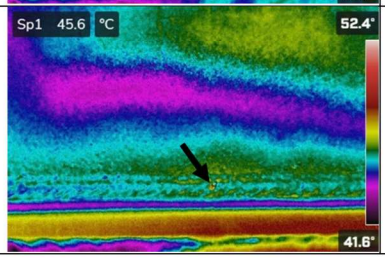	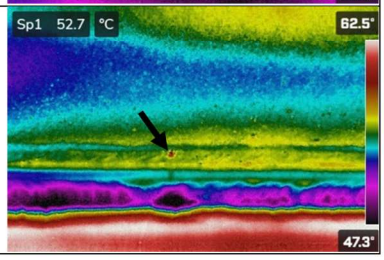

Steel plate-to-plate – Epoxy-based coating

T	Uncoated	Coated
Photo	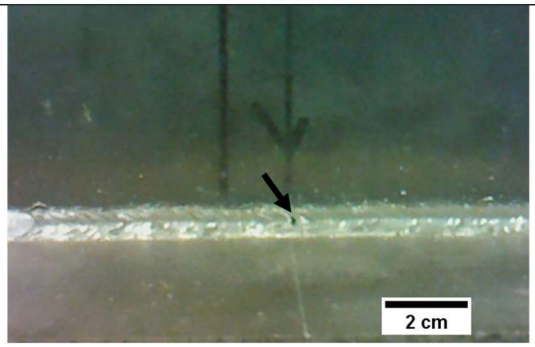	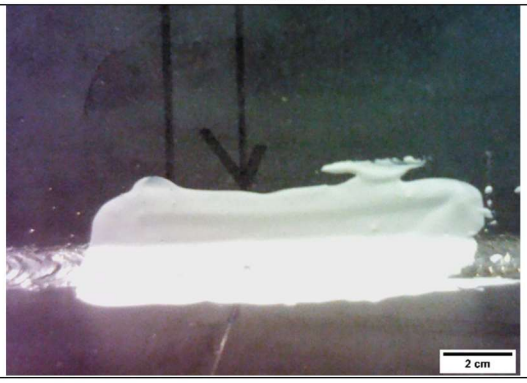
150°C	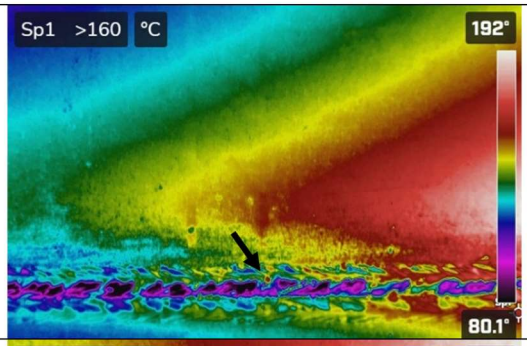	-
100°C	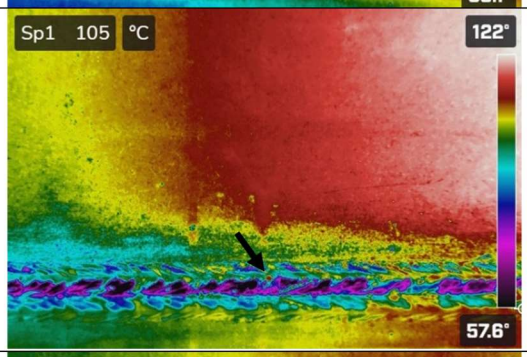	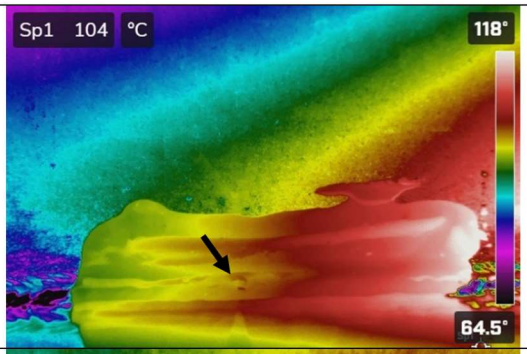
50°C